UNICA

UNIVERSITÀ
DEGLI STUDI
DI CAGLIARI

Ph.D. DEGREE IN

INDUSTRIAL ENGINEERING

Cycle XXXV

TITLE OF THE Ph.D. THESIS

High-Fidelity Computational Analysis of the Aerothermal Performance of In-serviced Jet Engine Blades

Scientific Disciplinary Sector(s)

ING-IND/08 - MACCHINE A FLUIDO

Ph.D. Student:	Mario Carta
Supervisor:	Tiziano Ghisu

Final exam. Academic Year 2021/2022
Thesis defence: April 2023 Session

Abstract

In today's civil aviation, the struggle for higher jet engine efficiencies has pushed the manufactures into the continuous challenge of developing new and better design and optimization strategies. In the information age, it is only natural that a great deal of this effort is going to be carried out by means of computational analysis. That is to say, these design and optimization strategies rely heavily on the use of computational models, and thus the search for a better design is hinged upon the search for a better model. A notable product of this search is the "robust design" philosophy, which aims to consider the variability in geometry and operating conditions that every component will invariably experience in real-world conditions. In general, the key element in this evolution process is for the model to be capable of accounting for more and more aspects of the reality of the problem at hand, while still being affordable in terms of computational costs. In this case, the problem is represented by the aero-thermal behavior of the jet engine's most characteristic components: the blades.

As mentioned above, to increase the fidelity of the model, key aspects that characterize the real operation of these components can be included in it, beginning with the geometry. While most of the computational performance analysis is conducted on nominal designs, it is important to consider that, during most of their service life, the turbine blades are going to operate with a geometry that is increasingly affected by deviation from nominal. This is due to both manufacturing variation and in-service damage. These geometric deviations can be measured on the blades after an engine overhaul, providing highly useful information on the damage modes of the engine. By digitalizing these geometries, engineers can quantify and parametrize the geometric deviation. Furthermore, by creating computational grids around these geometries, a high-fidelity CFD study revolving around the performance of the *real* blades can be carried out, shedding light on the correlation between the geometric deviation parameters and aerodynamic performance loss. Naturally, this geometric deviation also has a significant impact on the thermal behavior of the blades, affecting the distribution of the Heat Transfer Coefficient (HTC) over the blades' surfaces.

Even when modelling the nominal case, it is often common practice to use a simplified version of the geometry, where the internal cooling system is replaced with source terms. Although this reduces the costs of the CFD simulations, it obviously subtracts from the model's accuracy. Furthermore, it is particularly important to model the fluid-solid thermal exchange, and the rotor-stator unsteady interaction.

All these fidelity-related aspects that can impact the model's accuracy are investigated in the present work.

Preface

The majority of the work included in this thesis has been either presented in conferences and published by the author on scientific journals or has been submitted for publication and is being reviewed. These publications are listed below:

[1] M. Carta, T. Ghisu and S. Shahpar, "High-Fidelity CFD Analysis of In-Serviced Shrouded High-Pressure Turbine Rotor Blades" - TURBO-22-1122, ASME Journal of Turbomachinery, vol. 144, no. 12, p. 121001 (12 pages), 2022.

[2] M. Carta, T. Ghisu and S. Shahpar, "Heat Transfer Analysis of Damaged Shrouded High-Pressure Turbine Rotor Blades", Accepted for the ETC15 - 15th European turbomachinery conference in Budapest, Hungary.

[3] M. Carta, T. Ghisu and S. Shahpar, "Multi-Fidelity Heat Transfer Analysis of Shrouded High Pressure Turbine Rotor Blades", Accepted for the ASME Turbo Expo 2023 Conference in Boston, Massachusetts (USA).

Additional work was published by the author during the course of this PhD that made use of the models presented within this thesis, but for different aerodynamic applications:

[4] M. Carta, T. Ghisu and R. Putzu, "A Comparison of Plunging- and Pitching-induced Deep Dynamic Stall on a SD7003 Airfoil Using URANS and LES Simulations", Aerospace Science and Technology, vol. 121, February 2022.

The author has also contributed to other publications during the course of his PhD:

[5] Ghisu, T., Cambuli, F., Puddu, P., Virdis, I., Carta, M., Licheri, F., “A critical examination of the hysteresis in wells turbines using computational fluid dynamics and lumped parameter models” (2020) Journal of Offshore Mechanics and Arctic Engineering, 142 (5), art. no. 052001, DOI: 10.1115/1.4046379

[6] Ghisu, T., Cambuli, F., Puddu, P., Virdis, I., Carta, M., Licheri, F., “A lumped parameter model to explain the cause of the hysteresis in OWC-Wells turbine systems for wave energy conversion“ (2020) Applied Ocean Research, 94, art. no. 101994, DOI: 10.1016/j.apor.2019.101994

[7] Ghisu, T., Cambuli, F., Puddu, P., Virdis, I., Carta, M., “Discussion: "unsteady RANS simulations of wells turbine under transient flow conditions" (Hu and Li)” (2019) Journal of Offshore Mechanics and Arctic Engineering, 141 (4), art. no. 045501,DOI: 10.1115/1.4042875

Among these, [1] was previously published in the following conference proceedings:

[8] Carta. M., Ghisu. T., Shahpar, S. “High-Fidelity CFD Analysis of Shrouded High-Pressure Turbine Rotor Blades”, Proceedings of the ASME Turbo Expo, June 13 – 17, 2022, Rotterdam Ahoy Convention Centre, Rotterdam, The Netherlands – (for journal publication, see [1])

Acknowledgements

I would like to thank my supervisors, Professor Tiziano Ghisu from the University of Cagliari, and Rolls-Royce Fellow Shahrokh Shahpar, for their support and precious advice. I see my Ph. D. years as a time of great personal and professional maturation, and I am deeply grateful to you for guiding me through them.

I would like to express my gratitude and appreciation to my colleagues from Cagliari, and in particular to Irene, Diego and Roberto. Thank you for giving this journey a touch of friendship, and for supporting me whenever I needed it.

I am grateful to my family. My wife Francesca and my daughter Isabella, for their unconditional love and for always being there for me. Thank you for all the sacrifices you have made for me, and for always bringing me happiness through these challenging years. I am lucky to have you in my life, I could not have done this without you. Thank you to my father Giovanni and my mother Elena, and my brother Stefano and sisters Serena and Silvia. Thank you for your infinite love and help, that I was blessed with throughout my life.

I would like to thank Rolls-Royce plc for their support and permission to publish this work. This project has received funding from the European Union's Horizon 2020 Research and Innovation program under grant agreement N 769025.

Contents

List of Figures

List of Tables

Nomenclature

ACRONYMS

BC	Boundary Condition
BDF	Blade definition file
CFL	Courant-Friedrichs-Lewy number
CHT	Conjugate Heat Transfer
CSD	Casing cooling downstream to rotor blade
CSF	Casing cooling upstream to rotor blade
DELT	Blade section circumferential lean adjustment
DI	Design intent
DSH	Hub cavity inflow downstream to rotor blade
EP	Engineering parameter
EXBA	Blade section localized exit angle adjustment
FC	Rotor film cooling inlet
FPS	Front-Pressure-Side
H	Enthalpy [$J\ kg^{-1}$]
HPR	High-pressure rotor
HPS	High-pressure stator
HPT	High-pressure turbine
HTEC	HPS trailing edge cooling slot
IPS	Intermediate-pressure stator
ITEC	IPS trailing edge cooling slot
LE, TE	Leading edge, Trailing edge
LEMA	Inlet angle linear combination variable
LEMO	Blade section leading edge re-cambering
PH	Phase-Lag
PS, SS	Pressure side, Suction side
Q	Objective function value (deterministic)
RANS	Reynolds-averaged Navier-Stokes
RIDN	Inner endwall high-pressure stator film cooling rows
RODN	Outer endwall high-pressure stator film cooling rows
RPS	Rear-Pressure-Side
SKEW	Blade section rotation around the radial axis passing per the section LE

ST	Steady-State
STAG	Stagger angle linear combination variable
TECA	Blade section trailing edge chord extension
TEMA	Exit angle linear combination variable
TEMO	Blade section trailing edge re-cambering
u	Circumferential velocity $[m\ s^{-1}]$
USH	Hub cavity inflow upstream to rotor blade
w	Specific HPR work $[J\ kg^{-1}]$
W	Objective function weight

GREEK LETTERS

η	Isentropic HPT stage efficiency
θ_p	Periodicity angle
μ	Objective function distribution mean
σ	Objective function distribution standard deviation
Φ	Cycle phase during a phase-lag simulation

Chapter 1

Introduction

1.1 Background

Civil aviation constitutes a vital market. The global economy depends on its services for international transport of goods and passengers. Over the years, it has attracted copious investments from private and public entities. Business and touristic travel demands are in an ascending trend [9, 10, 11], clearly impacted in 2020 by the coronavirus pandemic but they are expected to reach pre-pandemic levels in 2025 as they keep rising [12]. Other than being an icon, firmly engraved into our contemporary era's social and cultural context, air travel has rightfully gained a reputation for being the safest form of travel. This reputation is fueled by the development and implementation of reliable and effective technologies. Aviation industry in general has pushed technological innovation throughout its existence, since the Kitty Hawk flight, and will continue to do so in the future. The entirety of the industrial world benefits from the technological advance that is pioneered by the aviation industry. Within the current "green revolution" taking place in the industrial world, a lot attention and concern of governments and the public has been directed at the pollution caused by air travel. This has led to significant strive for lower specific fuel consumptions (SFC) and lower emission levels of modern aircraft engines [13].

1.2 The Jet Engine

The jet engine [14] is a type of internal combustion engine (see Fig. 1) that has come to be widely used in aircraft propulsion. The machine follows the working principle of a Brayton thermodynamic cycle, as depicted in Fig. 2, by compressing a flow of air, mixing it with fuel, igniting the mixture and letting the combustion gases expand. Part of the energy in the expanding gases is used to provide the amount of work needed to perform the initial compression, while the remaining part is converted into velocity.

The high-velocity gas jet is directed rearwards, propelling the aircraft forwards by reaction. In practice, both the compression and expansion of the flows are operated by rotating machinery, which may be of centrifugal or axial design, usually depending on the flow rates involved.

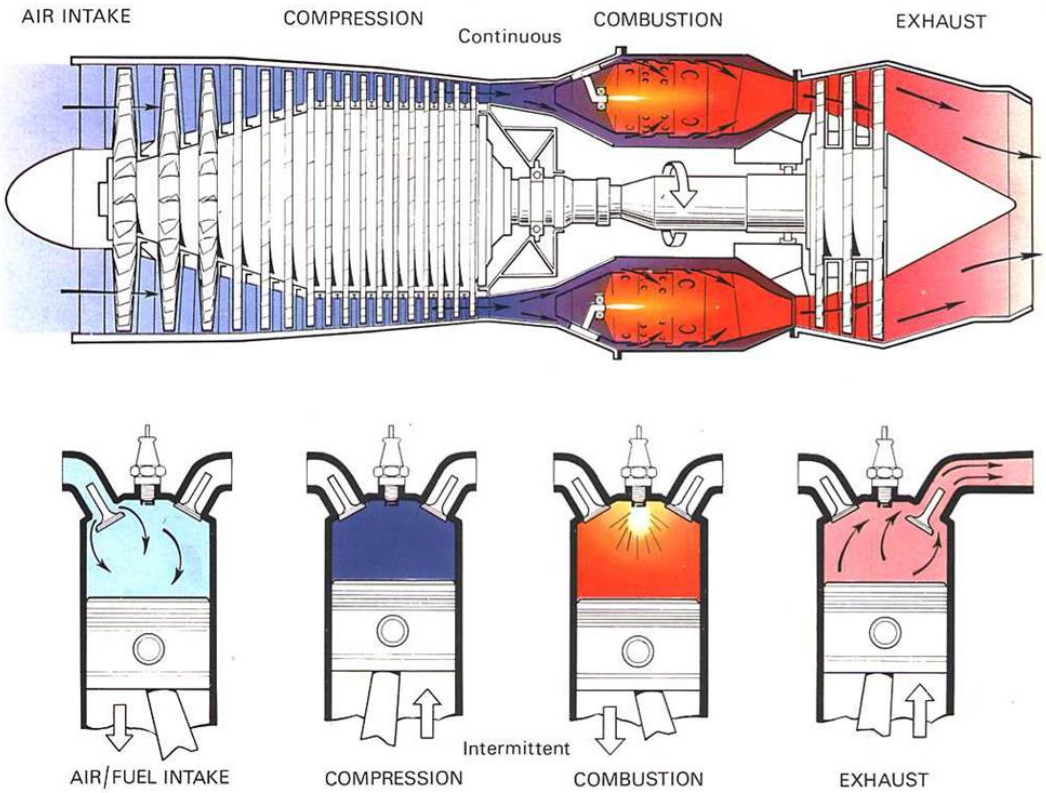

Figure 1: Working cycle of a Jet Engine (above) compared with that of a four-stroke piston engine (below) - Picture from [15]

The compressor and turbine disks are installed on the same shaft, thus allowing for power to flow back from the latter to the former. On the outer circumference of the rotating disks, several blades are fixed in position and constitute the moving parts of the machine, where work is exchanged with the fluid. Circumferentially placed statoric blades are also present, downstream (compressor) and upstream (turbine) to the rotor rows. The combustion of the fuel-air mixture is operated in one or more dedicated chambers. The engine is equipped with an intake to guide the incoming air flow into the compressor, and a rear nozzle to form the jet.

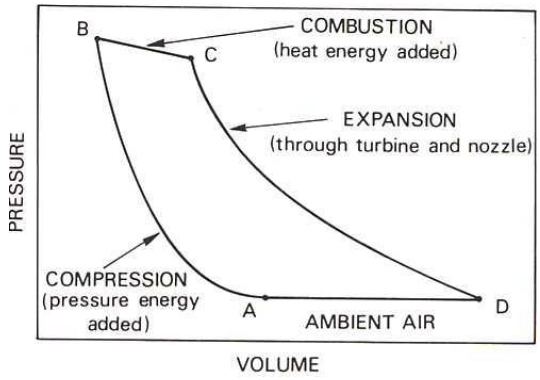

Figure 2: Brayton thermodynamic cycle – Picture from [15]

This engine's cycle efficiency is proportional to the turbine-entry temperature (TET) thus it is desirable to achieve a high value for this parameter. Over the years, the maximum cycle temperatures reached by jet engines have been consistently pushed forwards, from the original 1000-1200 K of early engines such as the Rolls-Royce Derwent and Dart [14], to the current 1800-2000 K of the current turbofans powering wide-body aircraft [15] [16]. These achievements have been made possible by the development of highly resistant metal alloys [17], single-crystal casting [18, 19], thermal barrier coating (TBC) and film cooling techniques [20, 21, 22, 23, 24].

1.3 Numerical Modelling of the Flow on Jet Engine Blades

Particular attention and research effort on the part of aircraft engine manufacturers has been directed into developing numerical simulation capabilities, for high-fidelity performance prediction of the engine components. One of these methodologies is represented by Computational Fluid Dynamics (CFD) which has established itself as a versatile and reliable tool for design optimization [25, 26]. Current state-of the art designs for modern jet engine components are the result of years of tuning and optimization. The growing computational resources available to the industry allowed for the simulation of more and more physical aspects of the machine's operation. Design optimization through modelling is traditionally a deterministic process, where the component's geometry and operating conditions are described by a set of parameters, or design variables. The values for these parameters are selected to achieve an optimal performance level, defined by a set of objective functions. More recently, the optimization community has become aware of the importance of considering many of those design variables as uncertain [27], or subject to variability. This is more realistic, as the geometry of a blade inside a running engine is not going to replicate exactly the nominal one, and the same can be said for the operating conditions. Clearly,

when an uncertainty is introduced in the design space, it produces an output variability in the component's performance, which is proportional to its sensitivity to that uncertain parameter. To optimize the component's performance in the presence of this uncertain input, it means to find the combination of design parameters, when their uncertainty is considered, which produces the most desirable performance output value and variability. Usually, this translates into minimizing an objective function's mean value while also minimizing its standard deviation, in what is called a "robust design optimization" (RDO) [28]. This kind of optimization is always preferrable to its traditional deterministic counterpart. The latter is prone to produce optimum configurations that are exceedingly sensitive to even slight (and inevitable) design and operating point variations. Naturally, this can cause significant performance losses. As usual, the gain in accuracy brought by choosing the robust alternative comes with a cost, which in this case is represented by the additional number of simulations required to deal with each uncertain input. This cost overhead becomes quickly unsustainable when more and more uncertainties are included in the design space, due to what is often referred to as the "curse of dimensionality" [29, 30, 31, 32]. For this reason, it is always recommended to start by firstly assessing the sensitivity of the component's performance to each of the uncertain parameters being considered, to eliminate those which have a negligible impact. This sensitivity analysis informs the designer on which geometric variabilities are associated with the most amount of performance loss. It can be used to shed light on the loss mechanisms that are triggered by each kind of geometric deviation, which helps the designer in setting up and guiding the subsequent optimization process.

1.4 In-serviced Component Analysis

Modern jet engine blades have a high degree of geometrical complexity, especially in what is called the hot end of the machine, the turbine. The rotating components must endure extremely high temperatures on top of the significant amount of mechanical stress. These geometric features include cavities, secondary flow inlets, film cooling systems and clearances between neighboring components in the assembly. To conduct a proper sensitivity analysis on this kind of case, it is important to include in the computational model as much as this complexity as possible. Moreover, as already mentioned in the previous section, the actual geometry of these components within the running engine will be different from the design-intent (DI) one. This is partly due to manufacturing variations or defects [33]. However, these phenomena tend to originate very narrow deviation fields, due to the high quality-control standards and scrap-rates.

Another important player in real-life-conditions geometric deviation from nominal is in-service deterioration [34].

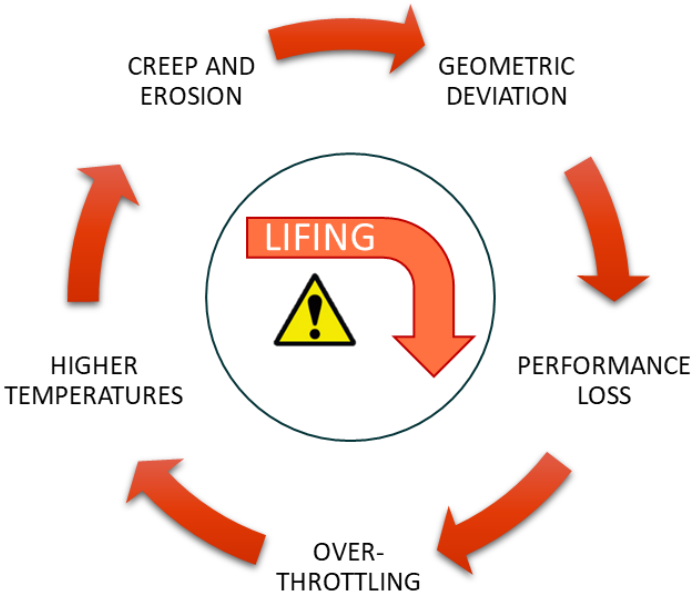

Figure 3: In-service deterioration as a sequence of reciprocal cause and effect

For turbine blades, this deterioration will manifest itself in patterns that are indeed peculiar to the design and operating conditions at hand, but principally include plastic deformation (creep) [35] and volume loss due to erosion [36]. This phenomenon has the potential to produce macroscopic geometric deviation, of orders of magnitude larger than those attributable to manufacturing variation. Clearly, when a turbine blade is designed and tested, this includes analytical and experimental investigations of its failure modes and deterioration rates [37, 38]. However, due to uncertainty on geometry and operating conditions of the blades, there are several factors that can accelerate the deterioration process, or in general, deviate it from the predicted course. In some cases, these factors can feed into each other circularly, forming what can be seen as a “vicious circle”. As exemplified in Fig. 3, some degree of geometric deviation from nominal on any engine component could be impacting the machine’s performance. This would trigger the need for over-throttling to achieve the desired thrust, which in turn would lead to higher stresses and temperatures. As a result, the blades’ deterioration rates would increase, leading to further geometric deviation, and so forth. From the aerodynamicist’s perspective, it is paramount to understand how said geometric deviation translates into a loss in performance.

1.5 Thesis Motivation and Outline

This work presents a high-fidelity study on the correlation between geometric deviation and performance loss, both in terms of aerodynamic and thermal performance. Instead of being carried out on academic case-studies, this analysis is conducted on high-resolution optical scans of several in-serviced high-pressure turbine (HPT) rotor blades, from a modern high-bypass jet engine. These components present geometric deterioration modes that resulted from experiencing real-life operating conditions. In other words, the geometric deviation displayed by these blades gives an account of the actual conditions a typical turbine rotor blade is going to end up working in during the end of its service life. This analysis enables to determine which, among the geometric deviation modes the design is going to develop, are those that need to be avoided. Thus, where the design of this blade would benefit the most from an "informed" optimization procedure. The study is focused on the high-pressure turbine stage. Particular attention has been paid to the tip region of the shrouded rotor blade. It is well known in literature that this is the part of the geometry where deformation is associated with the highest degrees of performance loss. Firstly, the investigation covers the aerodynamics of the stage, to determine the main loss mechanisms associated with isentropic efficiency loss. Secondly a heat transfer coefficient (HTC) analysis is conducted to investigate on the mechanisms that correlate in-service deterioration to an increase in surface heat transfer. Lastly, a methodology for high-fidelity conjugate heat transfer (CHT) simulation of the nominal fully featured rotor blade is presented, and the model is validated against experimental data. The one-and-a-half stage model used to conduct the CFD simulations is comprised of the high-pressure stator, high-pressure rotor, and intermediate-pressure stator. A set of 120 scanned rotor blades is considered for the aerodynamic analysis and 66 blades for the HTC analysis. These geometries are obtained through high-resolution blue-light optical scanning performed by GOM metrology [39] (GOM scans). On these blades, in-service deterioration is firstly quantified and parametrized using an automatic technique called "inverse mapping". This technique is based on a multi-phase optimization routine and allows to describe geometric deviation from nominal of each blade scan with a compact and orthogonal design space. Following this, the computational domains are meshed for flow simulation, and correlation between the parametrized geometric deviation and the aero-thermal performance metrics is sought. For the conjugate analysis, only the DI rotor geometry is considered, where the geometry is fully featured including the internal cavity and cooling holes. While the aero-thermal investigations conducted on the in-serviced rotors are carried out by simulating the "cruise-conditions" operating point, the CHT simulation is conducted for

flow conditions that replicate those of a thermal-paint experimental test. The present work is structured as follows: the next section provides theoretical background and a comprehensive survey on the state of the art regarding sensitivity analysis, uncertainty quantification and robust optimization techniques. The aerodynamic analysis on the in-serviced rotors is presented in the third section, starting with an introduction where the uncertainty quantification methodology and CFD modelling technique are described. The fourth section contains the heat transfer analysis, where the HTC calculation technique is described, and a new set of in-serviced blades is studied. In the fifth section, the geometry and modelling technique used to conduct the CHT simulation on the fully featured HPT rotor are presented. CHT results are then compared to those from the lower-fidelity levels and an additional conjugate run is performed and compared with experimental data. The last section of the thesis provides the concluding remarks.

Chapter 2

Uncertainty Quantification and Robust Design Methods

2.1 Concept of Design under Uncertainty

Design variables and other design parameters might be affected by some level of uncertainty, that can cause a deviation in the performance of the component. A first distinction can be made between “aleatory” and “epistemic” uncertainty [27]. The former has to do with many factors relating to the component’s operating conditions, manufacturing variations between different units and deterioration. Epistemic uncertainty is introduced by simplification and errors in the modelling process. In CFD, those errors are evaluated during verification and validation of the code [40] and can be reduced through better understanding of the problem’s physics and a more correct choice of discretization and numerical solution strategies.

Robust performance analysis, as opposed to the deterministic one, accounts for input uncertainty through its quantification and propagation, providing as a result a probabilistic distribution for the objective function. When this approach is integrated within an optimization problem, optimal values for different moments of said distribution are sought for. Investing in robust design and optimization is crucial to guaranteeing high performance in real-world conditions. Robustness of a design also goes hand-in-hand with its reliability since a reduced variation of the system’s response also means more operational margin with respect to the specified constraints.

Mathematical foundations for the general theory of robust optimization can be found in the work of Ben-Tal [28] and Ben-Tal et al. [41]. Bertsimas et al. [42] give a wide overview on the usage of robust optimization in many scientific grounds. An outline on robust optimization for engineering design can be found in the work of Arora [43]. Other comprehensive surveys on the subject are represented by the work of Park et al. [44] and Beyer et al. [45], while for an analysis more focused on aeronautic engineering

applications of robust design optimization, one should refer to the work of Hirsch et al. [46] which also hosts a number of practical RDO studies on turbomachinery cases.

In this section, different robust optimization strategies currently used in the field of turbomachinery design are presented. RDO procedures will be analyzed with a view on four points, namely:

1) Choice of objective function.

2) Choice of design space.

3) Choice of optimization framework: methods used to investigate the system's response, investigate the connection between each design and its performance.

4) Choice of uncertainty propagation method.

2.2 Choice of Objective Function

The difference between traditional and robust design optimization is that the former considers only nominal performance, while the latter takes into account the different moments of the figure of merit. If we limit this analysis to the first two moments (mean and variance), the objective of an RDO is to maximize (minimize) the mean value of certain performance-related objective functions (cost functions) while minimizing their variance, in the presence of one or more constraints. Therefore, even when dealing with a single-objective nominal optimization problem, RDO is inherently a multi-criteria optimization. If x is the vector of the system variables, μ is some cost function's mean value and σ its standard deviation, a constrained robust optimization problem can be written as:

$$
\begin{aligned}
&\min_{x_l} && \mu(x_l) && l = 1, \dots, L \\
&\min_{x_l} && \sigma(x_l) && l = 1, \dots, L \\
&subject\ to && g_j(x_l) = 0 && j = 1, \dots, J \\
& && h_k(x_l) \geq 0 && k = 1, \dots, K \\
& && x_{l,min} \leq x_l \leq x_{l,max}
\end{aligned}
\tag{1}
$$

Multi-objective optimization translates in the search for a Pareto front (with respect to mean value and standard deviation), representing a set of "non-inferior" solutions. In the end, one of the Pareto points will be selected from the front, according to the designer's preferences. Many of the RDO studies on turbomachinery that can be found in literature present the kind of multi-objective setup discussed above. In [46], Nigro et al. (pp. 495-511) used this approach to optimize mean value and standard deviation of the Rotor 37 blade's aerodynamic efficiency. As an additional objective, the minimization of the pressure ratio's standard deviation was included as well. They found that the pressure ratio's mean value was conveniently maximized indirectly just by optimizing the mean value of efficiency.

Shahpar [47] presents an RDO of a compressor blade with geometric uncertainty due to manufacturing variations. In that case, the author used a multi-objective approach involving minimization of a loss factor's mean value and variance. A similar setup can be found in the work of Kumar et al. [48] [49] [50], also for manufacturing variations, and in [51] for robust optimization of a compressor blade under geometric variations due to erosion.

In [52], Seshadri et al. set up their RDO as a minimization of the aerodynamic efficiency's variance and inverse of mean value for a Rotor 37 case. Seshadri's work here is also interesting for the choice of design space, which will be discussed in the next paragraph. Kamenik et al. in [53], for a high-pressure turbine blade case, defined their RDO problem as a minimization of expected value of the opposite of isentropic efficiency $E[-\eta_{is}]$ and variance of isentropic efficiency $Var[\eta_{is}]$.

If the designer wants to reduce the problem in (1) to a single-criterium optimization (in order to limit computational cost), this can be done by including both mean and variance in the same to-be-optimized function, by introducing weights. General theory on the proper usage of the weighted sum method in design optimization can be found in [54]. The weights fulfil the need of pre-emptively specifying the designer's preferences regarding a trade-off between multiple competing objective functions (in this case mean and variance). For convex problems, minimization of a weighted sum yields a single point, which belongs to the same Pareto front that would have been obtained by optimizing the different functions separately. The position of said point along the Pareto front will depend on the choice of weights. In chapter 7 of [55], Wang presents and compares four optimization studies on a Rotor 37 case, conducted by using different formulations of the objective function:

1) Deterministic optimization

2) Single-objective optimization using weighting functions

3) Single objective optimization using a combined objective

4) Multi-objective optimization

In the second case, the objective function was a sum of penalty terms as formulated in Eq. 2.

$$\min_{x} \quad P1(x) + P2(x) \tag{2}$$

Where P1 is relative to efficiency and P2 to the efficiency's standard deviation. The penalty terms in Eq. 2 had the following form:

$$P(x) = W\left(\frac{Q_{des} - Q(x)}{Q_{ref}}\right)^{m} \tag{3}$$

Where W is a weight, and the letter Q indicates an objective quantity's value. Inside the parentheses, the numerator on the right side in Eq. 3 represents the difference between the desired value Q_{des} and the calculated one $Q(x)$. This quantity is normalized by dividing it for a reference value Q_{ref}, and the magnitude of the fraction term can be adjusted by tweaking the parameter m. In the third case, the problem was defined as follows:

$$\max_{x} \quad \frac{\mu(x)}{\sigma(x)} \tag{4}$$

Since the figure of merit in Wang's work is aerodynamic efficiency, Eq. 4 is expressing a maximization of the mean efficiency value divided by its standard deviation. The fourth case is of the type described in Eq. 1 where mean value and standard deviation constitute two different objective functions. When comparing the results obtained with the different strategies, Wang claims that the multi-objective optimization method shows no superiority on the single objective optimization techniques. Furthermore, changes in penalty setting for the second case do not seem to significantly affect the final optimization result.

Zhiying et al. [56] adopted the weighted sum approach to run an RDO on a turbine blade by using complementary weights in the following form:

$$\min_{x} \quad \alpha\mu(x) + (1-\alpha)\sigma(x) \tag{5}$$

In this case, the authors assigned to α in Eq. 5 a value of 0.2. An optimization strategy is classified as "variance-based" when the relative (to the one of mean value) weight assigned to variance is smaller than 6, while for larger values it is more appropriate to refer to it as "reliability-based" [57]. An example of a Reliability-Based Robust Design Optimization method (RBRDO) can be found in the work of Jeong et al. [58]. Design for Six Sigma is a reliability-based design philosophy according to which variance must be given six points of weight. This concept constituted the aim of a work by Roos et al. [59] which conducted both CHT and FSI studies on an axial turbine stage, followed by robustness evaluations. Kato et al. [60] conducted a robust optimization on a rocket fuel turbopump's turbine where the objective function (adiabatic efficiency) was expressed in the following form:

$$\max_{x} \quad \mu(x) - k\sigma(x) \tag{6}$$

where the weight k was equal to 3. This modus operandi ensures that the final optimized performance will have a 99,7% probability of being higher than the maximized value, that is, provided that the output variable's distribution is normal or close to a normal one.

The value of k in this kind of optimization setup is critical. A study in which the objective function definition of Eq. 7 is adopted, and different values of k (3; 4.5; 6) are used, can be found in the work of Korolev et al. [61], which focused on a structural case.

$$\min_{x} \quad \mu(x) + k\sigma(x) \tag{7}$$

The same definition expressed in Eq. 7 was used by Antinori et al. [62] for a multi-disciplinary RDO on a low-pressure turbine's Secondary Air System (SAS). Here the authors adopted a weight of 2 for the deviation term, and the quantity of interest was the cooling air mass flow.

The value of k = 2 was also adopted by Martin et al. [63] that conducted a robust multi-objective optimization of an axial compressor blade. In their study, the authors

defined three objective functions, two of which followed the formulation in Eq. 7, namely pressure loss at design-point conditions and off design losses.

If the designer has in mind a particular shape (and mean value) for some performance parameter's probability density function, the robust optimization problem can also be set up as a progressive minimization of the distance between the PDF obtained during optimization and the reference one. This technique is known as "density matching" [64]: through the formulation of the function with which the distance between the curves is evaluated, the designer can establish the relative importance of the error on mean value versus the one on deviation.

Robustness can also be evaluated based on the tendency of a given design's mean performance to deteriorate when moving to off-design conditions. Inside an optimization framework, this tendency can be inhibited through the formulation of additional partial-load objective functions, as was done in the work of Ghisu et al. [65].

Dow and Wang in [66] underline that robust optimization should also be aimed at avoiding that manufacturing tolerances may cause a switch in the dominant loss mechanism. Problem definition in that case was limited to the minimization of a certain loss coefficient's mean value, with input uncertainty coming from manufacturing variations. Output QoI's variance or standard deviation were not included in any objective function: instead, to pursue optimum robustness, the authors chose to perform multipoint optimization where the angle of attack on a UTRC fan exit guide vane was set to vary in a narrow interval centred around its nominal value.

In some cases, as a way to reduce costs, the RDO cycle is set up as a deterministic optimization followed by a robustness evaluation [59] where the cycle repeats itself until the deterministic optimum is able to satisfy the robustness criteria, or until the maximum number of iterations is reached. This strategy is often referred to as "successive" robust optimization.

2.3 Choice of Design Space

In robust optimization, a distinction can be made between:

1) Design/Control variables (belonging to the Control Space)

2) Uncertain/Noise variables (belonging to the Noise Space)

Elements from the first class are used to build a design space, while the second class represents a set of variabilities with respect to which the system's response has to become insensitive. These two sets can overlap: in that case, some or even all of the

design variables will also be affected by noise, as it is the case for example in some of the works here analyzed [48] [49] [50] [51] [62] [63].

2.3.1 Design variables

Choice of the design variables should firstly be motivated by the need to control the main physical (aerodynamic, thermal, structural) features on which the machine's performance typically depends on. In [67], the choice derived from the consideration that performance losses in Rotor 37 are caused mainly by two well-known flow features, namely inlet shock and hub stall. Their design space therefore included some specific engineering parameters (sweep and curve angles at different span sections) through which they believe, based on previous knowledge on the machine, that said phenomena can be effectively controlled.

A number of other relevant geometric and operational design variables should be included in the initial space in order not to prevent the optimization algorithm from exploring possibly interesting design solutions. To slim down the list of secondary design variables to be considered for the purpose of optimization, a sensitivity analysis can be pre-emptively conducted.

Besides using engineering parameters, another option for geometric design variables is represented by bump functions, such as the widely used Hicks-Henne, or in alternative, Free-Form Deformation (FFD) methods can be used. Through local bump addition, a blade section can be effectively reshaped [48] [49] [50].

In [52], Seshadri et al. conducted two different optimization studies on a Rotor 37 case: one where blade geometry was parametrized with engineering parameters (tangential lean, axial sweep, leading edge and trailing edge re-cambering) and the other by using bump functions, where the former approach provided a better optimum.

Design variables often include leading edge and trailing edge angles at different span sections, as can be found in the work of Vinogradov et al. in [46] (pp. 583-600) for optimization of an NPO Saturn fan blade. Nigro et al. [46] (pp. 495-511) had the aforementioned two variables and also included tangential and axial stacking laws, chord length and maximum thickness at different span sections.

Seshadri et al. [64] conducted a robust optimization study on a Rolls Royce fan stage, where their design space included rotor and stator hub lines, as well as a series of tri-dimensional engineering parameters relatively to the stator, namely tangential lean, skew, leading edge and trailing edge re-cambering, axial sweep at different span sections. Similarly, in [53], Kamenik et al. parametrized a high-pressure turbine blade in terms of skew, sweep, lean, leading edge, and trailing edge re-cambering at different sections.

Ghisu et al. [65] conducted a robust optimization through mean-line analysis on a 3-shaft compressor core, one of the main design variables being the number of stages of the intermediate pressure compressor.

Wang [55] and Wang et al. [67] adopted meridional sweep and tangential lean at hub and tip as design variables to perform RDO on Rotor 37.

In their reliability-based design optimization conducted on a turbine stage, Roos et al. [59] selected as control parameters rotation speed, blade hub and shroud angle, guide vane blade angle, total inlet temperature, total inlet pressure and rotor blend radius.

Kato et al. [60] parametrized a rotor blade belonging to an axial turbine stage by using two b-splines, one for each side of the aerofoil, controlled through 7 parameters each. They also included as design variables blade axial chord length, stagger angle, leading edge, and trailing edge radii.

Antinori et al. [62] conducted a multi-physics (thermo-mechanical) robust design optimization of a low-pressure turbine's cooling flow system with a high number of design variables of operational, geometric and thermal nature. For the operational part, they considered inlet and outlet temperature and pressure, both for the low-pressure turbine and the high-pressure compressor. The geometric variables were the orifices' cross-section area, the labyrinth gap and the restrictions' cross-section area, while for the thermal part they adopted a number of coolant mass flows. Their set of design variables resulted from a preliminary sensitivity analysis.

Martin et al. [63] parametrized an axial compressor blade with a series of engineering parameters, namely maximum thickness, blade lean and tilt, leading edge and trailing edge radii, inlet, and outlet blade angles at different span sections.

2.3.2 Uncertain variables

The choice of uncertain variables is up to the designer and depends on the focus of the optimization, which is that of de-sensitizing the machine's performance with respect to a specific set of variabilities.

Approaches based on the generation of random bump or geometric noise functions can be useful when the intent is to reproduce geometric variations due to manufacturing tolerances [48] [50] [53] [59] or even superficial wear due to erosion [51].

Small variations in the manufacturing process must not be the cause of a switch in the dominant loss mechanism (e.g., the way the flow transitions or separates) for a certain blade design. The main flow features on which a component's efficiency loss depends on have to be controlled (through the design variables) and should not be significantly altered by changes in geometry and/or operating conditions due to uncertainty. This aspect of the design problem is addressed by Dow and Wang in [66],

where a distinction is made between “geometry design” and “tolerance design”. The authors formulated an aerodynamic loss coefficient, and their aim was to detect its sensitivity to local variations in the blade’s superficial profile. The idea behind that is to bring machining accuracy on different parts of the blade’s surface in line with the above-mentioned sensitivity value, in order to limit additional expenses due to higher precision requirements only to the parts of the blade on which performance is actually sensitive to that improvement.

In order to do that, they proposed a de-coupled optimization procedure:

1) Geometric Optimization - Minimization of the loss coefficient’s mean value with respect to the geometric design variables (in their case five Chebyshev modes for blade thickness) with a multi-point approach based on stagger angle variation, resulting in a robust blade design

2) Tolerance Optimization - Sampling a high number of virtual blades obtained by applying a random geometric noise (within realistic bounds) to the blade obtained in step 1, and detecting the tolerance settings that provide the smallest losses

This kind of de-coupled analysis can be done only if the geometric variations due to the first step are significantly larger than the ones involved in the second step. In their case, Dow and Wang compared the results from the proposed de-coupled procedure with the one from a standard coupled one where the manufacturing noise was applied directly in the geometric optimization problem and obtained very similar results from the two methods.

For RDO on fan blades, outlet static pressure is often selected as uncertain variable as can be seen in the work of Pisaroni et al. [46] (pp. 305-325), Nigro et al. [46] (pp. 495-511), and Wang et al. [67], while in [64] the uncertain variable was the rear-seal leakage mass flow rate.

Kato et al. [60] performed RDO on the axial turbine of a rocket fuel turbopump and adopted the rotational speed of the machine as an uncertain variable.

Seshadri et al. [52] conducted an RDO on a Rotor 37 case aiming to find an optimum design which was also less sensitive to tip-gap variations. To achieve those variations without having them affecting the blade’s shape, they displaced the casing instead. From previous studies on the relation between tip clearance and aerodynamic efficiency on Rotor 37, the authors were aware of a region of tip clearance values (between 0.2% and 0.9% of the total blade span) where efficiency behaviour was remarkably linear. Since for the purpose of their investigation the tip gap variation’s

PDF was contained inside that region (lower bound 0.5% and upper bound 0.85%), the authors took advantage of said linearity to significantly reduce the complexity of their noise space: for each design, just two 3D CFD simulations (i.e., one for each bound of the noise variable) were enough for them to calculate the response's statistics.

In the work of Ghisu et al. [65], the uncertain variable is represented by a load-related quantity, namely the total temperature ratio between combustor outlet and core compressor inlet, to which a bimodal PFD was assigned, with a maximum near design-point conditions and another one near idling. Through the assignment of different limiting values to the above-mentioned load factor, the authors were able to simulate two different cases: on-design and partial-load conditions.

In some cases of RDO in the presence of manufacturing tolerances, the designer might end up with a large number of correlated uncertainties. As a way of reducing the noise space to a smaller number of uncorrelated modes, Principal Component Analysis (PCA) can be used, see for example the work of Nigro et al. in [46] (pp. 431-444) on a high-pressure compressor stage.

Spotting patterns in the covariance matrix of the elements of the noise space can help reduce the number of uncertain dimensions. An example of that is represented by the work of Kamenik et al. [53], who conducted an RDO on a high-pressure turbine blade in the presence of manufacturing variations. Kamenik chose not to resort to PCA in order to keep parametrization straightforward to interpret (2D blade section engineering parameters) and with as few elements as possible. FFD methods can also be used to parametrize a virtual blade to replicate manufacturing noise.

2.4 Choice of Optimization Framework

In many industrial applications it is impractical to only rely on high-fidelity methods to perform the whole optimization routine. In this context, surrogate models or Response Surface Models (RSMs) are often used, such as Artificial Neural Networks (ANN) or Support Vector Machine (SVM) which cost-effectively provide an approximation of the system's response to a wide set of input conditions. Abundant literature can be found on the subject of meta-model generation and usage for design optimization purposes. An overview on meta-model building is given by Roos et al. in [68]. In general, to build a surrogate model, a set of design points must be selected, and the high-fidelity simulation must be run on each point to obtain a set of accurate estimations of the system's response. This set of high-fidelity evaluations is often called the "training set". After that, by using regression methods, a response surface can be created. The optimum-seeking algorithm can then be sent over the response surface to look for stationary points.

Whenever an optimum point is found during the search phase, a CFD simulation is ran on the corresponding design to calculate a more accurate solution. The new point is then included in the training set, the surrogate model is updated, and the cycle starts over.

An example of this kind of surrogate-assisted, cyclically self-updating framework is represented by the IOSO technology [69]. Also, in [46] many RSM-based robust optimization studies on different fan blade cases can be found, by Nigro et al. (pp. 495-511, NASA Rotor 37) and Vinogradov et al (pp. 583-600 NPO Saturn). Kamenik et al. conducted a surrogate-assisted RDO on a turbine blade in [53]. The works of Wang [55] (pp.181-203), and Wang et al. [67] are about RDO on Rotor 37 cases, both conducted using a Back Propagation Neural Network (BPNN) model to surrogate the system's response.

An alternative to surrogate-assisted optimization is represented by gradient-based methods, such as Adjoint CFD. Despite being the fastest to converge, gradient-based methods are demanding in terms of computational expenses, since a high level of accuracy is required in gradient determination. Gradient-based methods might fail due to noise in the objective function and, in any case, they inherently lead to the detection of local stationary points. Therefore, when using these strategies, it is recommended to repeat the optimization process by starting from different points. Adjoint-based RDO can reduce the computational cost significantly. This kind of framework was used in the work of Seshadri et al. [52] on a fan blade geometry.

For what concerns the optimizers, an overview on the advantages and disadvantages of various optimization techniques for RDO is given by Will in [70]. In the field of robust turbomachinery optimization, the algorithms that are most frequently adopted to scan a response surface for optima are of the genetic and evolutionary kind, since they are well-suited to work with multi-objective optimization problems. In particular, many authors have adopted the Non-dominated sorting NSGA-II algorithm presented in [71].

Ghisu et al. in [65] used the Tabu Search algorithm developed by Jaeggi et al. [72], while Seshadri et al. in [64] adopted the Sequential Quadratic Program (SQP) which is implemented in the Smart Optimization For Turbomachinery (SOFT) toolkit [73].

Antinori et al. conducted their optimization procedures by using two different algorithms, namely Particle Swarm Optimization (PSO) and Constrained Optimization BY Linear Approximation (COBYLA), obtaining similar results in the two cases.

2.5 Choice of Uncertainty Propagation Method

According to an UMRIDA best practice guide [46] given by Pons-Prats and Bugeda (pp. 805-808) regarding the usage of uncertainty management in RDO, the following classification of uncertainty propagation methods can be made:

- Non-intrusive polynomial chaos methods
- Non-intrusive probabilistic collocation methods
- Adaptive sparse collocation methods
- Reduced basis methods
- Surrogate-based methods
- Monte Carlo-based methods
- Intrusive perturbation methods

The most accurate and reliable way to perform uncertainty propagation is represented by Monte-Carlo based techniques, which present numerous advantages, one of those being that convergence rates do not depend on the number of stochastic dimensions. When performing uncertainty propagation while dealing with discontinuities inside the parameter space, Monte Carlo methods can maintain a rather robust and accurate behaviour by virtue of their sampling-based approach. The main disadvantage of Monte Carlo methods is in their high cost: to correctly perform this kind of analysis, a large number of points is required, and it becomes practically unfeasible to analyse each point with high-fidelity methods. Furthermore, the random samples generated by a Monte Carlo simulation may not be space-filling. To speed up the process, Monte Carlo simulations may be performed on a response surface model, provided that the accuracy level of the latter is initially assessed (for example with the leave-one-out method [49]) and cyclically monitored throughout the optimization procedure. Kumar et al. used the Monte Carlo sampling method in conjunction with Gaussian process modelling [51] to perform uncertainty propagation on an axial compressor blade. This technique is called Bayesian Monte Carlo Simulation (BMCS) and has also been used in the work of Shahpar [47] and Kumar et al. [48] for robust optimization of compressor blades. In [49], the authors were able to execute a total of

100000 evaluations using BMCS, with a single evaluation requiring about 13 seconds on one processor. Another example of sampling on RSM for uncertainty propagation can be found in the work of Antinori et al. [62].

Relatively high convergence rates can be achieved by the Multi-Level Monte Carlo (MLMC) method, which was firstly introduced by Heinrich [74] and extended by Giles [75]. MLMC can be used to drive a progressive coarse-to-fine analysis of the system's response, which in CFD cases translates into using either progressively refined meshes or gradually smaller time steps while going from the lowest to the highest level. In [46], Pisaroni et al. (pp. 305-325) adopted the C-MLMC technique developed by Collier et al. [76] to study uncertainty propagation for a NASA Rotor 37 test case on a 4-level mesh hierarchy.

Non-intrusive polynomial chaos expansion of the 5^{th} order has been used by Ghisu et al. [65] to propagate uncertainties on operational variables in a multi-stage axial compressor modelled using the mean-line flow analysis method. In the same investigation the authors conducted a second optimization using Interval Analysis (IA), both methods (PC and IA) proved to be effective for robustness evaluation. PC expansion can also be efficiently coupled with gradient-based optimization methods: Kumar et al. in [46] (pp. 567-582) presented a study on the combination of adjoint formulations and non-intrusive polynomial chaos for uncertainty propagation in optimization. Stochastic collocation methods are also used as a more cost-efficient alternative to high-fidelity sampling-based methods: Seshadri et al. in [52] used the stochastic collocation method presented in [77] to conduct a design optimization on a Rotor 37 case with tip gap uncertainty. Second order non-intrusive probabilistic collocation was used by Wang et al. [67] to propagate uncertainty on outlet static pressure in another Rotor 37 case. A non-intrusive probabilistic collocation method called NIPColM was used by R. Nigro et al. in [46] (pp. 495-511) in a Rotor 37 case and in a high-pressure axial compressor stage (pp. 431-444) following the execution of a Principal Component Analysis that allowed the authors to significantly reduce the number of uncertainties. Second-order non-intrusive polynomial chaos expansion was used for uncertainty propagation by Kato et al. [60]. Seshadri et al. [64] used the derived distribution theorem for uncertainty propagation within their density-matching, adjoint-based framework.

Chapter 3

Aerodynamic Analysis

3.1 In-Service Damage and its Effects on a Turbine Blade

High Pressure Turbine (HPT) rotor blades often operate in harsh mechanical and thermal conditions. To maintain a high aerodynamic efficiency, blade loading $\Delta H/u^2$ must be kept low, thus requiring a high rotational speed. This subjects the blade to high centrifugal loads as pointed out by Glezer [78]. To grant the whole engine a high thermodynamic efficiency, high values of turbine entry temperature are sought for, now exceeding 2000K [15, 16]. Sophisticated cooling mechanisms are implemented to keep the metal structure sensibly cooler than its melting point of around 1400K [79]. The structure is designed to elastically stretch and twist due to the mechanical and thermal stresses. At its operating point, the blade reaches the desired "running" shape, which must also be designed to maintain a minimum gap between its tip and the machine's outer casing. On the surface, the HPT blade is chemically attacked by the hot gases, which cause pitting of the Thermal Barrier Coating (TBC) and then oxidization of the uncovered alloy. This erosion process worsens the heat exchange, as proved by Colón *et al.* [80]. The oxygen-rich air coming from the cooling system can also fuel the oxidization process, aggravating surface damage. Typical surface degradation modes will also include fouling [80] and cooling hole blockage [81]. Over time, the structure also experiences permanent deformations due to the creep process [35]. These will manifest principally as elongation and twist (opening-up), which may negatively affect the blade's aerodynamic performance, as well as the effectiveness of its sealing and cooling mechanics. Undesired variations in operating conditions such as outboard traverse bias [82] or engine over-throttling, add up to common geometric ones such as manufacturing variations [83, 84], defects and handling damage, accelerating the degradation and deformation processes. Shape deviation from nominal for a shrouded HPT rotor blade may have highly detrimental effects on its performance. The main loss

mechanisms in gas turbine stages have been researched and categorized since the 1950's. Many authors including Ainley and Mathieson [85], Baljé and Binsley [86], Krichakin and Mukhtarov [87], have divided turbine losses into the following six categories: (a) Profile loss, (b) Profile incidence loss, (c) Secondary flow loss, (d) Blade tip clearance loss, (e) Cooling air injection aerodynamic loss and (f) Cooling air injection thermodynamic loss.

Zaita *et al.* [88] indicate (d) to be the most detrimental to aerodynamic performance. Tip clearance loss is caused by rubbing and erosion, which depend on mission profile and/or on the number of damaging cycles. Rubbing may occur due to the blade working in hotter (off-design) conditions, or frequent "hot rotor rebursts". These take place when the engine is rapidly decelerated from a high to a low power setting, and rapidly brought back to full power. When this happens, rubbing occurs due to the different thermal inertia of the casing and disk: the former cools down faster than the latter after a temporary acceleration. As suggested by Denton in [89], the effect of an increased tip clearance on the rotor performance is firstly of inviscid nature: rotor work generation and the pressure drop across the vane is reduced by the larger leakage flow.

On the viscous side an increase in tip clearance intensifies mixing losses due to the larger secondary flow (c). Moreover, the tip geometry is designed to re-align the cavity flow in order to minimize mixing losses in the wake, and sometimes even to extract work from the said flow. The importance of re-alignment of the cavity flow for shrouded turbine rotors is highlighted by many authors including Traupel [90], Denton [89], Gier *et al.* [91] and Pau *et al.* [92]. Modifications in the tip geometry could also easily undermine these re-alignment mechanisms, further worsening aerodynamic losses.

In the available literature on the correlation between loss of tip sealing and loss in efficiency for shrouded turbine blades, much emphasis has been given to the importance of tip clearance. The present analysis on a set of out-of-service scanned (GOM) blade geometries reveals that the size of the gap between neighboring shroud platforms is in fact of even greater relevance, in determining large amounts of performance loss. An increase in the shroud-side gap, which is observed in the majority of the GOM scans that are analyzed here, can be caused by a combination of different thermo-mechanical factors: (a) Rotation of the shrouds due to aerofoil twisting, (b) Wear due to contact between the shroud sides, (c) Erosion by the leakage flow passing through the gap and (d) Hot metal curling or bending under flow pressure and heat loads.

On the other hand, when dealing with deformation of the aerofoil shape, the most prominent inviscid losses stem from alterations of the throat area and blade angles [85, 93, 94]. Conversely, the principal viscous loss mechanisms that are fueled by aerofoil shape deviation are related to friction and mixing (i.e., boundary layer and shear layer

losses). In particular, trailing edge losses on the rotor are often found to be the most prominent contribution to HPT stage entropy generation, accounting for 1/3 of the total losses for a given HPT rotor design [89, 95, 96].

This section of the thesis focuses on the relation between aerodynamic performance loss and shape deviation for a large set of in-serviced (scanned) shrouded HPT rotor blades. This work is part of a more comprehensive investigation on the root cause analysis of the damage effects and its aero-thermal consequences. The aim of this part of the work is to:

- Provide an insight on the main damage modes experienced by a series of shrouded turbine blades during in-service operating conditions.

- Analyze the aerodynamic loss mechanisms that take place as a consequence of the measured shape deviation.

- Investigate any correlations between shape deviations and the performance loss.

This analysis is carried out through a series of high-fidelity CFD simulations. Aerodynamic performance indices for the scanned rotor blades are compared against the corresponding nominal ones. Monitored quantities include HPT stage efficiency, HPT rotor work production, capacity, and reaction values. In-service shape deviations for each scanned blade with respect to the Design Intent (DI) are obtained using an inverse mapping technique [33] and expressed with a set of parameters within the design space provided by the proprietary Rolls-Royce meshing and parametric design tool PADRAM [97]. PADRAM was also used to calculate other relevant quantities such as throat area, leading edge and trailing edge metal angles, and stagger angle. Shroud damage of each GOM scan is measured at five different points on the blade structure. The one-and-a half stage computational domain, comprising of a high-pressure stator, high pressure rotor and intermediate pressure stator, is meshed with a hybrid strategy using PADRAM and BOXER [98]. Rolls-Royce’s proprietary unstructured RANS CFD solver HYDRA [99] is used to perform all the aerothermal calculations.

3.2 Numerical Setup

3.2.1 Geometries and Boundary Conditions

In the present work, CFD simulations were run on a one-and-a-half stage computational domain, as shown in Fig. 4. The difference between the cases is represented by the high-pressure rotor (HPR) geometry, which in one case is the design intent (DI) and in the other cases is obtained from scans of a set of in-serviced blades. One hundred and twenty scanned blade geometries were used for this analysis, originally belonging to eight different engines. All the shapes are provided in cold conditions by Rolls-Royce plc in the form of a de-featured CAD file for the DI (without cooling geometry) and high-resolution GOM stereolithography (STL) files for the scanned blades. Before meshing, a cold-to-hot transformation provided by the manufacturer is applied to every rotor blade, to bring the GOM shapes to running conditions. The transformation process involves a translation along the machine axis, followed by a non-uniform scaling relative to a point located on the blade hub.

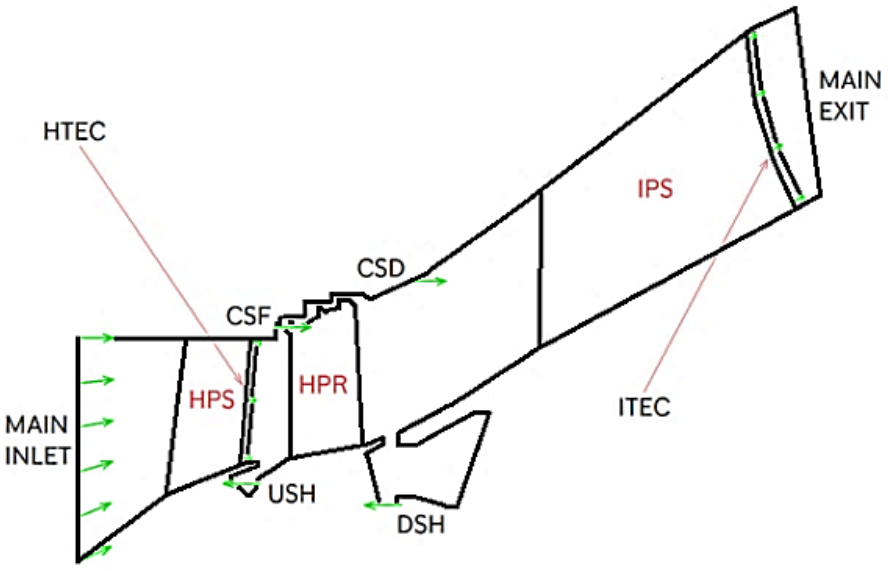

Figure 4: Schematic of the computational domain. The green arrows indicate an inlet boundary; symbols are defined in the nomenclature section – Picture is distorted and not to scale

Stator geometries were provided in the form of a BDF, which is a proprietary Rolls-Royce format, being already in hot conditions. Film-cooling “strip” models such as the

ones used and defined by Occhioni *et al.* in [100] were applied to the HPR and HPS geometries. Both HPS and IPS have TE cooling slots (HTEC and ITEC in Fig. 4). Other secondary flows were introduced in the rotor domain and include the casing cooling inlets positioned upstream and downstream of the rotor blade CSF & CSD and the inner cavity flows USH & DSH. All these inflows are visible in Fig. 4. Compared to the DI geometry, the GOM scans display elongation and twist. The shroud platforms also appear to be slightly rotated following the twist of the blade beneath. The blades also display wider tip clearances, with clear evidence of rubbing, and the gaps between the sides of neighboring shroud platforms are larger than nominal. Simulations were performed on single passages, by imposing periodic boundary conditions on either side of the blade domain for each one of the three rows.

3.2.2 Meshing

For the stator domains, construction of the multi-block structured computational grids was done with PADRAM. Computational grids around the rotor geometries were generated with BOXER with a body-fitted approach.

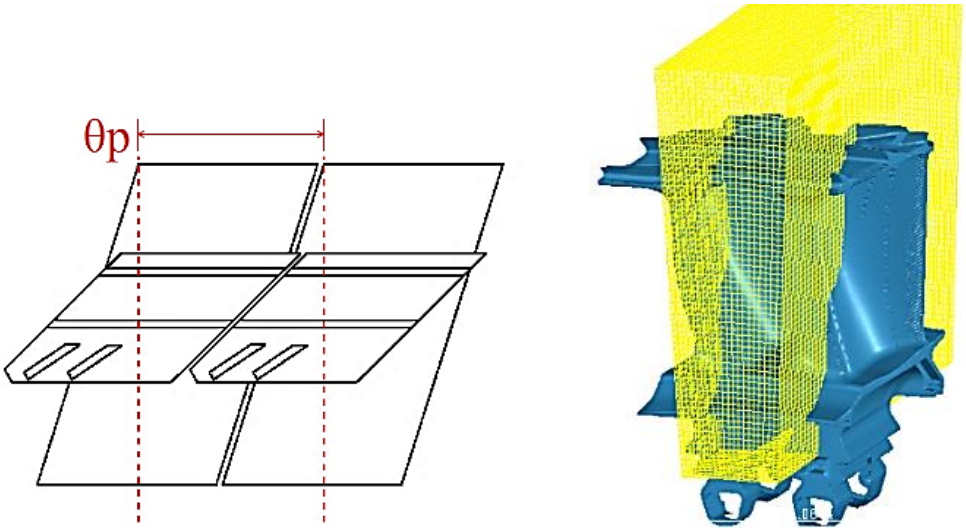

(a) (b)

Figure 5: Meshing of the rotor domain. (a) Top view schematic of the rotor row passage. The rotor domain consists in a straight cylindrical sector of amplitude θp, enclosing two complementary portions from a pair of identical rotor blades. The "bounding box" is shown in (b)

The reason for using a different meshing tool for the rotor is that BOXER allows to mesh directly on the STL file, and to entirely capture the scanned geometric features. BOXER meshes were generated within a bounding box that has the shape of a cylindrical sector of angular range θ_p, limited to a minimum and maximum radius. The axis of this cylindrical sector was coincident with the turbine axis, and the box could not be skewed laterally (in a helical way) to follow the curvature of the blade. Due to the skewness of the geometry, the cylindrical sector of amplitude θ_p on the rotor annulus needed to include parts belonging to two adjacent blades, as shown in Fig. 5. For this reason, while the stator PADRAM meshes only host a single blade each, the BOXER ones for the rotors include two complementary portions from a pair of identical blades. For the rotor meshes, 20 O-grid prismatic layers were generated around the blades as shown in Fig 6a, where grid refinement can be seen around the blades and in the wake region.

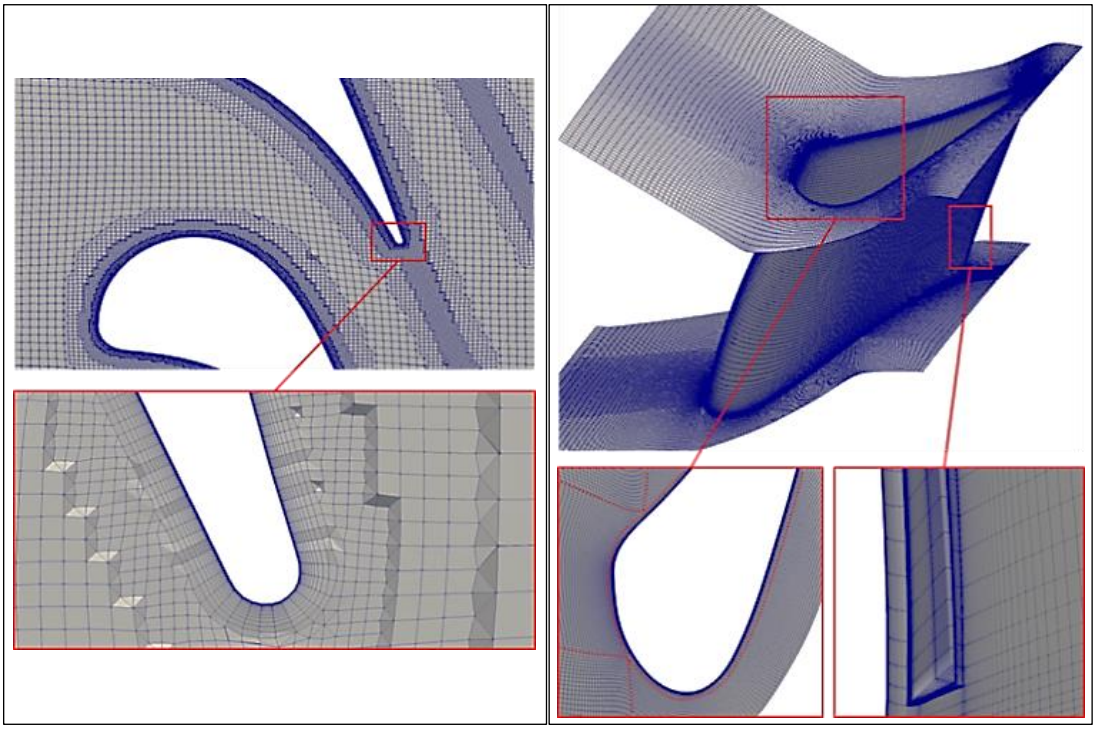

(a) (b)

Figure 6: Radial section of a rotor BOXER mesh around the DI rotor passage (a) and view of the HP stator PADRAM mesh (b) with close-ups on the leading edge (blocking highlighted in dashed red curves) and the cooling slot indicated as "HTEC" in Figure 1. HP and IP stators were meshed following the same procedure

Local refinement was applied to the shroud region, where particular attention was directed to the shroud gap and to fins and fences. The BOXER meshing process was prepared once within the software's GUI and automated for the other 120 blades using a "lua" script. A single meshing run for the rotor domain required 190 core hours. PADRAM generates, in a few seconds, a multi-block H-O-H structured grid as shown in Fig. 6b.

The PADRAM domain follows the curvature of the blade, with the whole mesh structure being oriented along the flow direction. 14 O-mesh layers were specified for both stator domains. For all the three domains, first cell height was set to a dimension of 10^{-6} meters after a series of tests, allowing for a y^+ lower than 1 on all the surfaces. Before analyzing the 120 GOM blades, a mesh independence study is carried out on the datum-blade computational domain.

For the BOXER-meshed rotor domains, grid density was modified by increasing the resolution of the initial bounding box. For the stator PADRAM meshes, the modification was enacted by increasing the number of nodes along the aerofoil sides. Mesh densities for the different cases are listed in Tab. 1.

Table 1: Grid densities used in the mesh independence study

Case	Rotor	BB cells (HPR)	Side Nodes (HPS,IPS)	Cells
D30	DI	30	90,120	$27.7 \cdot 10^6$
D35	DI	35	105,140	$37.8 \cdot 10^6$
D40	DI	40	120,160	$50.3 \cdot 10^6$
G40	GOM	40	120,160	$42.4 \cdot 10^6$

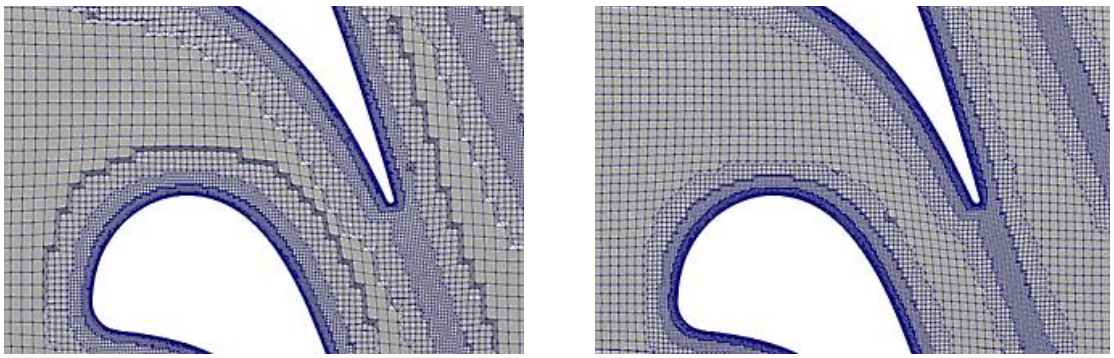

(a) (b)

Figure 7: Sections of two of the rotor BOXER meshes used for the grid independence study (see Table 1) – D30 (a) and D40 (b)

The values included in the case nomenclature of Tab. 1 indicates the number of cells in BOXER's bounding box (e.g. D35 = DI geometry, 35 cell BB span). The coarsest and finest DI rotor meshes used for this study are reported in Fig. 7. The 40-BB-span GOM scan "G40" mesh is also included in the Table 1 to note that, for the GOM cases, cell count is slightly lower than the DI one for the same cell span, due to the wider clearances in the shroud region. Tab. 2 contains the results for each case in relation to all the quantities of interest considered. Percentages of variation for each value are presented in relation to the corresponding values obtained for Case D40.

Table 2: Variations of Output Quantities with respect to Case D40

Case	Capacity	Spec. work	Efficiency	Reaction
D30	0.0077%	0.06%	0.064%	-0.157%
D35	0.0066%	0.02%	0.030%	-0.071%
G40	0.8095%	-4.58%	-3.670%	-18.320%

It can be seen from the variations reported in Tab. 2 that the differences in the output quantities due to grid density (Cases D30 & D35) are significantly smaller than the ones due to shape variation (Case G40). Ultimately, the 40-cell approach was adopted because it allowed for a greater resolution of all the surface features, increasing the fidelity of the analysis.

3.2.3 Simulation Technique

All the CFD simulations presented here were conducted with HYDRA, which is a proprietary Rolls-Royce density-based unstructured solver. The steady-state 3D Reynolds-Averaged Navier-Stokes (RANS) equations were solved with a single-grid implicit scheme. This allowed to use a relatively high CFL of 20. This technique is found to provide the best convergence levels of around 10^{-12} for the residuals of the momentum equations. A residual drop of four orders of magnitude, with respect to the initial solution values, was achieved in all cases, for every conservation equation. The *k-ω SST* turbulence closure model was adopted. Each CFD simulation had a cost of approximately 2400 core hours and was carried out on Rolls-Royce's HPC clusters, using 96 cores. At the main HPS inlet, a 1D boundary condition was used to define radial distributions of total pressure and total temperature. Fixed-mass-inflow boundary conditions with total temperature, total pressure and injection angle settings were

placed at each one of the secondary inlets shown in Fig. 4 (CSF, CSD, USH, DSH). Conditions of the same kind were used to define the slot-cooling inlets (HTEC and ITEC) and the film cooling models. A radial distribution of static pressure was imposed at the IPS main exit.

3.3 Uncertainty Quantification

3.3.1 Description of the technique

To express the geometric deviation in terms of Engineering Parameters (EPs), a fully digital reverse engineering procedure called “inverse mapping” was used [33]. The outcome of this procedure was the definition of each GOM geometry as a superposition of the DI geometry plus a shape deviation vector. The inverse mapping process is carried out by means of an automatic optimization loop comprising the Rolls-Royce in-house software tools P2S, PADRAM and SOFT.

P2S is a distance-evaluation tool used to calculate the “distance field” (see Fig. 8b) between two blade geometries (a total average value is passed to the optimizer). PADRAM is the same tool that is being used to mesh part of the computational domain, and that can also be used to morph the geometry using a wide variety of methods. SOFT (Smart Optimization for Turbomachinery) [73] is a Rolls-Royce proprietary tool that contains various optimization libraries. The optimization loop is shown in Fig. 8a.

P2S receives as input the target shape (which in this case is a particular GOM scan stereolithography file), the DI blade geometry and a set of design parameters that describe shape deviation. It calculates the distance field between the two and passes it on to SOFT. The latter then modifies the design parameters according to the selected optimization routine and instructs PADRAM which in turn morphs the DI shape accordingly, through engineering parameters (EPs)-based morphing. PADRAM EPs are a set of geometric parameters, each describing a different mode of aerofoil shape deformation. Examples of these modes are depicted in Fig. 9: each EP describes a modification to the control section’s shape either by rigid translation/rotation of the whole aerofoil, or by re-cambering deformations. XCEN is a rigid-body movement along the machine axis, DELT is a rigid-body movement in the circumferential direction (normal to the machine axis in the section plane), SKEW is a rigid-body rotation of the section around a radial axis passing through the quarter-chord position, LEMO and TEMO respectively involve re-cambering deformation at the leading edge

and trailing edge of the blade, TECA is a trailing-edge chord extension and EXBA is a movement of the trailing edge, similar to TEMO but much more localized.

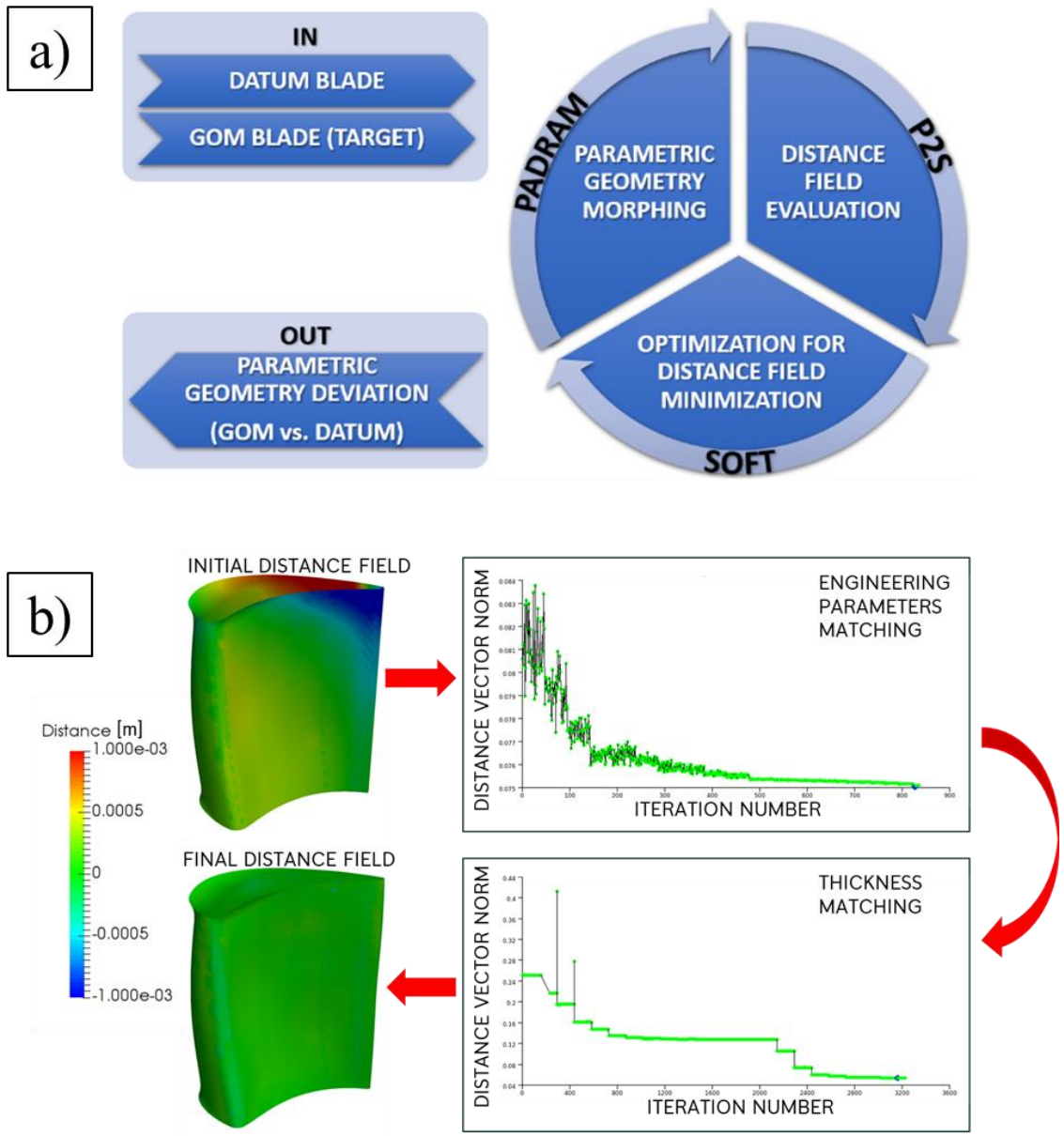

Figure 8: PADRAM-P2S-SOFT optimization loop for reverse engineering of turbomachinery blades (a) and a scheme showing how the distance field is affected by the multi-phase iterative matching (b)

As indicated in Fig. 8b, the matching process happens in two main phases, namely the engineering parameters matching and the thickness matching. This allows to firstly tackle the large-scale deformations with the design space shown in Fig. 9 and then to locally adjust blade thickness by introducing bump functions locally on the blade surface. The bump functions are applied on a matrix of 180 control points that are evenly distributed on the whole surface of the blade.

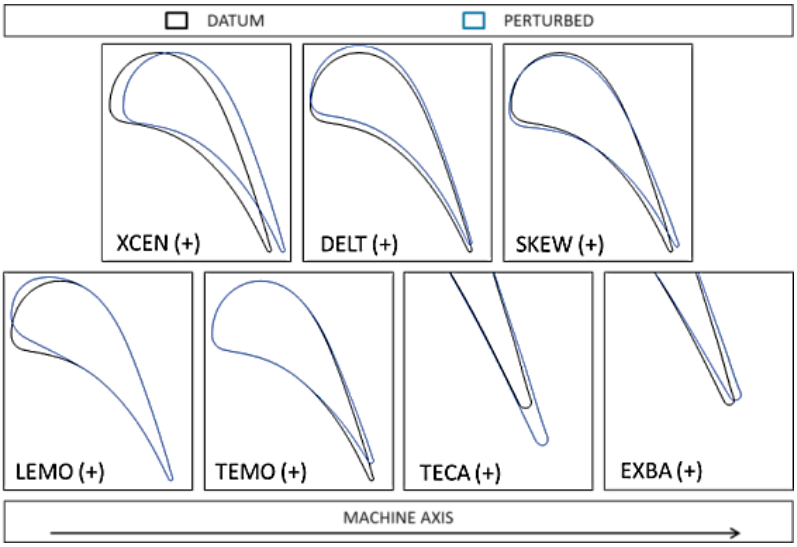

Figure 9: PADRAM Engineering Parameters (EPs) used in the present analysis – example of each EP's effect on a turbine blade section

The iterative process continues until a termination criterion is met, i.e., when no further reduction in the distance field between the two geometries can be obtained, which means that an optimal match between the GOM scan and the distorted DI has been obtained. The shape modification applied to the DI is parametric, since the morphing was done by intervening on a set of compact design parameters and describes the shape deviation from nominal of that target GOM. For a more detailed description of this process, the reader can refer to [33]. Convergence of the matching process can be judged by the final values of the P2S distance field. In this case, after the maximum match-to-target distance goes below 0.1 millimeters, the inverse mapping run was considered converged. For the present case, the shape deviation vector was composed of 35 values, due to the adoption of 7 EPs on 5 constant-span "control sections". The sections are evenly distributed along the blade's spanwise coordinate. A spline-based interpolation algorithm ensures a smooth shape transition in between consecutive control sections. The complete process required around 48 hours, using one core per blade (120 cores). After the reverse-engineering process, PADRAM is also capable of

generating the camber line of each GOM scan match. This data was then used to calculate the inlet and exit metal angles, and the stagger angle of each blade.

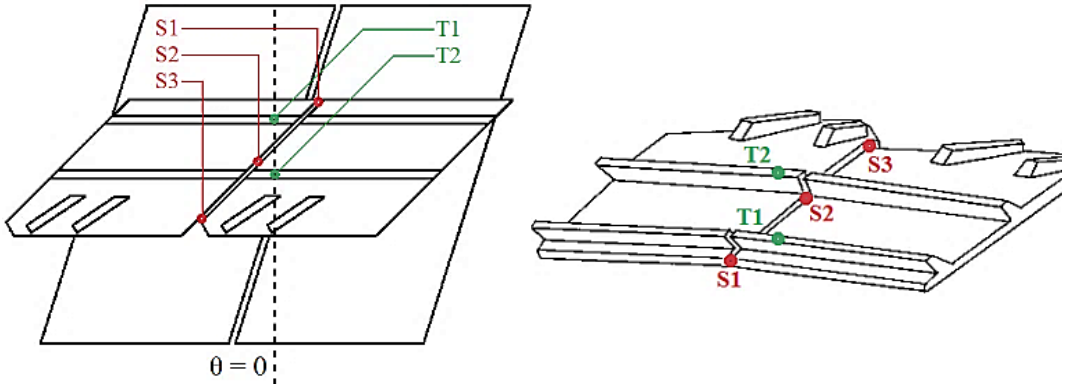

Figure 10: Top view schematic of the rotor row with measurement points for quantifying the shroud damage

In order to accurately measure the deformation of the blade shroud, a different approach was used. Measurements were taken on each GOM blade at different points in the shroud region, to gather information on the gaps between the fins and upper casing (tip gaps at T1, T2) and the gap between neighboring shroud platforms (shroud gaps at S1, S2, S3) as indicated in Fig. 10. PADRAM was also used to measure the throat area formed by each GOM blade.

3.3.2 Inverse Mapping Results

EP distributions pertaining to one of the engines analyzed are shown in Fig. 11a. All the EP distributions, including the ones not shown in Fig. 11, are used in the correlation study presented in section 3.4 of this work.

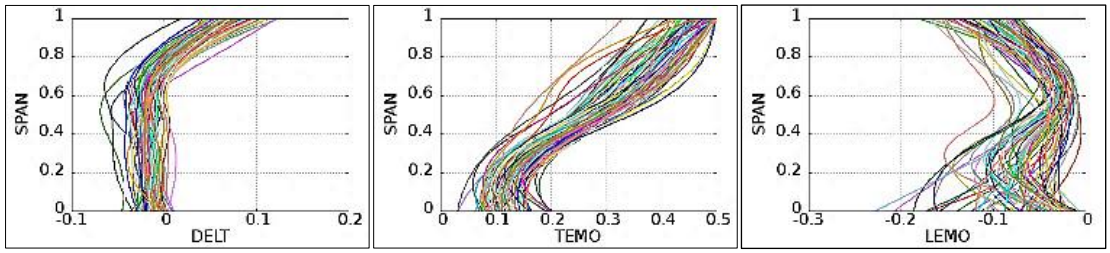

(a)

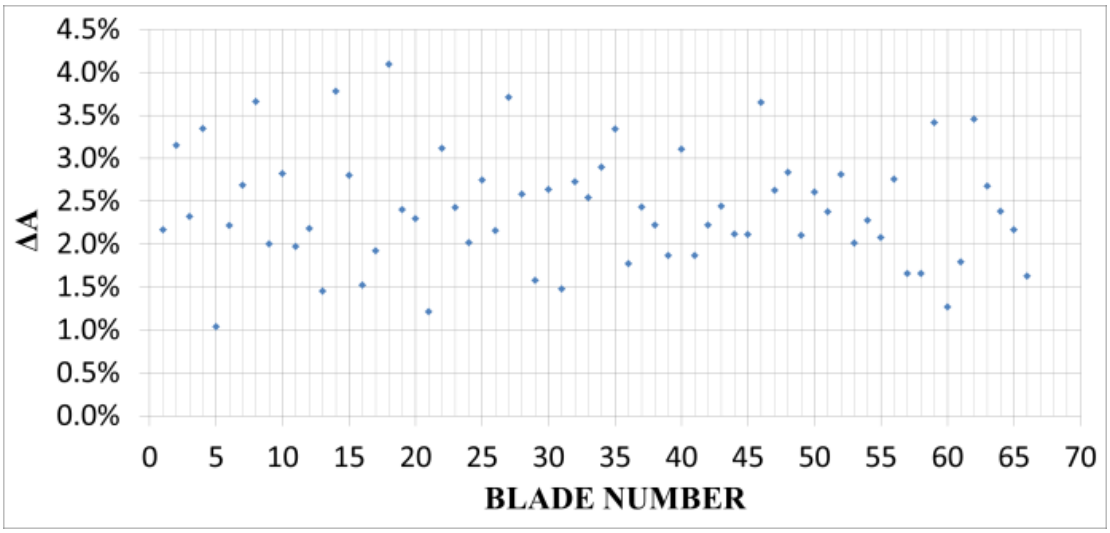

(b)

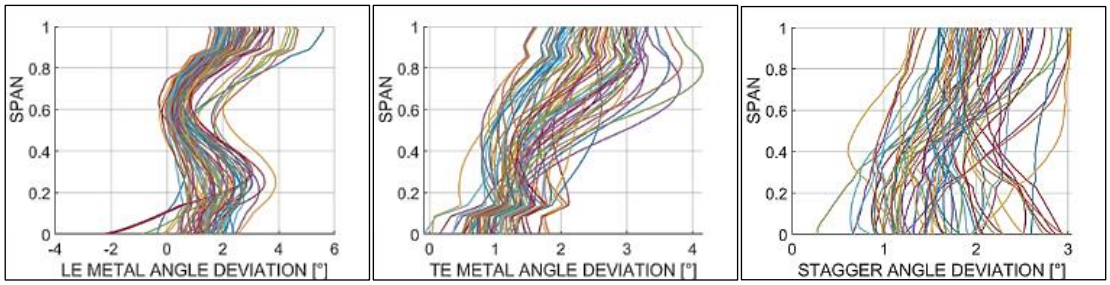

(c)

Figure 11: Engine n. 5 HPT rotor blades: (a) parametrized aerofoil shape deviation along the spanwise direction in terms of PADRAM EP where each curve represents a blade, (b) throat area variation from nominal and (c) spanwise distributions of the blade angles' variation from nominal

In the plots in Fig.11a, the EP values are in degrees. By observing the EP curves, most of the blades appear to display the same predominant modes of shape deviation. These, referring to Fig. 9, include positive tangential lean "DELT" (towards the suction side); and positive trailing edge movement "TEMO".

The blades also display a certain amount of trailing edge chord adjustment "TECA", particularly at the top half of the span. For a correct interpretation of these large TECA values, the interaction between TEMO and TECA must be taken into account. When positive TEMO is present, the trailing edge of the blade section is moved in the circumferential direction. As shown in Fig. 9, the section's chord becomes proportionally shorter due to this. The optimizer then compensates this effect by introducing positive TECA, to restore the correct chord length. Indeed, the typical GOM scan's chord length is not dissimilar to the DI one as can be seen in Fig. 15 where the black curves represent DI blade sections, and the red curves represent the GOM ones. Due to this interaction with TEMO, the large TECA values are not to be interpreted as a direct consequence of deterioration, but rather as a consequence of the choice of design space used for this parametrization. The shape deviation captured by the inverse mapping process is mostly concentrated in the upper half of the blade span. Fig. 11b shows a subset of the measured data on throat area variation from nominal. Interestingly, all the blades display an increase in throat area. The group appears to sit with significant dispersion around an average of +2.4%. The plots in Fig. 11c display the geometric deviations from nominal in terms of leading edge metal angle, trailing edge metal angle and stagger angle. The plot in Fig. 12 presents the variations from nominal of average tip gap (mean value of T1 and T2) and average shroud gap (mean value of S1, S2 and S3) values, measured on the GOM scans.

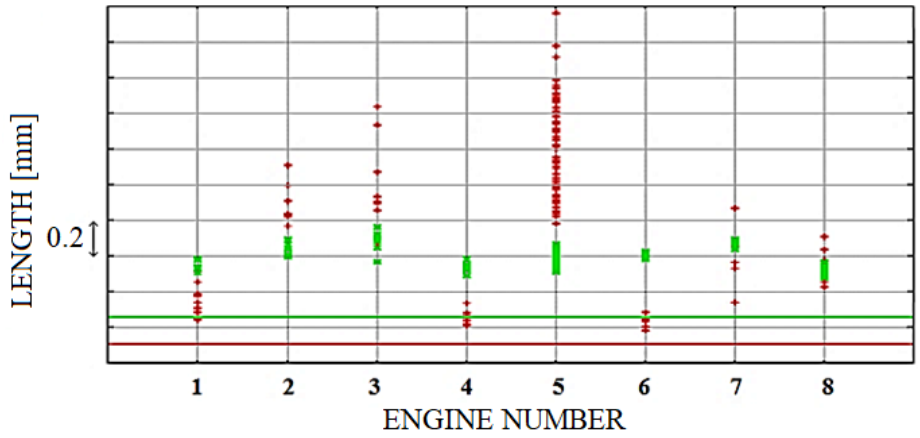

Figure 12: Average tip gap (green) and shroud gap (red) of GOM rotor shrouds divided by Engines: (1 – 8) – the horizontal lines represent the DI values

The significant increase in shroud gap that is observable in most of the GOM scans is caused by a shroud platform rotation around a radial axis. This rotation takes place as a consequence of the TEMO (blade geometry perturbation) below the shroud platform (i.e. the blade twists open at the trailing edge and this is followed by the shroud). Fig. 13 shows a top view of the DI shroud geometry that has been rotated to replicate the twist found on one of the GOM scans. For small displacements, it is found that the shroud gap increases by 0.43 millimeters per degree of rotation around a radial axis passing through the point shown in Fig. 13.

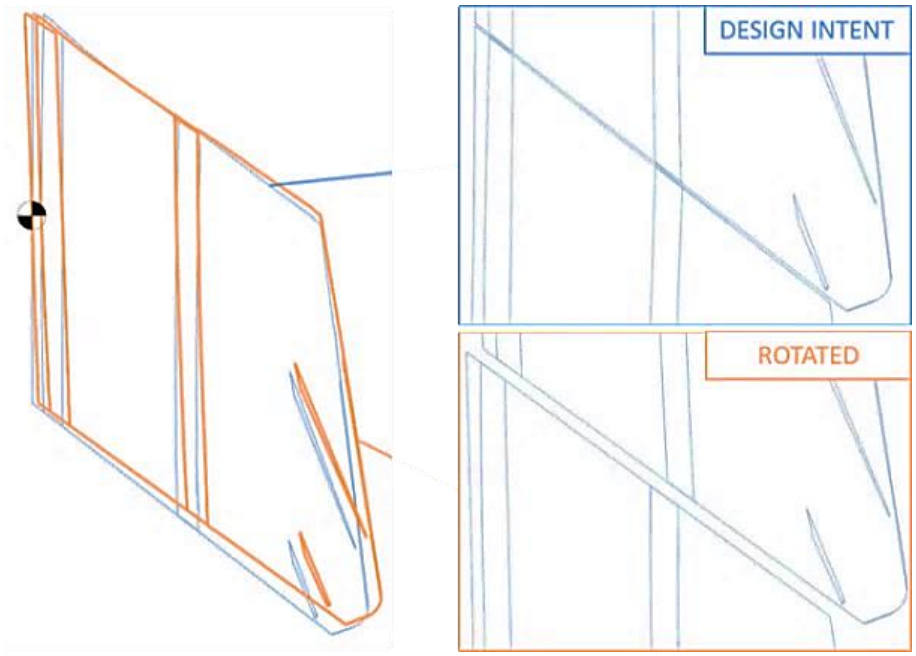

Figure 13: Effect of TEMO-induced shroud rotation, single blades on the left; passage pairs on the right (close-up on the gap region)

3.4 CFD Results and Sensitivity Analysis

3.4.1 Performance Levels of the In-Serviced Blades

As illustrated by the plots in Fig. 14, the results indicate that all the GOM scans suffer a significant aerodynamic performance loss with respect to the DI.

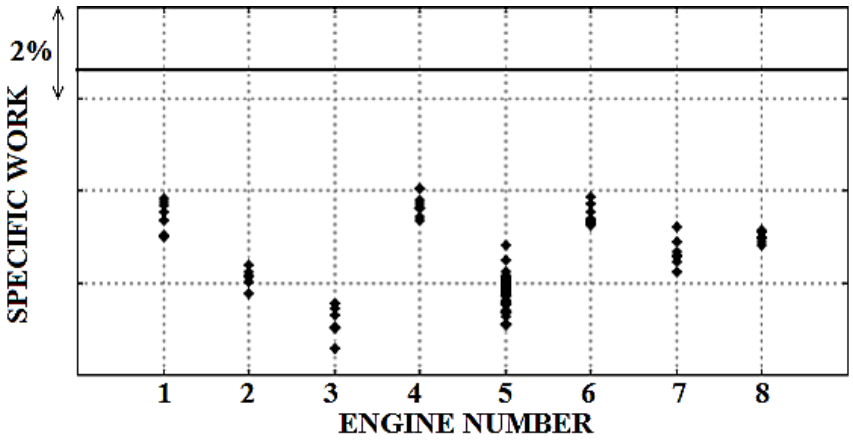

(a)

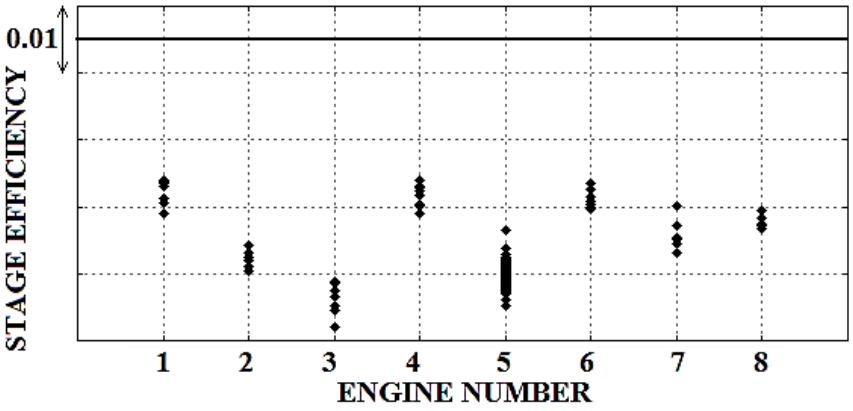

(b)

Figure 14: Aerodynamic performance indices for the GOM scans (points) compared with the DI values (lines) - Specific work production [J /kg] (a) and HPT Stage efficiency (b) as defined in eq. (1)

The main metric that is used in this work to evaluate the aerodynamic performance for each case is the HPT stage isentropic efficiency, which will henceforth just be referred to as "efficiency". Its definition is reported in Eq. 8.

$$\eta = \frac{\sum_{i=inlets}(\dot{m}H_0)_i - (\dot{m}H_0)_{exit}}{\sum_{i=inlets}(\dot{m}H_0)_i - (\dot{m}H_{0\_ideal})_{exit}} \tag{8}$$

This quantity was calculated by placing monitors at all the flow inlets shown in the scheme of Fig. 4, and at the high-pressure rotor exit. Through these monitors, mass flows and total enthalpy values were collected. The total enthalpy values are calculated by mass-averaging the total pressures and temperatures at each boundary. In Eq. 8, the

terms $\dot{m}$ indicate the mass flows and H_0 the total enthalpy values. The term indicating the ideal exit total enthalpy, which can be seen in the denominator of Eq. 8, is calculated by isentropically expanding each gas stream to the mass-averaged total pressure of the mainstream rotor exit.

Observing the plots in Fig. 12 and Fig. 14, it is interesting to note that the different engines display a drop in performance that looks remarkably proportional to the amount of shroud damage. The following part of this section contains two different CFD analyses: the first one focusing on the effects on performance due to shroud damage only; the second one focusing on the impact of the blade deformation only.

3.4.2 Sensitivity to Shroud Damage

The aim of this part of the study is to assess the importance of shroud damage only in determining the large amounts of efficiency loss observed: one additional CFD simulation was carried out on a modified DI blade where only the shroud was altered to reproduce the damage of one of the GOM scans. The modified DI blade is henceforth referred to as the "hybrid" design or "HB" due to its geometry being a hybrid between a GOM blade "GS" and the DI. Results from this comparison are presented in Tab. 3: more than 80% of the observed stage efficiency loss is associated to shroud damage only. This is true even for a case where there is substantial aerofoil shape deviation, as depicted in Fig. 15. The increased leakage promotes a lower static pressure throughout the span in the "HB" and "GS" rotor vanes. This can be seen in the non-dimensional static pressure contours of Fig. 16.

Table 3: Hybrid Blade and GOM scan – Variations with respect to DI

Case	Capacity	Spec. work	Efficiency	Reaction
HB	+0.60%	-4.12%	-3.29%	-15.11%
GS	+0.81%	-4.58%	-3.67%	-18.33%

As a result of the lower static pressures throughout the domain, the flow-field near the damaged blades' suction sides is significantly slower. This can be seen from the relative Mach number contours in Fig. 17.

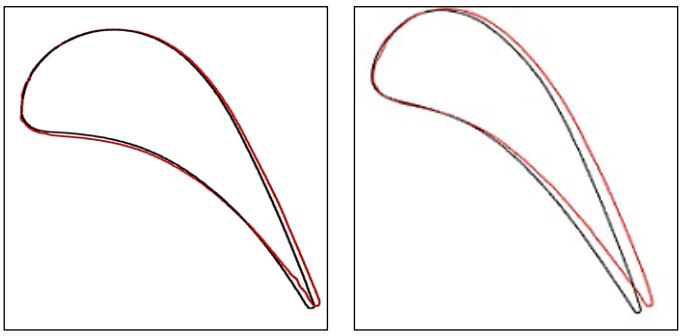

Figure 15: Aerofoil sections of the two rotor blades in Table 3 at different percentages of span – 50% (a) and 90% (b) – hybrid blade "HB" in black and GOM scan "GS" in red

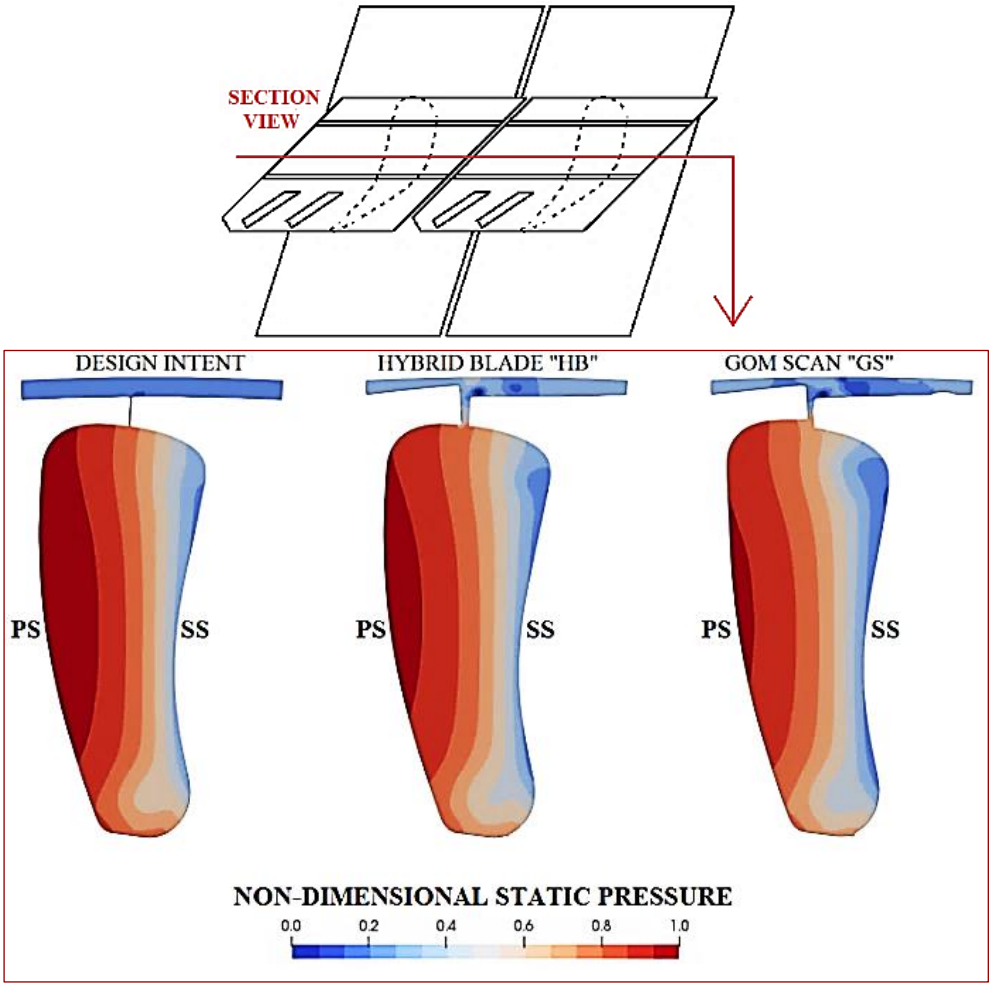

Figure 16: Non-dimensional static pressure contours at a mid-chord axial section of the rotor passages

Due to this phenomenon, the shockwaves on the “HB” and “GS” cases move upstream, and an early diffusion of the suction-side flow can be seen at all span sections. This causes the early rise in static pressure as the flow approaches the trailing edge along the suction side. This effect is shown in Fig. 18 where a non-dimensional force (obtained by integrating the pressure difference between pressure and suction sides) is plotted for the three cases considered. The net force exerted on the blade by the surrounding flow is proportional thus to rotor work production. While, expectedly, HB and GS show similar behaviors near the tip, it is interesting to note that the two present similar values also throughout the span. Hence, it can be concluded that the effects of shroud deformation extend their influence also at lower blade heights, while the effects of blade deformation on work production are small compared to those caused by the shroud damage. An additional loss factor related to shroud damage pertains to modifications to the cavity flow re-entry conditions.

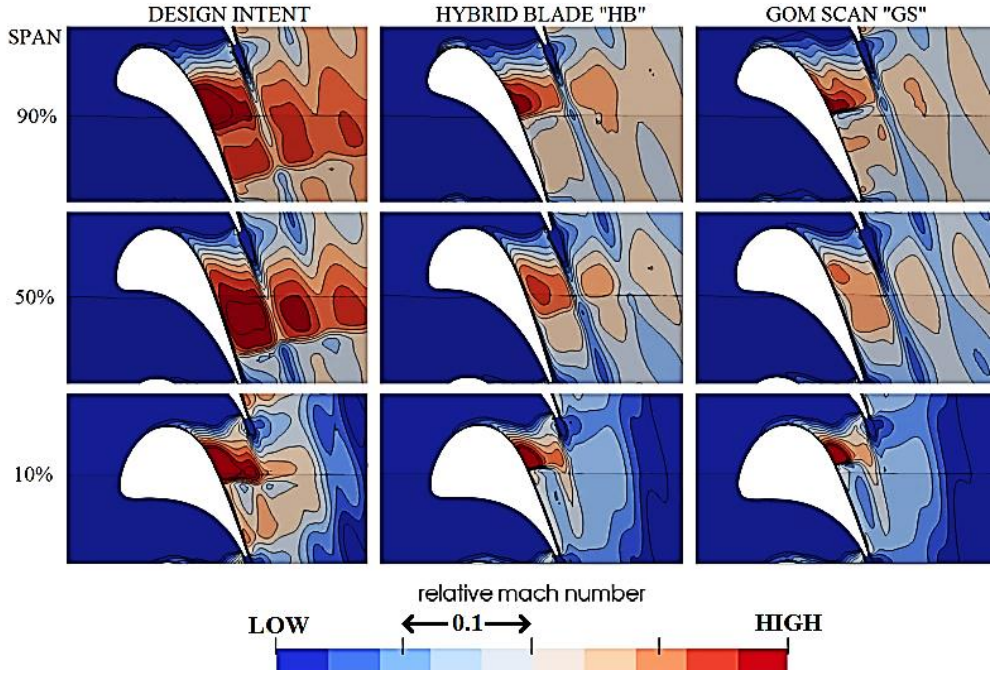

Figure 17: Relative Mach number contours of the three blades at different span-wise sections

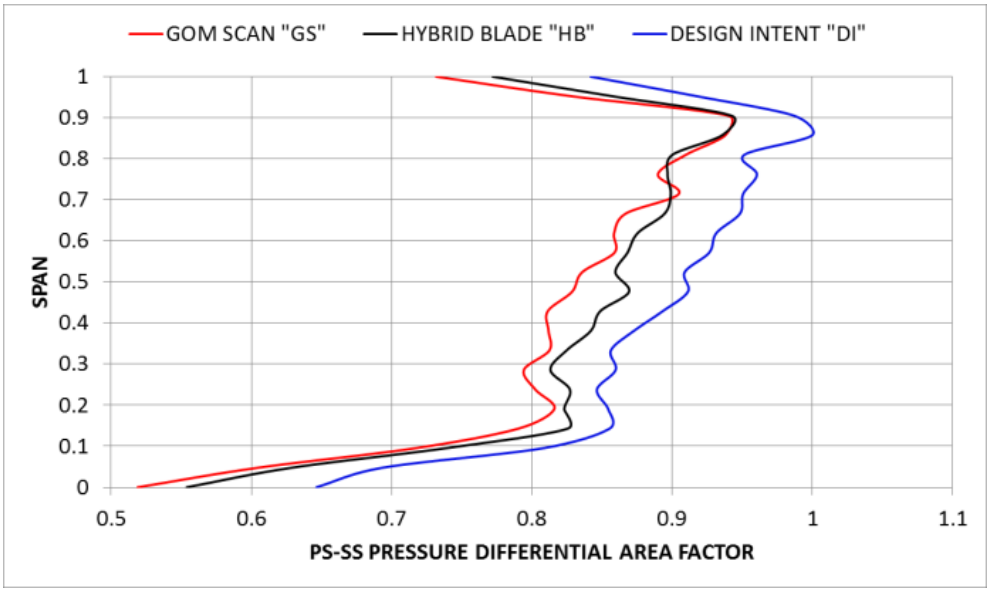

Figure 18: Non-dimensional blade force as a function of span - from hub wall (0) to shroud wall (1).

The contour plots of Fig. 19 show the relative tangential velocity and axial velocity fields immediately downstream of the rotor's trailing edge. The three most prominent flow structures displayed in the contours of Fig. 19 are the leakage vortex (1), and the two passage vortices (2,3) formed by the rotor. The "HB" and "GS" leakage vortices display significantly more intense velocity gradients with respect to their passage flows. This indicates that the shroud geometry is failing to properly redirect the cavity flow, with the effect of higher mixing losses. The "GS" flow-field displays the effects of the aerofoil TE re-cambering visible in Fig. 15. This is particularly evident in Fig. 19a at higher spanwise positions, where the flow-field leaving "GS" also has a smaller tangential component due to the reduced exit angle. To investigate on the correlation between HP stage efficiency drop and the parametrized shroud damage, a combined shroud damage variable "SDV_{ETA}" was constructed through a linear combination of the 5 parameters depicted in Fig. 10 (S1, S2, S3, T1, T2). To determine the best set of "fitted" coefficients for the shroud damage parameters, a Python-based random search algorithm was coded by the author and used for the purpose at hand. Random search was used instead of more complex method because of the limited number of variables (5) involved in this regression study. For all the coefficients, a parameter space ranging from 0 to 1 was explored. In this case, the search was confined to only positive-sign coefficients, because all the associated parameters were always observed to give a positive contribution to the efficiency loss.

A constraint was placed on the random generation algorithm to ensure that the sum of the coefficients adds up to one and avoid duplicate solutions (i.e. random coefficient

vectors that are multiples of each other). The random search was repeated several times to ensure that a similar solution (in terms of "ranking" of the various coefficients) was consistently found.

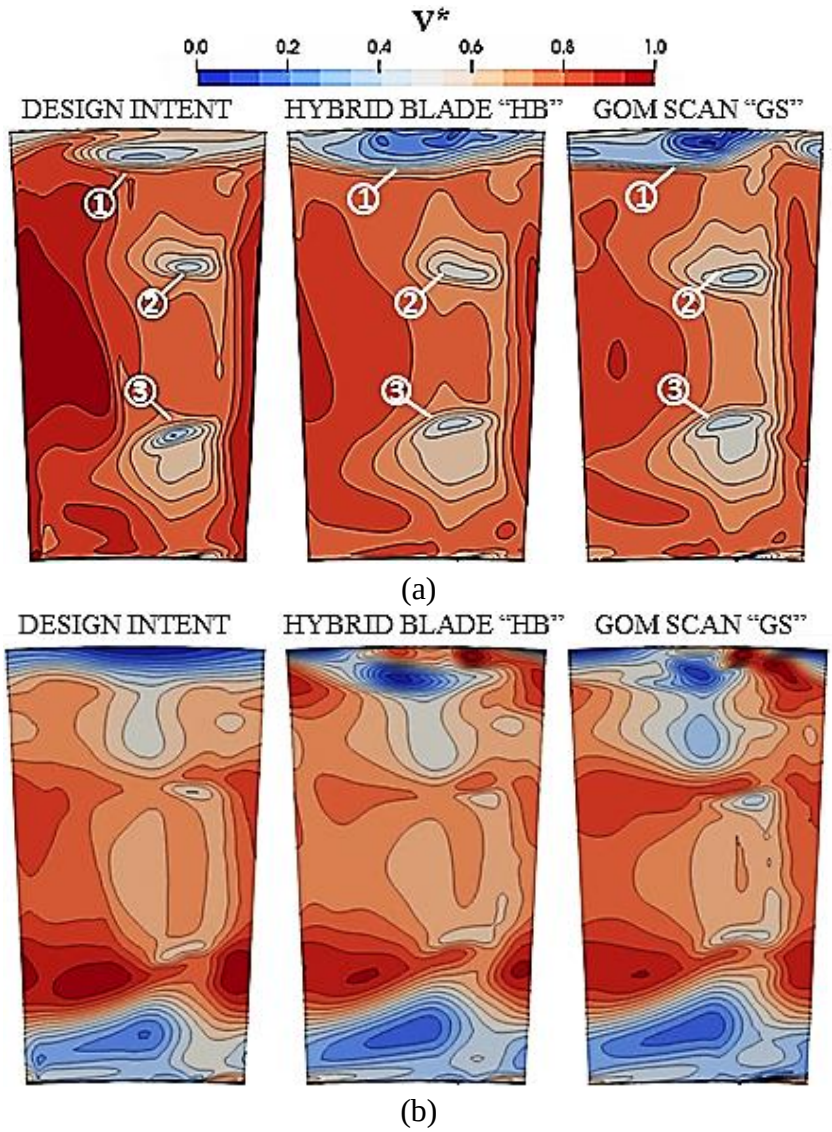

Figure 19: FLOWFIELD Contours at an axial section placed 0.1Cax downstream of the rotor trailing edge SHOWING non-dimensional relative tangential velocity (a) and non-dimensional axial velocity (b). The numbers in (a) indicate the leakage vortex (1), the upper (2) and lower (3) passage vortices.

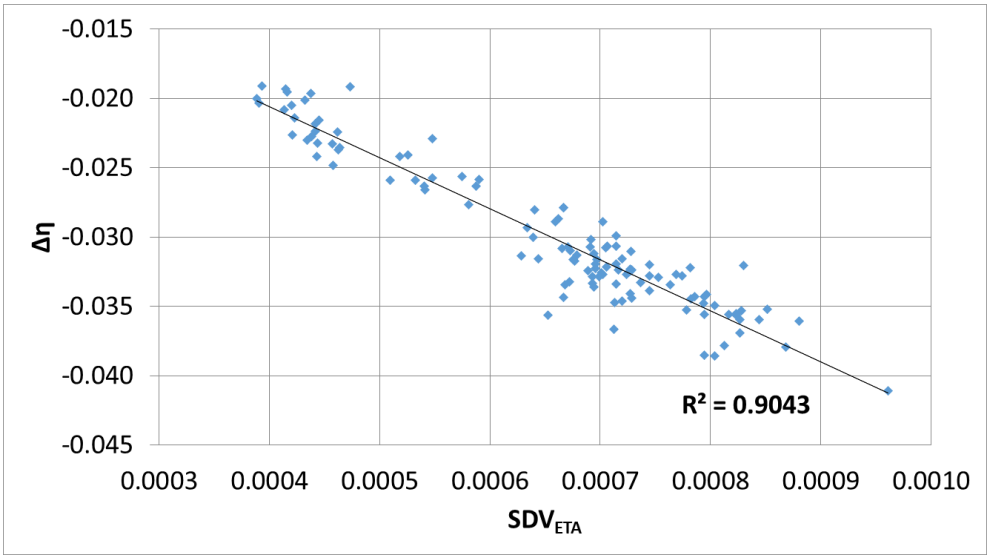

Figure 20: Stage efficiency delta of the GOM scans with respect to the DI displays linear correlation to the combination of shroud damage parameters SDV_{ETA}.

Tab. 4 reports the coefficient values that allow for the best linear correlation (R^2 = 0.9043) of the combined variable SDV_{ETA} against stage efficiency drop. The corresponding formulation for the variable is thus the one reported in Eq. 9. The distribution of SDV_{ETA} against HP stage efficiency drop is plotted in Fig. 20. The linearity trend is evident.

Table 4: Shroud Damage Variables Definition

Parameter	S_1	S_2	S_3	T_1	T_2
Coefficient	C_1	C_2	C_3	C_4	C_5
SDV_{ETA}	0.057	0.365	0.008	0.342	0.227

$$SDV_{ETA} = 0.057\,S_1 + 0.365\,S_2 + 0.008\,S_3 + 0.342\,T_1 + 0.227\,T_2 \qquad (9)$$

From this correlation analysis, it can be concluded that the "wear points" that are most relevant to performance are represented by the mid-chord shroud gap "S2" and the front fin tip gap "T1". In third position, the second fin tip gap "T2" contributes for about 20% of the observed correlation, while the front and rear shroud gaps "S1" and "S3" appear to only play a marginal role. The high importance of the shroud gap opening at the position marked as "S2" is confirmed by flow-field visualization. Fig. 21 shows a section obtained by cutting the domain in between the two neighboring shroud

platforms, on a GOM rotor passage: the shroud cavity upstream of the rear fin is pressurized by the flow leaking over the front fin.

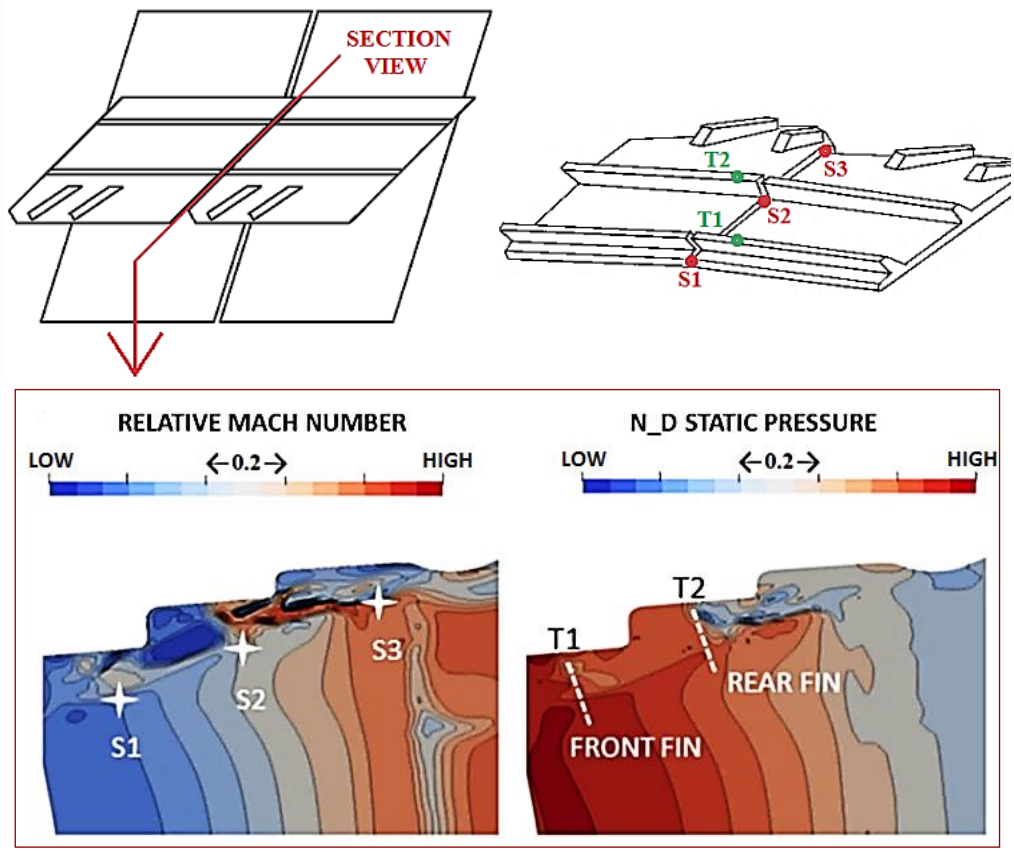

(a) (b)

Figure 21: Flow-field in the shroud gap of a GOM scan – Relative Mach number (a) and Static pressure (b)

The high-pressure flow below the front shroud platform does not encounter a high enough pressure differential to escape through the shroud gap in the "S1" position. Similarly, there is no significant pressure differential between the passage and cavity flows at the rear portion of the shroud platform (point "S3"). By contrast, there is a significant pressure differential driving the crossing of the passage flow below "S2". From there, the main gas escapes through the shroud gap at high speed, emerging into the low-pressure section of the shroud cavity, behind the rear fin. The same behavior is also captured by a streamline visualization of the gas passing through the shroud gap of blade "HB" at the two different locations "S2" and "S1", shown respectively in Fig. 22a and Fig. 22c. In the pictures, the surface of the blade is colored by non-dimensional static pressure, and the streamlines are colored by relative velocity vector magnitude.

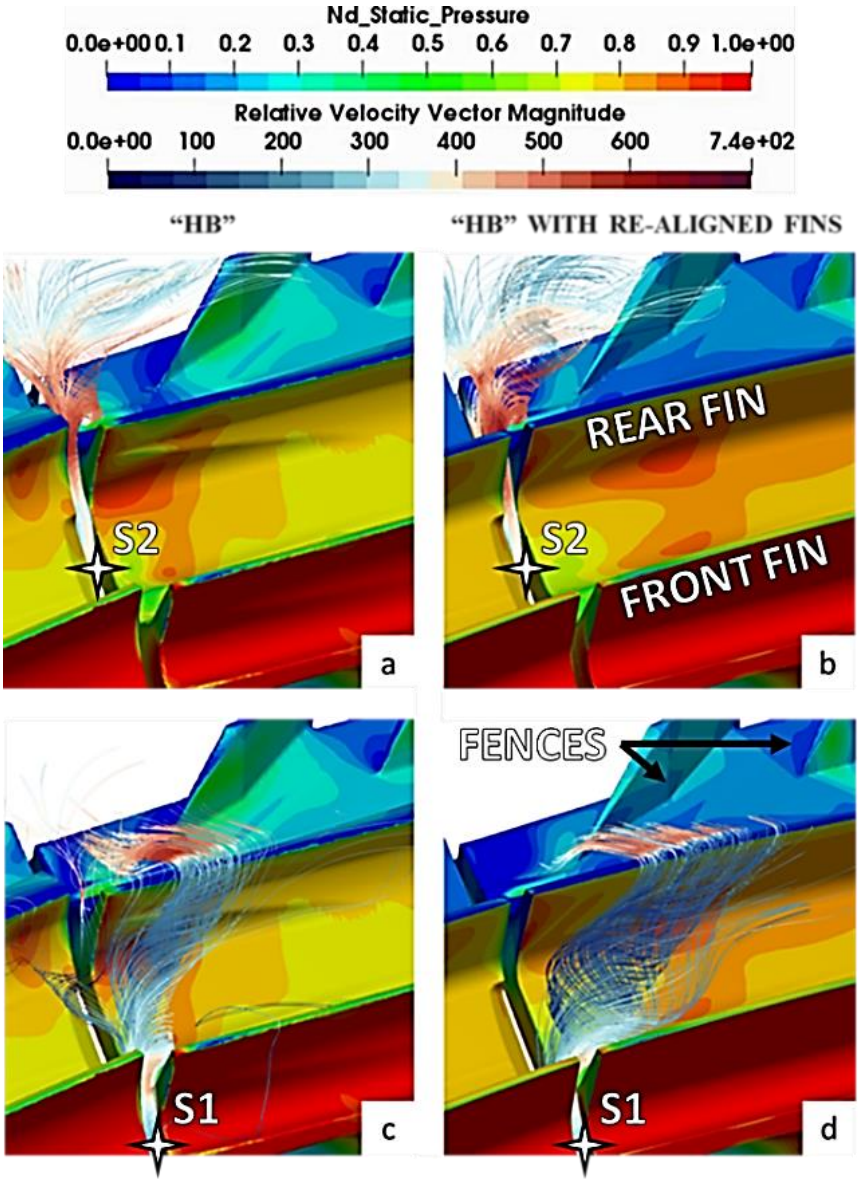

Figure 22: Streamlines of the leakage flow crossing the shroud gap at two different points "S2" (a,b) and "S1" (c,d). The geometry on the left (a,c) is blade "HB", on the right (b,d) the blade "HB" with fins re-aligned to the design intent. The surface of the blades is colored by non-dimensional static pressure, the streamlines are colored by relative velocity vector magnitude.

When the gas from the main passage crosses the gap at "S1" (Fig. 22c), it accesses the pressurized part of the shroud cavity, in between the two fins (the space between T1 and T2). Conversely at "S2" (Fig. 22a) all the passage flow that crosses the gap has immediate access to the lower-pressure region of the cavity, behind the fins. The "S2"

leakage flow can then be seen forming a clockwise-rotating vortex as it leaves the shroud. As it can be seen from Fig. 22a and Fig. 22c, the fins of the two neighboring shrouds of blade "HB" are misaligned. To assess the relevance of fin misalignment in determining the leakage behavior, an additional geometry is created from blade "HB" by re-aligning the fins with the design intent. CFD results (streamline tracking) from this blade can be seen in Fig. 22b and Fig. 22d. It can be seen that the fin re-alignment mostly affects the "S1" leakage (Fig. 22c and Fig. 22d) rather than the "S2" one (Fig. 22a and Fig. 22b). Interestingly, it was found that the fin re-alignment resulted in a stage efficiency recovery of 0.52 which is significantly larger than the amount recovered by completely restoring the blade aerofoil to its design intent (0.32).

3.4.3 Sensitivity to Blade Aerofoil Geometric Deviation

This section is dedicated to a sensitivity study on the effects of rotor aerofoil shape deviation on the HPT stage efficiency whilst keeping the shroud fixed to its datum design intent. The metrics used to quantify each blade's shape deviation from nominal have been defined in section 3.3. To perform this study, a new set of flow simulations was conducted on the same GOM scans used in the previous sections, following a geometrical modification: the shroud of each GOM blade was replaced with the DI shroud.

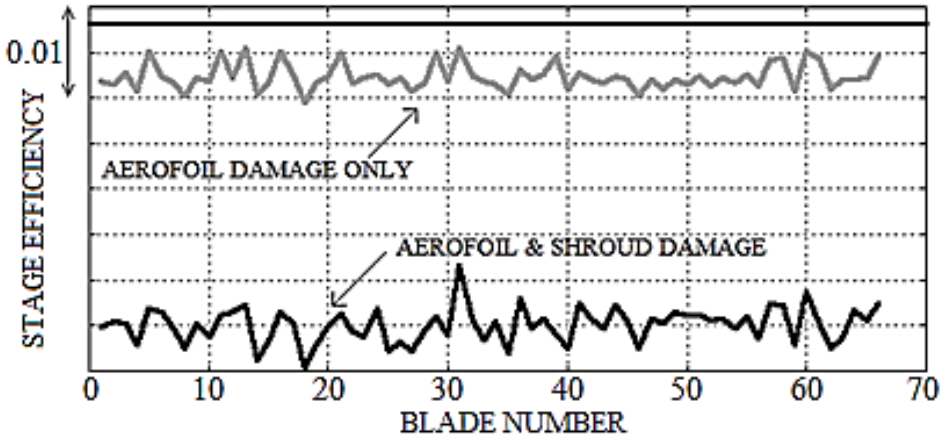

Figure 23: Stage efficiency values: modified GOM scans in grey, original GOM scans in black. The horizontal line is the DI value

This was done to isolate the effect on performance that is exclusively due to the blade's shape deviation, from the much larger one observed for the shroud damage. The latter would otherwise eclipse the former and hinder a conclusive analysis on the

correlation between aerofoil deformation and performance drop. The plot in Fig. 23 shows the stage efficiency values of a subset of the modified GOM scan cases (grey curve), compared with the corresponding original GOM geometries (black curve). The horizontal line in Fig. 23 represents the DI value. The partially repaired GOM scans appear to recover more than 80% of their original performance loss, which is consistent with what was found in the previous section. The performance drop that these partially repaired GOMs are still experiencing is primarily tied to the key parameters of throat area and blade angles. Fig. 24 shows a plot of throat area variation (with respect to nominal) versus stage efficiency loss for the new cases. The plot indicates that there is a significant amount of linear correlation between the two, with R^2 of 0.7991. To study correlation between efficiency and blade angles, the angular deviation values were extracted at 5 span heights (0, 0.25, 0.50, 0.75, 1.0) from the three sets of data plotted in Fig. 11c.

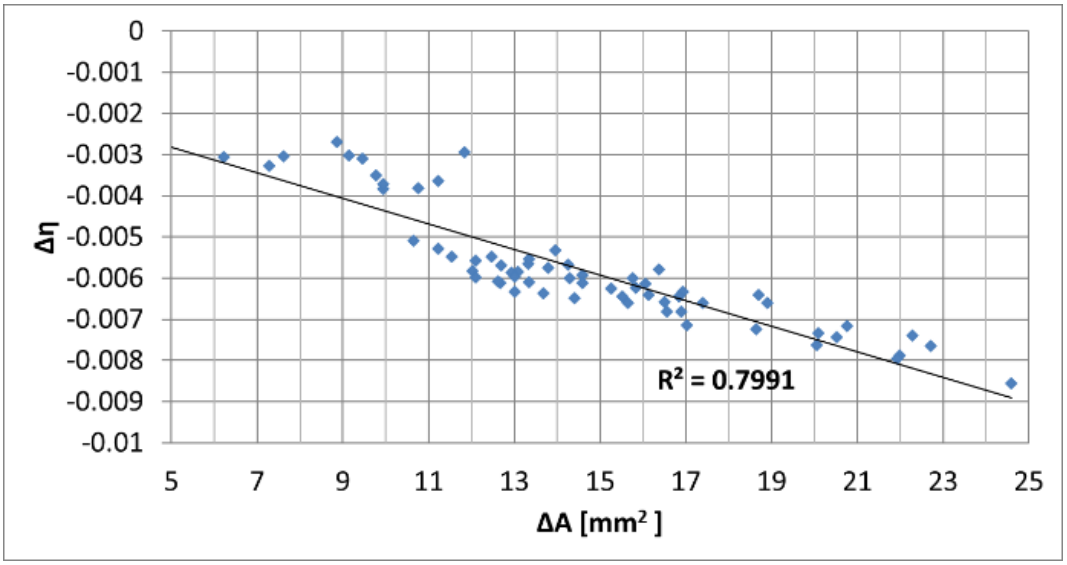

Figure 24: Linear correlation between throat area variation from nominal (ΔA) and stage efficiency loss

These correspond to the same span heights used for the control sections during the EP (inverse mapping) analysis described in section 3. The same random-search algorithm used to determine the fitting coefficients reported in Tab. 4 was used on these extracted sets. Three new combined variables called LEMA, TEMA and STAG were generated respectively for leading edge metal angle, trailing edge metal angle and stagger angle, with 5 coefficients each. These coefficients are reported in Tab. 5.

Table 5: Blade Angles variables definition

Span Section	0.0	0.25	0.50	0.75	1.00	R^2
Coefficient	C_1	C_2	C_3	C_4	C_5	
LEMA	0.0019	0.2781	0.0414	0.0049	0.6737	**0.013**
TEMA	0.2573	0.1582	0.0003	0.0002	0.5840	**0.354**
STAG	0.1100	0.0094	0.0039	0.0660	0.8108	**0.213**

As indicated by the correlation factors in Tab. 5, the leading-edge metal angle has a rather small effect on performance. This is likely due to the relatively large leading-edge diameter, which makes this design more robust to off-design incidences [94]. Stagger angle and trailing edge metal angle appear to have a stronger impact. All three variables consistently have larger coefficients at the highest span point. Therefore, when only aerofoil deformation is present, the key geometric parameters considered achieve the following linear correlation scores against HP stage efficiency loss: (a) Throat Area (R^2 = 79.9%), (b) Trailing Edge Metal Angle (R^2 = 35.4%), (c) Stagger Angle (R^2 = 21.3%), (d) Leading Edge Metal Angle (R^2 = 1.3%).

Blade shape deviation from nominal has been parametrized with the EPs-based aerofoil shape deviation described in section 3.3.2. The variables in Fig. 25 represent XCEN (1-5), DELT (6-10), SKEW (11-15), LEMO (16-20), TEMO (21-25), TECA (26-30) and EXBA (31-35). The five figures associated to each variable represent the corresponding parameter values at the five span sections in the following order: 0, 0.25, 0.5, 0.75, 1. To determine the impact of each one of the EPs on the HP stage efficiency, a sensitivity analysis was conducted. The analysis was carried out by using the "Effective Quadratures" suite [101] to determine the Sobol indices of each EP with respect to stage efficiency, using a Non-Intrusive Polynomial Chaos (NIPC) regression technique [102]. The results of this analysis are reported in Fig. 25a. The most important EP is TEMO (TE re-cambering, 21-25), followed by TECA (TE chord extension, 26-30), LEMO (LE re-cambering, 28-32) and then by SKEW (re-staggering, 11-15). The remaining parameters appear to have little to no effect on stage efficiency. Sensitivity to all EPs also increases towards the tip. This is at least in part due to the wider variation range experienced by these geometric variables at higher spanwise positions. The EPs impact on efficiency was also found to be similar to their impact on the key geometric parameters of throat area and blade angles.

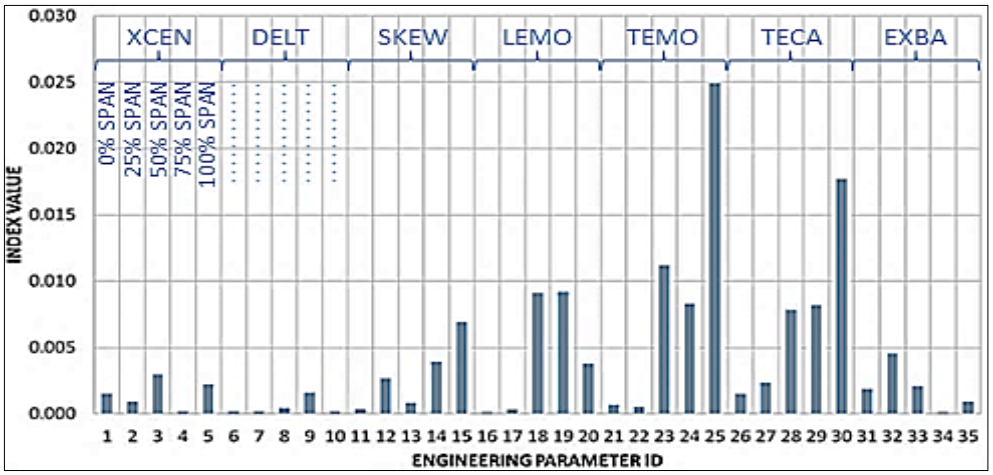

(a)

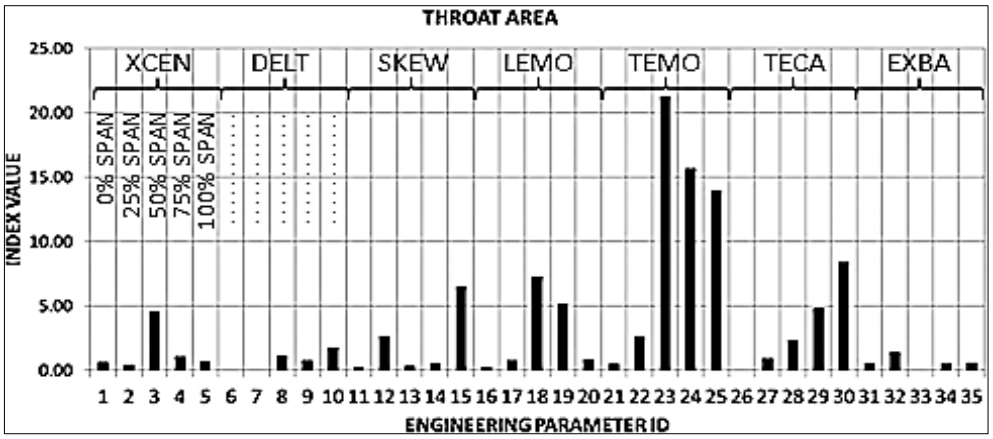

(b)

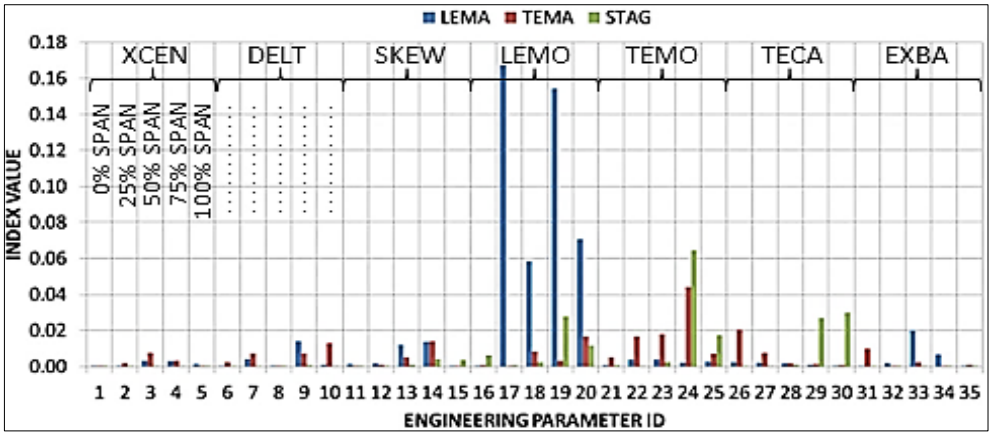

(c)

Figure 25: Sensitivity Analysis: Sobol Indices of the PADRAM Engineering Parameters versus HPT Stage Efficiency (a), throat area (b) and blade angles (c)

To demonstrate this, results from an additional sensitivity study are presented: the graph in Fig. 25b shows the Sobol indices for the EPs impact on throat area, while Fig. 25c shows the same parameters' impact on the three combined variables defined in Tab. 5. For throat area, TEMO at all sections is the most relevant among all, followed by TECA and LEMO, in a similar pattern to the one visible in Fig. 25a. TEMO also appears to have the larger impact on trailing edge metal angle and stagger angle, which in turn have an, albeit weaker, effect on efficiency.

Ultimately, it was decided not to include the 180 thickness parameters in the correlation study, following a series of considerations:

1) The large amounts of performance loss that were observed as a direct consequence of the two primary shape deviation factors (i.e. shroud damage and throat area change) induced the author to concentrate the efforts on performing correlation analysis to these factors. Nevertheless, an additional CFD simulation was carried out to assess the effect of the blade's surface roughness on performance. The geometry used for this test was obtained by modifying one of the blades belonging to the DI shroud and GOM aerofoil series (see grey "AEROFOIL DAMAGE ONLY" curve in Fig. 23). The modification involved replacing the aerofoil of this blade (from the hub to just below the shroud platform) with the aerofoil of the corresponding parametric match generated through the reverse-engineering process described in section 3.3 of the thesis. The resulting blade has a DI shroud and a reverse-engineered GOM aerofoil, which is missing all the surface roughness. Through the subsequent CFD analysis on this zero-roughness case, it was determined that the effect of surface irregularities alone on this blade's performance was of 0.15%. This efficiency delta was considered relatively small with respect to the ones that the analysis revolves around, albeit not completely negligible.

2) The objective of the present part of the study has been to correlate the geometric deviation data with the CFD-calculated performance. To be able to do this, there was the need to limit the total number of geometric parameters, and only the "most important" components of the parametric description were included. Adding the 180 thickness-matching parameters to the 35 engineering parameters would have significantly increased the sample size i.e. the total number of high-fidelity CFD simulations needed to perform the correlation analysis.

An individual blade is selected among the set to perform a breakdown of the effects of different kinds of deterioration on isentropic stage efficiency. Different versions of this blade's geometry are prepared:

- **PURE GOM** = Original GOM scan - Blade n. 6 of Engine n. 5
- **MOD 1** = Modified version of Blade n.6 with Design Intent Aerofoil and GOM shroud
- **MOD 2** = Modified version of MOD 1 with shroud fins re-aligned with Design Intent
- **MOD 3** = Modified version of Blade n.6 with Design Intent Shroud and GOM aerofoil
- **MOD 3 SMOOTH** = Modified version of MOD 3 with smooth aerofoil surface (irregularities removed)

Stage efficiency is calculated for each of the variants listed above, and the results are reported in Fig. 26.

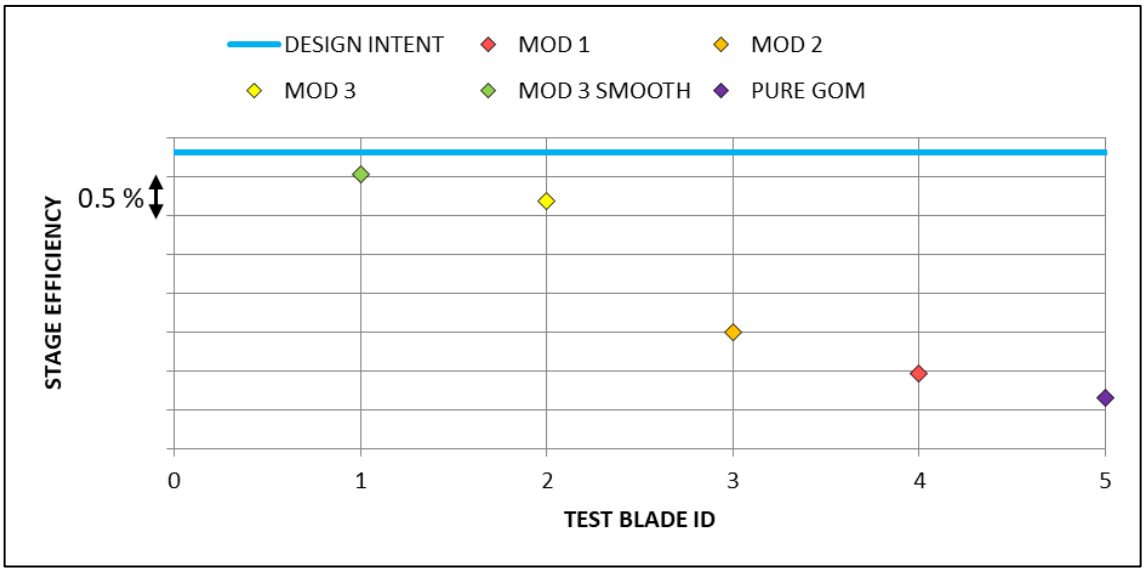

Figure 26: Breakdown of the effect on efficiency of different damage components for Blade n. 6 of Engine n. 5

It can be seen from the graph of Fig. 26 that the largest amount of performance recovery is obtained when repairing the shroud (from "PURE GOM" to "MOD 3") which is in line with the findings of the previous section. By removing all the surface irregularities (from "MOD 3" to "MOD 3 SMOOTH") only a marginal amount of performance is recovered.

3.5 Summary

Undesired shape variations on a high-pressure turbine rotor blade, which can be due to manufacturing variation and in-service deterioration, are observed to have a significant impact on efficiency (>3%) and power generation (>4%) of a modern shrouded HP turbine rotor. This work presents the results of a high-fidelity computational study focused on full 3D, steady-state RANS simulation of the flow around 120 GOM-scanned blade geometries. The GOM blades analyzed display shape deviation from nominal achieved in real operating conditions. Shroud deformation by itself was found to account for approximately 90% of both the stage efficiency and work generation deficits with respect to nominal. Shroud measurements were taken at five critical points in the shroud structure. It was discovered that the performance of the shrouded design under study is highly sensitive to an increase in shroud gap at the mid-chord position. The correlation observed between shroud damage and performance loss is remarkably linear with an R^2 factor exceeding 0.9. When the shroud geometry is restored to nominal on the GOM geometries, more than 80% of the performance drop is recovered. At that point, throat area variation becomes the principal geometric deviation in determining stage efficiency loss, with a linear correlation factor close to 0.8. Among the blade angles, the trailing edge metal angle appears to have the highest linear correlation (0.35) with efficiency drop. Each GOM scan's shape deviation from nominal was expressed through a set of Engineering Parameters (EPs). These parameters describe deformation modes such as trailing edge or leading-edge re-cambering, skewing, and leaning at various span sections. To determine the sensitivity of HPT stage efficiency to each Engineering Parameter, a regression study was conducted. The results reveal that, among the considered EPs, this blade's performance is most sensitive to trailing-edge re-cambering, followed by leading-edge re-cambering and trailing-edge chord extension. One proposed explanation for the above facts is that some degree of blade deformation, particularly TEMO and TECA, that was present as a consequence of manufacturing variation, causes a throat area change. In turn, this reduces the HPT stage efficiency, and forces the blade to operate at higher work and hotter inlet conditions. This can weaken the structure and accelerate further twist and erosion. TEMO is structurally causing a rotation of the shrouds, which directly increases shroud gap, fueling the main aerodynamic loss mechanism. The identification of the geometrical parameters with the largest influence on performance represents the basis for a future robust optimization, aimed at reducing the impact of geometrical deviations on performance, with the additional potential of alleviating the degradation process due to the low-performance driven engine over-throttling.

Chapter 4

Heat Transfer Analysis

4.1 Heat Transfer on In-Serviced Turbine Blades

A prolonged overheating of the HPT rotor blade surface, even by a relatively low value in the order of the tens of Kelvins, can lead to dramatic acceleration of thermal barrier coating (TBC) erosion and melting of the metal alloy. The high-pressure turbine (HPT) rotor is known to experience the most arduous thermal conditions, particularly towards the tip region [80].

Higher-than-nominal temperatures may accelerate the creep process. Overheating for extended periods of time has been shown not only to degrade the structure macroscopically (creep, erosion, melting) but also on a microstructural level [103, 104, 105]. For these reasons, the temperature of the HP components must be managed carefully through the use of sophisticated internal and external cooling mechanisms [106]. The amount of coolant that is injected must be kept to a minimum, to limit mixing losses, and the overall cycle losses due to the compressor bleed . Therefore, the heat transfer systems need to be highly efficient and finely optimized for their purpose [20]. These systems are conceived around the nominal “running” geometries, and a set of operating conditions (usually take-off and cruise), where they operate at peak performance. However, as discussed in the previous sections, there are a number of factors that may lead to deviations from nominal geometry and operating conditions. This part of the work studies the correlation between the geometric deviation from design intent and the distribution of surface heat transfer coefficient, for a large set of in-serviced shrouded HP turbine rotor blades of a modern jet engine resulting from high-resolution 3D structured-light optical scans. Thermal results are obtained through the use of a CFD methodology published by Maffulli and He [107, 108], which allows calculating the heat transfer coefficient (HTC) by fitting a quadratic relation between local wall temperature and heat flux. This technique is described in further detail in the methodology section. This three-point non-linear fitting process requires three CFD

simulations of the flow around the same blade geometry, with prescribed wall temperatures. The objective of this part of the analysis is to determine whether in-service deterioration, by virtue of inducing a modification in the geometry of the blades and the flow conditions, can cause an increase in the heat transfer coefficient in critical areas such as the blade shroud, leading the blades to experience a consequential acceleration of their degradation process.

4.2 Numerical Setup

4.2.1 Geometries

The geometries used in this part of the analysis are represented by a set of HPT rotor blades of the same design of those used in the previous aerodynamic investigation (Chapter 3). As mentioned before, these rotor geometries have a shrouded tip design. Compared to its unshrouded counterpart, the shrouded design (see Fig. 27a) has its main advantage in the higher aerodynamic stage efficiency due to reduced tip leakages. However, this comes at the price of an increased difficulty in the task of cooling the shroud region [78].

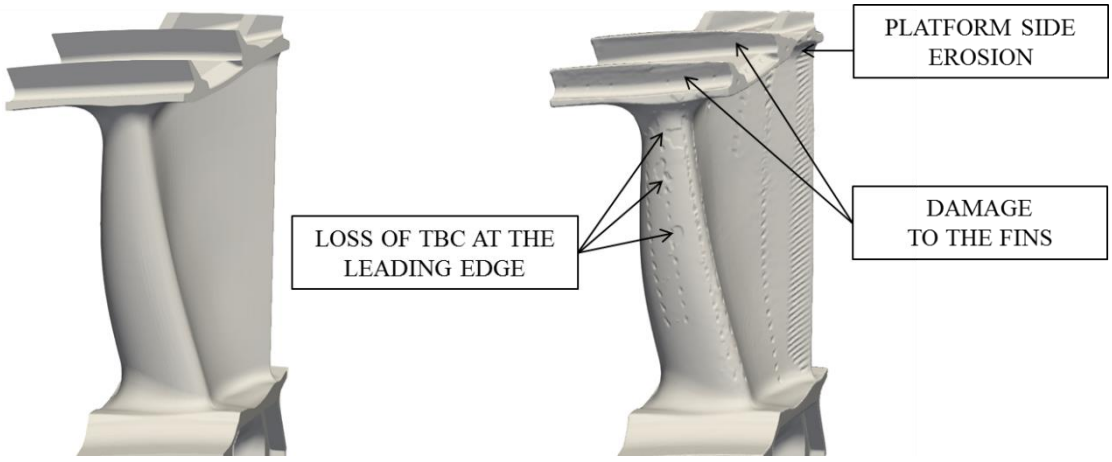

(a) (b)

Figure 27: HP turbine rotor blades, nominal (a) and a blue-light scan displaying different forms of in-service deterioration (b) – Pictures distorted

A set of 66 HPT in-serviced shrouded rotor geometries are analyzed in this part of the work. One of the blades is displayed in Fig. 27b. These blades belong to a single "test" engine that was operated in an experimental rig beyond its normal life timeframe, with the intent of determining the modes and rate of deterioration. The meshing and

simulation techniques used for this part of the work are the same as the ones presented in sections 3.2.2 and 3.2.3.

4.2.2 Heat Transfer Coefficient Calculation Technique

The expression that defines the heat transfer coefficient can be derived from Newton's Law of cooling as given in Eq. 10: the heat flux on the left-hand side is defined as the product of heat transfer coefficient "h" and the difference between wall temperature T_w and recovery temperature (or adiabatic wall temperature) T_{rec}.

$$\dot{q} = h(T_w - T_{rec}) \tag{10}$$

Eq.10 can be used to estimate the heat transfer coefficient on a turbine blade, by conducting two CFD runs. The first one is the simulation of the flow assuming adiabatic wall surfaces, which allows the calculation of the recovery temperature distribution on the blade. The second one is a prescribed-wall-temperature run, where the blade's surface temperature is specified as a boundary condition. This prescribed temperature distribution can be obtained by offsetting the recovery temperature distribution derived from the adiabatic run by a few tens of Kelvins. However, this method is based on the hypothesis that the heat transfer coefficient is independent from the wall temperature, which is often not very realistic [109, 110, 111, 112]. A new three-point non-linear method was published by Maffulli and He [108] to account for the HTC's dependency on the wall temperature by introducing a linear relation between the heat transfer and the temperature difference. This new formulation is reported in Eq. 11 where the locally corrected HTC (with the "j" linear correction terms) value is represented by the first term on the right-hand side.

$$\dot{q} = (h_0 + j_1 T_w)(T_w - T_{rec}) \tag{11}$$

$$\begin{cases} \dot{q_{w1}} = (h_0 + j_1 T_{w1})(T_{w1} - T_{rec}) \\ \dot{q_{w2}} = (h_0 + j_1 T_{w2})(T_{w2} - T_{rec}) \end{cases} \tag{12}$$

To solve Eq. 11 for the HTC, three CFD runs are necessary. The first one is still represented by the adiabatic case for the initial calculation of the recovery temperature, and the remaining two consist in two separate prescribed-wall-temperature runs. The HTC distribution on the blade surfaces is then calculated by solving the system in Eq. 12 where the flow solutions provide the values for the $\dot{q}$ and T terms, allowing calculation of the unknowns (h_0 and j_1). In the present work, the specified wall temperature boundary conditions for the two cases listed in Eq. 12 are created by

offsetting the recovery surface temperature calculated during the adiabatic run, by respectively +50K and -50K. This quantity is chosen as a trade-off between fitting accuracy (ideally requiring the smallest possible offset) and stability of the fitting process, which in turn becomes less robust the more the two prescribed temperature values are close together.

4.3 Uncertainty Quantification

As was the case for the aerodynamic analysis part, the rotor domain of each individual case is constituted by a single circumferential repetition of the same geometry, to allow for single-passage CFD analysis with periodic boundaries. All the blade-to-blade measurements that are described in this section are taken between two identical blades that have an angular shift equal to the periodicity angle. In this section, the uncertainty quantification is focused on the shroud region, as the aerodynamic analysis revealed that this design is particularly impacted by geometric deviation taking place in this part of the geometry.

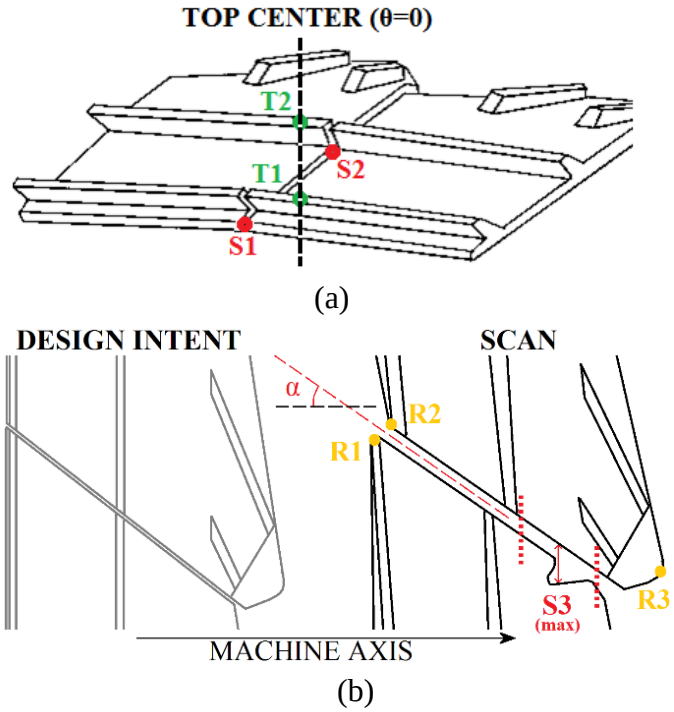

Figure 28: Measurement points of the shroud gaps S1, S2, S3 between neighboring blades, tip clearances T1 and T2, shroud angle α and shroud platform radii R1, R2, R3

The blades display different degrees of in-service deterioration, commonly including elongation, twist, erosion, and local loss of thermal barrier coating. On this set of blades, the most amount of damage can be seen in the shroud region, with an increase of all the clearances (tip gaps and inter-platform gaps).

Measurements taken in the shroud region of each blade are used to quantify the deformation of the shroud region. The measurements include the two tip clearances T_1, T_2 and the three inter-platform shroud gaps S_1, S_2 and S_{3max}, as depicted in Fig. 28. On this set of scans, a V-shaped opening can be observed in the rear half of the platform region. To quantify the extent of this opening on each blade, the inter-platform gap distance is measured throughout all the rear half portion of the shroud (between the dashed lines in Fig. 28b), and the maximum distance value is exported as S_{3max}. Conversely, the S_1 and S_2 shroud gap measurements are taken for all the blades at two fixed axial positions. T_1 and T_2 are measured as the radial distances between the tip of the respective fin and the design intent casing at the top center position.

It can also be seen from the relative orientation of the shroud fins in Fig. 28b that the typical scan displays a twist of the platform with respect to the design intent geometry.

Table 6: Damage Parametrization for HTC analysis

PARAMETER	DESCRIPTION
S_1	Front inter-platform shroud gap
S_2	Middle inter-platform shroud gap
S_{3max}	Rear inter-platform maximum shroud gap
T_1	Front fin tip-to-casing gap
T_2	Rear fin tip-to-casing gap
α	Shroud angle with respect to the machine axis
R_1	Radius of the shroud platform in the front suction side corner
R_2	Radius of the shroud platform in the front pressure side corner
R_3	Radius of the shroud platform above the blade's trailing edge
V	Volume lost due to erosion

This counterclockwise twist is in part responsible for the increase in shroud gap as discussed in the previous chapter. To quantify this, a parameter called "shroud angle" is measured on all the blades as the angle formed by the shroud gap mean line with the

axial direction. To quantify elongation, the blade radius at three points R_1, R_2 and R_3 on the upper face of the shroud platform is measured as shown in Fig. 28b.

Finally, the volume of the rear half of the inter-platform shroud gap is measured directly on the computational grids by calculating the volume of mesh in between the two neighboring shroud platforms. In order to do so, the three points R_1, R_2 and R_3 and the shroud angle on each blade are used as a reference to place a cuboid in the gap region. The cuboid includes the gap space and the side platform metal from two neighboring blades. The volume occupied by the fluid mesh within the cuboid is then calculated with proprietary Rolls-Royce software. This measurement is proportional to the volume of metal that was lost to erosion in the rear shroud gap region (between dashed lines in Fig. 28b). Tab. 6 reports all the parameters used to quantify geometric deviation in the present analysis.

4.4 CFD Results and Sensitivity Analysis

The scanned blades display notable differences from the nominal both in terms of geometry and heat transfer, particularly in the shroud region. Fig. 29 shows a comparison of the heat transfer patterns on the design intent rotor and on a typical in-serviced scan from the present set.

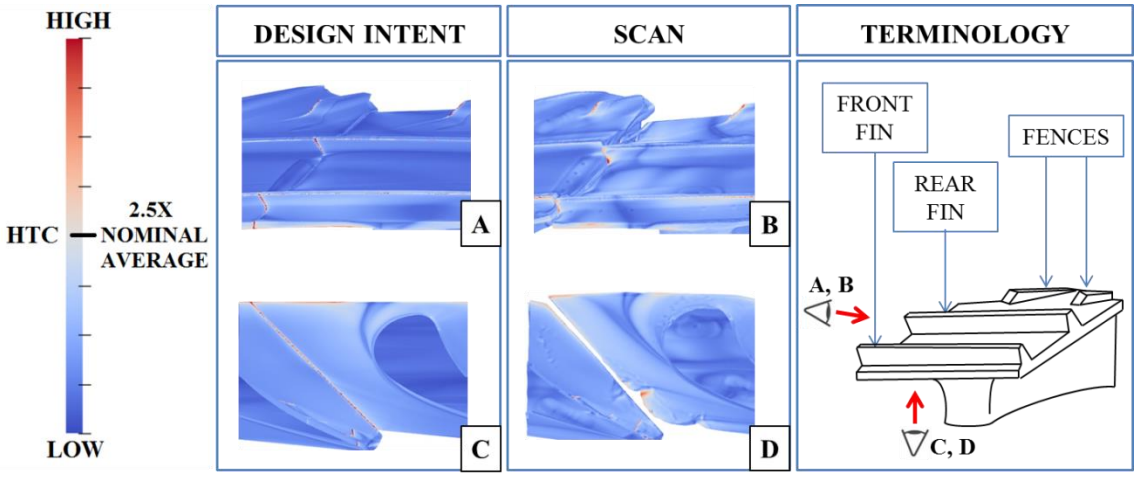

Figure 29: Comparison of the HTC contours on the design intent case (left) against the same contours on one of the scans (right) - displaying the outer (A, B) and inner (C, D) surfaces of the shroud, where the blade has been sectioned off, to attain a full view of the shroud – Pictures distorted

By visual inspection of the HTC results from flow simulations carried out on the scans, it can be seen that higher-than-nominal heat transfer zones have formed due to

the deterioration and modification of the flow conditions. It can be seen in Fig. 29a that the many sharp corners on the design intent geometry are marked as high-HTC areas, which is expected since usually heat transfer is higher in stagnation and sharp-turning points. The same corners appear to have been rounded off by erosion in the in-serviced component. In the baseline design, the inter-platform shroud gap is near zero, and there is no significant amount of flow passing through it. The figures show that there is a notable overall increase in shroud HTC due to damage. It is found that the overall shroud HTC (calculated as the average HTC on the whole shroud region) on the scanned blades is approximately 11% higher than the corresponding nominal value. The damaged geometry shown in Fig. 29b and Fig. 29d also displays a high-HTC patch in the rear part of the shroud gap, where erosion has carved the previously mentioned V-shaped opening in the suction-side platform. This patch is clearly visible when looking at the shroud from below (Figure 4D). The contours of Fig. 30 show the near-wall gas static temperatures for the same blades used in Fig. 29. In the scanned rotor case (Fig. 30b, Fig. 30d) the gas that comes in contact with the upper face of the shroud platform is 25K to 50K hotter with respect to the nominal case.

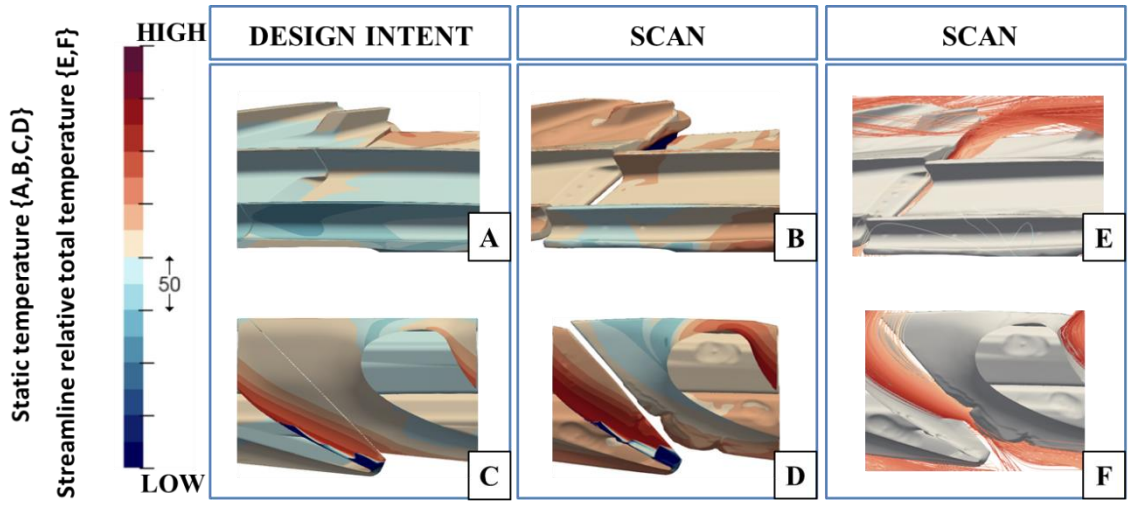

Figure 30: Comparison in terms of near-wall gas static temperatures on the design intent (A, C) and the same scan shown in Figure 5 (B, D) – Trajectories of the flow particles crossing the shroud gap in the rear portion of the platform are also shown (E, F) – Pictures distorted

By looking at the contours on the lower face (Fig. 30a, Fig. 30c), it can be seen that a stream of high-temperature gas from the main passage is reaching and crossing the aft portion of the inter-platform shroud gap, where most of the erosion is taking place. This is confirmed by the streamline visualization of Fig. 30e and Fig. 30f, showing the trajectories of the stream particles passing through the rear shroud gap opening. This

particular region of the shroud sees a combination of high HTC and high near-wall gas temperatures, which can accelerate the erosion process.

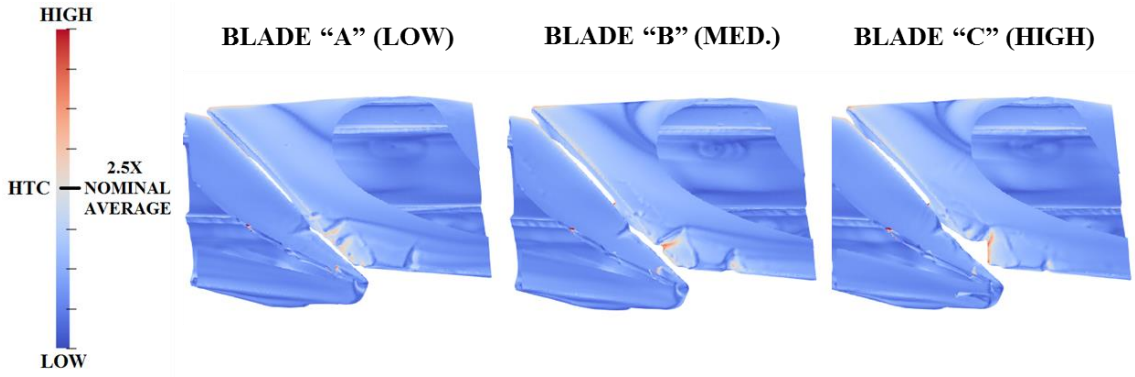

Figure 31: Views of the shroud platform from below in three cases of low (A), medium (B) and high (C) HTC. The surface is coloured by HTC value – Pictures distorted

The progressive erosion and formation of the opening can be seen from the views of the bottom face of the shroud displayed in Fig. 31, where HTC contours are shown for three in-serviced blades named "A", "B" and "C", respectively representing the low, medium, and high HTC levels of the set. HTC levels get increasingly worse with damage, as the amount of hot passage flow that is able to cross the opening in the gap gets larger. This, for the current set of blades and flow conditions, points to a degenerative process.

A linear correlation analysis is conducted to determine the effect of the parameters listed in Tab. 6 on shroud heat transfer. The metric used to quantify the level of HTC on the shroud platforms of the in-serviced blades is the fraction of surface area with an HTC value exceeding 2.5 times the average value on the nominal shroud. A linear correlation between this metric and the parameters in Tab. 6 is sought through multiple runs of a random-search algorithm. A linear combination variable is formulated with the set of coefficients achieving the best R^2 score.

The resulting best-fit linear combination called "SDV_{HTC}" (Shroud Damage Variable for HTC correlation) achieves a good correlation (R^2 = 0.795) and is reported in Eq. 13a, where the terms that ended up having a near-zero (< 0.01) coefficient (S_2, T_1, α and R3) are removed.

$$SDV_{HTC} = 0.16S_1 + 0.33S_{3max} + 0.11T_2 + 0.16R_1 + 0.04R_2 + 0.2V \qquad (13a)$$

The results shown in Fig. 32a indicate that there is significant linear correlation between the combination variable SDV_{HTC} and the shroud surface area with high HTC.

The values of the coefficients also indicate which parameters are more associated with the formation of high-HTC regions on the shroud surface. The maximum shroud gap amplitude in the rear half of the platform (S_{3max}) and the volume loss (V) are the most important parameters with coefficients respectively equal to 0.33 and 0.2. This is in agreement with what can be seen from the contours of Fig. 31, where the highest HTC levels are associated with large amounts of erosion in the rear portion of the inter-platform shroud gap, both in terms of depth of the V-shaped opening and metal volume loss.

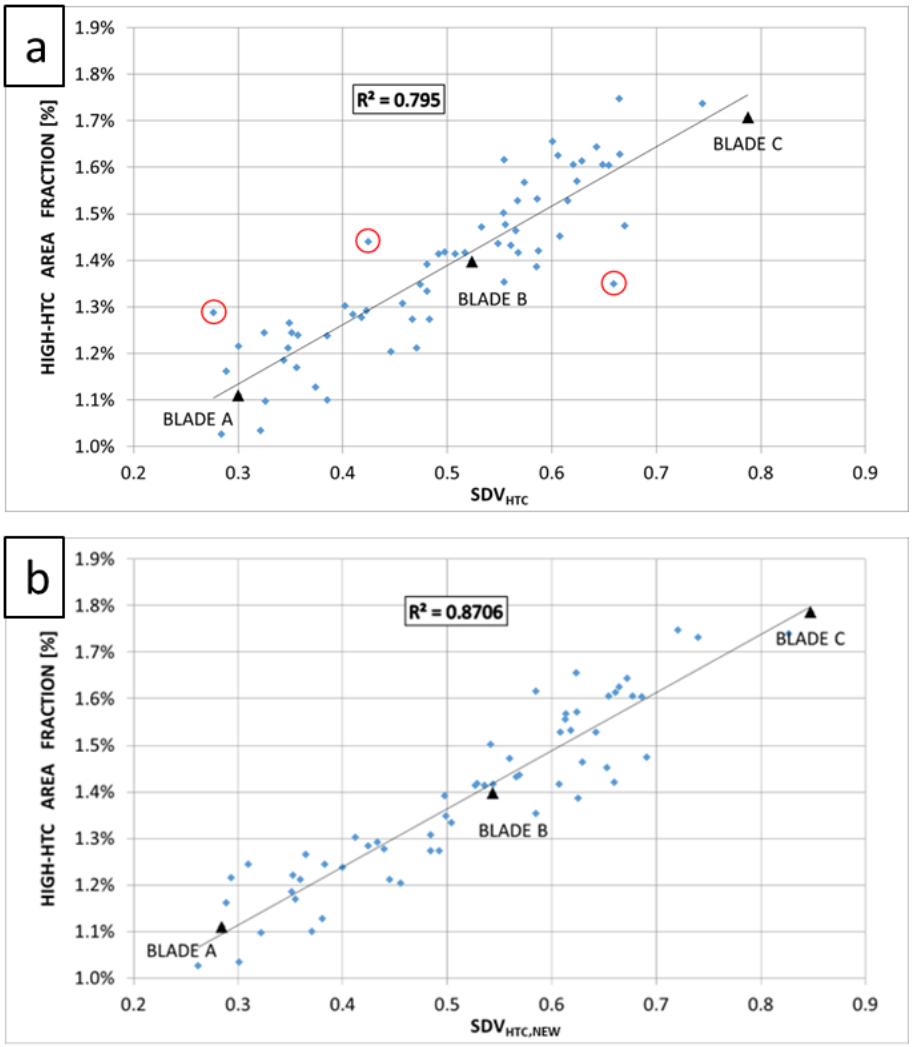

Figure 32: a) Distribution of the SDV combination variable against the fraction of high-HTC shroud surface area of the scanned rotors. Three outlier points have been located and are circled in red – b) New distribution of the SDV combination variable after removal of three outlier points. The trend-line and linearity score are also displayed in the charts. The three blades A, B and C used in Figure 31 are highlighted.

Three "outlier" points were located, by discriminating based on the distance of each point from the trendline (if the distance is greater than 1.5 standard deviations, the point is considered an outlier). The outliers are highlighted in Fig. 32a. After eliminating the three points from the distribution and re-running the regression algorithm, a new combination variable with a different set of coefficients is obtained, achieving a linearity index (R^2) of 0.871 as indicated by the graph displayed in Fig. 32b. The new Shroud Damage Variable for HTC ($SDV_{HTC,NEW}$) is reported in Eq. 13b.

$$SDV_{HTC,NEW} = 0.2 \cdot S_1 + 0.39 \cdot S_{3max} + 0.04 \cdot T_2 + 0.13 \cdot R_1 + 0.24 \cdot V \qquad (13b)$$

It can be seen by comparing the two Equations 13a and 13b that, by removing the three outliers, the weight of the main coefficients (S_1, S_{3max} and V) increases even further, while the rest of the coefficients lose magnitude. R_2 is missing from Eq. 13b because the relative coefficient goes to zero in the new variable.

The scanned geometries used in the present analysis also suffer from different degrees of aerodynamic performance loss. Isentropic stage efficiency (see Eq. 8) for the present set of blades is now correlated against shroud damage, employing the same parametrization used for the HTC analysis. Likewise, a linear combination variable is constructed by combination of the damage parameters with a set of best-fit coefficients as reported in Eq. 14. This variable is called "$SDV_{ETA,II}$" to distinguish it from the one used in Chapter 3 of the thesis.

$$\begin{aligned} SDV_{ETA,II} = {} & 0.04S_1 + 0.27S_2 + 0.03S_{3max} + 0.03T_1 + 0.2T_2 + 0.01\alpha \\ & + \quad 0.08R_1 + 0.06R_2 + 0.24R_3 + 0.04V \end{aligned} \qquad (14)$$

Figure 33 represents the distribution of isentropic stage efficiency for the scanned geometries as a function of the $SDV_{ETA,II}$ variable. Similarly to what was observed with the HTC correlation study, there is significant correlation between the variable $SDV_{ETA,II}$ and the isentropic stage efficiency loss with respect to nominal, with a linearity score of 0.754. In this case, however, it can be seen that the most relevant parameter to aerodynamic performance is the mid-chord shroud gap "S2". This finding is in line with that was observed in the aerodynamic analysis of Chapter 3 of the thesis: a large pressure differential can be found at that particular position between the passage and top cavity flows. This creates a large amount of leakage through the inter-platform shroud gap, which is severely detrimental to aerodynamic performance.

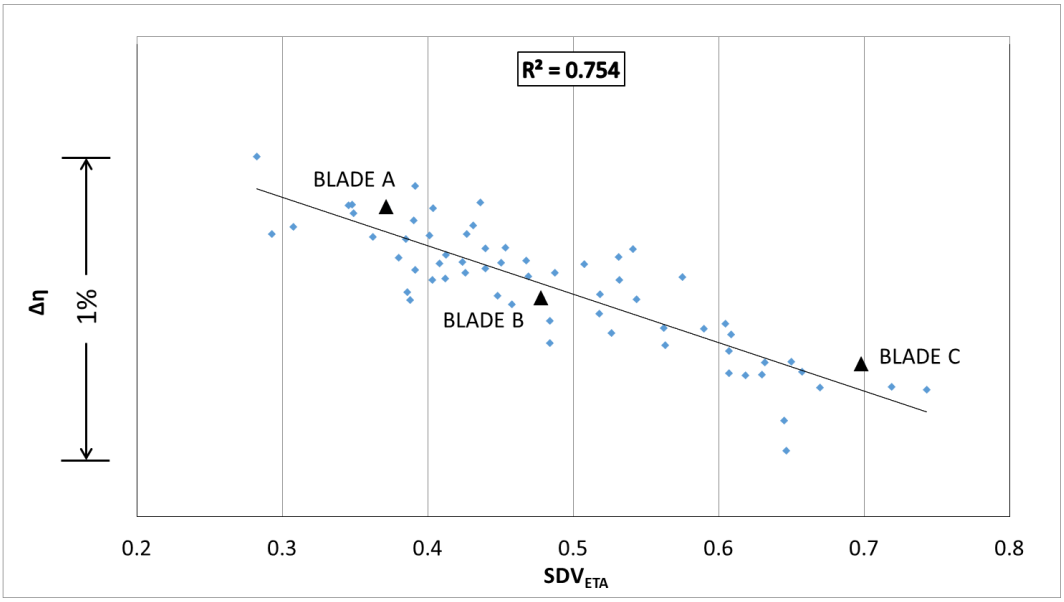

Figure 33: Distribution of the $SDV_{ETA,II}$ combination variable against the isentropic stage efficiency values of the scanned rotors. The trend-line and linearity score are also displayed in the chart. The three blades A, B and C of Figure 31are highlighted

The trailing edge elongation R_3 and rear fin tip gap are also associated to a relatively high impact on efficiency for this set of blades. In contrast with what was observed for heat transfer, it appears that the depth of the V-shaped opening (S_{3max} parameter) has a low impact when looking at aerodynamic performance. In Fig. 33, the points pertaining to the three blades "A" "B" and "C" shown in Fig. 31 are also highlighted. It is interesting to note that both the SDV combination variables shown in Fig.32 and Fig. 33 rank these blades in the same order in terms of parametric damage vs. performance, indicating that low aerodynamic performance is also associated with high heat transfer.

4.5 Summary

A series of CFD simulations were conducted on a set of blue-light optical scans of in-serviced HP turbine rotor geometries from a modern jet engine, with the objective of identifying the damage modes that are associated with an increased heat transfer in the shroud region. All the blades belonging to this set display overall higher (+11%) HTC values on the shroud when compared to the average value measured on the nominal shroud region. All the sharp corners originally present in the nominal design appear to have been rounded off in the in-serviced blades, as a result of erosion. Furthermore, significant HTC increases are observed locally, particularly in the shroud gap region.

Shroud damage levels on the present set of blades have been measured in terms of a set of parameters including shroud gaps, tip gaps, elongation, and volumetric loss. A correlation analysis was then conducted to assess the impact of each parameter on HTC levels, intended as the fraction of shroud surface area with an HTC greater than 2.5 times the average value on the nominal shroud surface. A linear correlation between this measure and the set of parameters was sought, obtaining a R^2 score of 0.871, with the largest coefficients being those pertaining to the amplitude of the shroud gap in the rear platform part, and the metal volume loss due to erosion in the same region.

In terms of aerodynamic performance, a notable isentropic stage efficiency loss was observed with a 1% variability within the set. A linear correlation study was conducted between efficiency and the set of parameters achieving an R^2 score of 0.754, with the highest-ranking coefficient being the S_2 inter-platform shroud gap at mid-chord. This finding on the set of blades considered here is in agreement with the results presented in Chapter 3.

It is interesting to note that the thermal and aerodynamic aspects are markedly sensitive to damage in different areas of the shroud: mid-chord gap for the aerodynamic performance and maximum rear platform gap for the thermal exchange performance. It is hypothesized that, due to an initial twist of the shroud platforms due to blade turning, the blades experience an increase in inter-platform shroud gap. Consequent to this, a stream of hot passage gas is able to cross the shroud gap reaching the top cavity. Over time, the leakage flow through the rear portion of the shroud gap carves a V-shaped opening in the suction side of the shroud platform, exposing a larger surface of internal alloy to the erosion process. Analysis of the CFD results reveals that an increase in the size of the opening causes higher local HTC values, which further increases heat exchange and can lead to a degenerative acceleration of the erosion process.

Since the trigger of this aero-thermal deterioration mechanism was identified to be the initial blade twist below the shroud platform, it is recommended to periodically monitor this parameter during service. This could be done with less-invasive techniques (e.g., borescope analysis [113]). The temperature distribution provided by the combustor also plays a major role in this phenomenon. By shifting the distribution peak towards the inner radii, the temperature of the flow streams that end up crossing the shroud gap, may be lowered. This is the subject of further optimization studies.

Chapter 5

Fully Featured Aerothermal Analysis

5.1 Multi-Fidelity approach to CFD on Turbine Blades

High-Fidelity CFD techniques are becoming increasingly relevant as a tool used by turbomachinery analysts and designers to predict surface temperatures. In this field, the reality of the cases being modeled is indeed characterized by remarkably complex physics and sophisticated geometrical features. The aero-thermal interaction between the blades and the flow is also quite complex and includes unsteady effects, the formation of small-scale flow structures, significant differences in the flow evolution timescales between the mainstream gas and the internal coolant. All these aspects point to the fact that a multi-disciplinary, high-fidelity approach is needed to properly capture this reality in a mathematical model. Naturally, upgrading the model's fidelity comes with additional computational costs. Increasing the fidelity of the geometry is clearly associated with a higher grid cell count. The same can be said for the inclusion of the solid domain in the model, which is needed for being able to model the fluid-solid thermal interaction. This is done by running a CHT simulation. In literature, examples of CHT analyses focused on internally cooled gas turbine applications can be found in the work of Rigby et al. [114], York et al. [115], Facchini et al [116] and Ho et al [117], on stator vanes, focusing on the role played by turbulence and transition modelling. CHT-based analyses focused on internally cooled rotors can be found in Tsukamoto et al. [118], where the importance of modelling the internal turbulators is highlighted, and Ho et al. [119]. A CHT investigation was carried out by Takahashi et al. [120] where the authors compared the temperatures predicted by the numerical model with the erosion patterns present on ex-service blades. Modelling the unsteadiness of the flow behavior is perhaps the most expensive improvement to the model's fidelity, which sometimes pushes the computational cost beyond reasonable values. However, a step towards this goal can also be taken by using less expensive frequency-domain approaches such as the phase-lag technique. This method was first developed by Erdos

and Alzner [121], and He [122], and has been used by many authors to model the effects of periodic unsteadiness in turbomachinery applications [123, 124, 125, 126]. These approaches can still provide a better level of fidelity, with respect to the basic mixing-plane steady state RANS, when trying to model a single-stage rotor-stator interaction.

The aim of this part of the work is to analyze the aero-thermal behavior of an HPT stage of a modern jet engine, by providing the results from a set of flow simulation which tackle the modelling problem with different fidelity levels.

- The bottom fidelity level is represented by a 3D steady-state RANS simulation of the flow around a simplified version of the blade geometry. In this case, the internal cavities are not modeled, and the film cooling flow is injected from the external surfaces through film cooling "strip" models.
- On the same geometry, a phase-lag simulation has also been carried, using the steady-state one as the initial solution.
- The same two kinds of CFD simulations (steady-state and phase-lag) have also been run for the fully-featured geometry cases, where the high-pressure rotor geometry definition includes the internal cavity and cooling holes.
- Steady-state coupled CHT simulations are run on the fully-featured geometry, to assess the impact of fluid-solid heat exchange on the rotor surface temperatures.
- A modified HPS inlet temperature distribution is conceived around the benefit of having lower maximum near-wall gas temperatures on critical regions of the rotor surface. The new distribution is tested on the fully featured model with both adiabatic-walls and CHT simulations, and the results are compared to evaluate the amount of benefit predicted by the two models.

5.2 Numerical Setup

5.2.1 Geometries and Boundary Conditions

In this part of the work, only the nominal (DI) geometries are considered. The cases where the rotor geometry does not include the internal cooling cavity system (similarly to what was done in the previous chapters) will be referred to as the "external" cases. Conversely when the internal cooling chambers and tubes of the rotor blade are included in the model, the case is going to be referred to as a "fully featured" one.

An increase in the geometric fidelity of the models prepared for this section of the work is also brought by the adoption of a more realistic HPT stator geometry: the so-called “RIDN” and “RODN” cooling-hole rows, which are present in the real geometry of the component, are included. These are placed respectively at the inner and outer stator endwalls, upstream of the stator vanes. These holes serve the function of inhibiting thermal exchange between the main gas and the stator endwalls by providing a protective layer (film) of cooler air bled from the last high-pressure compressor stage. In the CFD analyses of chapters 3 and 4, the presence of these holes was modelled, just like for the blade film cooling, by positioning source terms in the form of “strip” models. These are indicated with dashed red lines in Fig. 34 (HPS and HPR) and Fig. 35 (HPS only). This kind of modelling is still being used here for the stator vane. Since one of the objectives of this part of the work is to study the migration of the radial temperature distribution, the inclusion of the RIDN and RODN cooling holes allows to have a more realistic prediction of the temperature field downstream of the HPT stator.

In the steady-state models, the single rows communicate through mixing-plane surfaces. In the phase-lag cases, a sliding-plane interface is used between the high-pressure stator and rotor domains. This allows for circumferential variations in the flow conditions to be communicated through the first two rows. In this study, a mixing-plane interface is kept between the rotor and the intermediate-pressure stator, as the focus of the phase-lag analysis is to study the migration of the temperature distribution through the high-pressure stage only.

As mentioned in the introduction, in terms of geometry, two types of cases are run for this analysis: the first type is where the rotor geometry is tight, and only presents the external surfaces, and the second type is where the rotor geometry is fully featured, the blade is hollow and presents the internal cavity, tubes and cooling holes. The first type of cases will be referred to as the “external” ones (see Fig. 34), and the second type as the “fully featured” ones (Fig. 35).

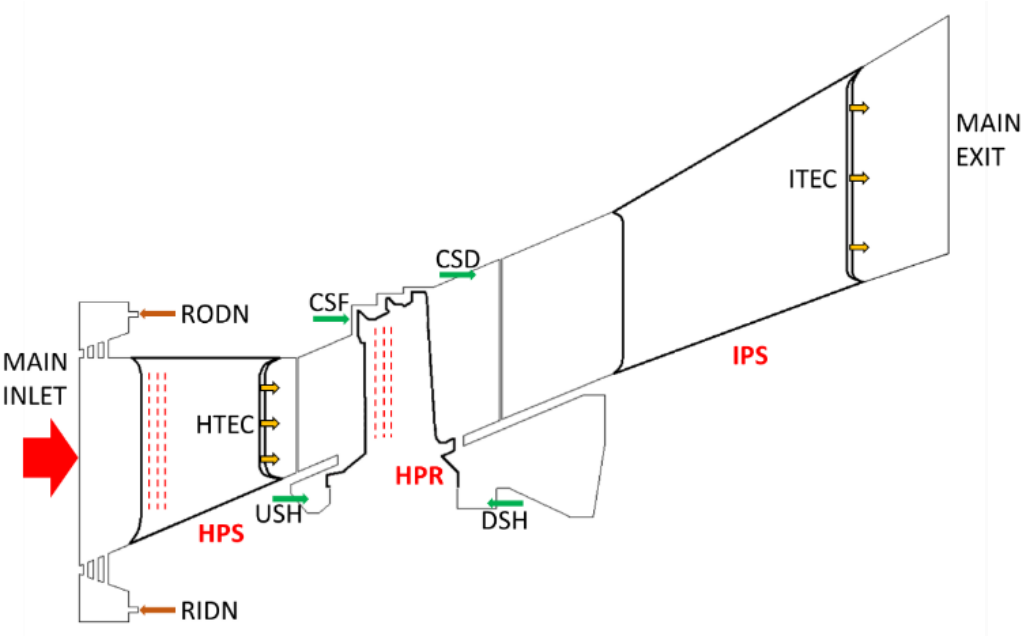

Figure 34: Schematic of the computational domain used for the "external" flow simulations. The arrows represent inflow boundaries. Film cooling source models are represented by the dashed red lines. The meaning of the acronyms can be found in nomenclature – Picture distorted and not to scale

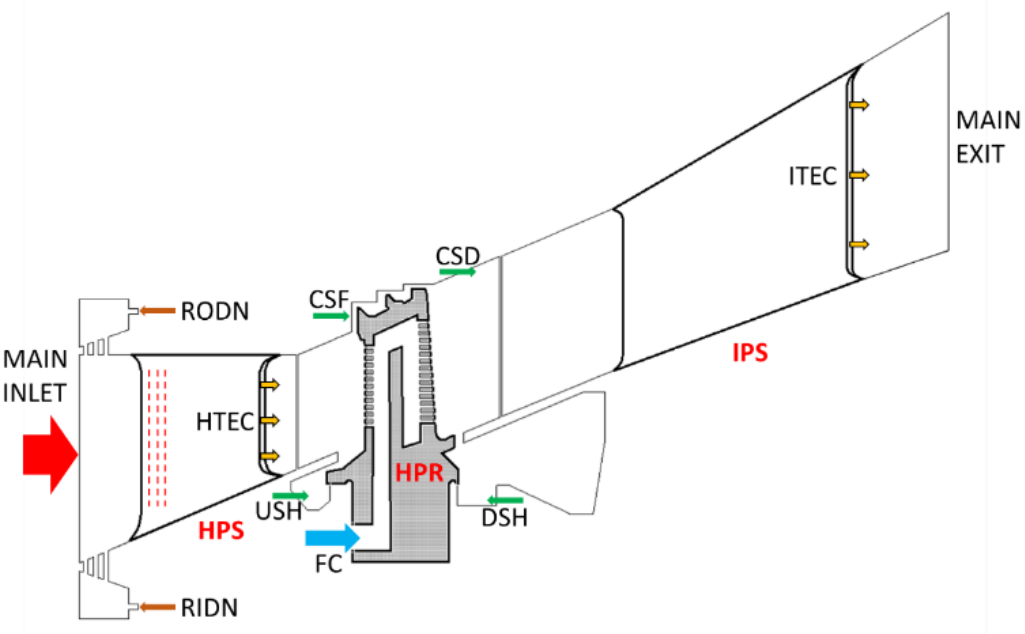

Figure 35: Schematic of the computational domain used for the "fully featured" flow simulations. The arrows represent inflow boundaries. Film cooling source models are represented by the dashed red lines. The meaning of the acronyms can be found in nomenclature – Picture distorted and not to scale

The HPT stator geometry is fitted with “RIDN” and “RODN” cooling-hole rows. These are placed respectively at the inner and outer stator endwalls, upstream of the vanes. These holes serve the function of inhibiting thermal exchange between the main gas and the stator endwalls by providing a protective layer (film) of cooler air bled from the last high-pressure compressor stage. Film cooling on the stator and rotor blades is modelled through the use of source terms in the form of “strip” models.

CHT simulations are only run on the fully featured domain. As symbolized by the grey area in Fig. 35, the metal that constitutes the HPT rotor structure is included in the fully-featured model with its own mesh. This “solid” mesh (as opposed to the “fluid” one, pertaining to the fluid domain) is only active in the CHT simulations, where heat exchange is taking place between the fluid and solid meshes. The solid mesh is inactive when conducting standard (adiabatic-walls) CFD runs. The HPS inlet BC, indicated as “MAIN INLET” in both Figs. 34 and 35, is a 2D field where total pressure, total temperature and inlet flow angle values are specified. The same class of BC is used in the fully featured cases for the rotor film cooling inlet, indicated as “FC” in Fig. 35. The IPS exit BC (“MAIN EXIT” in Figs. 34 and 35) is a radial 1D static pressure profile. The operating conditions being simulated in this analysis is meant to replicate real operating conditions. The amount and temperature of the coolant emitted by each strip model was instead calculated based on previous data provided by the company for different operating conditions. The values were calculated by running a quasi-3D simulation. The resulting mass flows, and injection temperatures were then linearly scaled based on the new pressure and temperature ratios, in order to match the present operating point.

Simulations are run by enforcing periodic boundaries at the domains’ periodic sides. For the high-pressure stator, the domain contains two complete blades, which allows the inclusion of all the periodic variability produced by the combustor in the main inlet BC as shown in Fig. 50a. The rotor and intermediate-pressure stator domains only include a single blade passage between the periodic boundaries.

5.2.2 Meshing for External Simulation

This section describes the grid generation technique used to mesh for the external CFD cases. The computational meshes for the high-pressure domains (HPS, HPR) are generated with BOXER, which allows to mesh directly on the CAD surfaces. The grid-generation technique used by BOXER is capable of capturing the small-scale geometric features of the components, by creating a high-resolution body-fitted mesh. The meshes generated with this technique are hexa-dominant, with 22 prismatic layers on all the

walls. First cell height is set to 5×10^{-7} m, which ensured a y^+ value below 1 on all the surfaces. The bounding box resolution is set to 70 cells for the HPS and 40 cells for the HPR. These base cell sizes are adopted following the results of the mesh independence study presented in section 3.2.2 of this thesis.

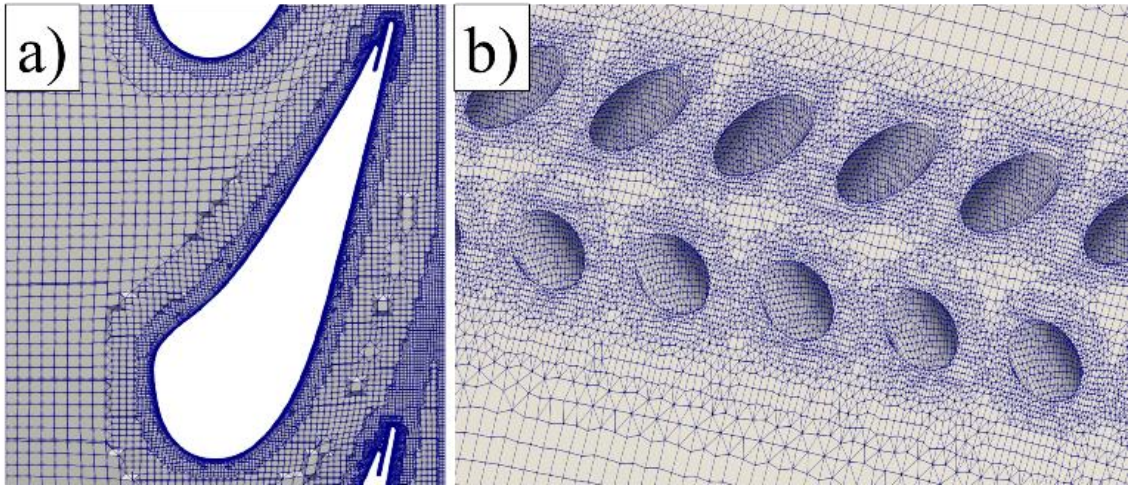

Figure 36: HPS mesh, constant-radius section view at mid-span (a) and view of the inner endwall surface mesh with RIDN cooling holes (b) – Pictures distorted

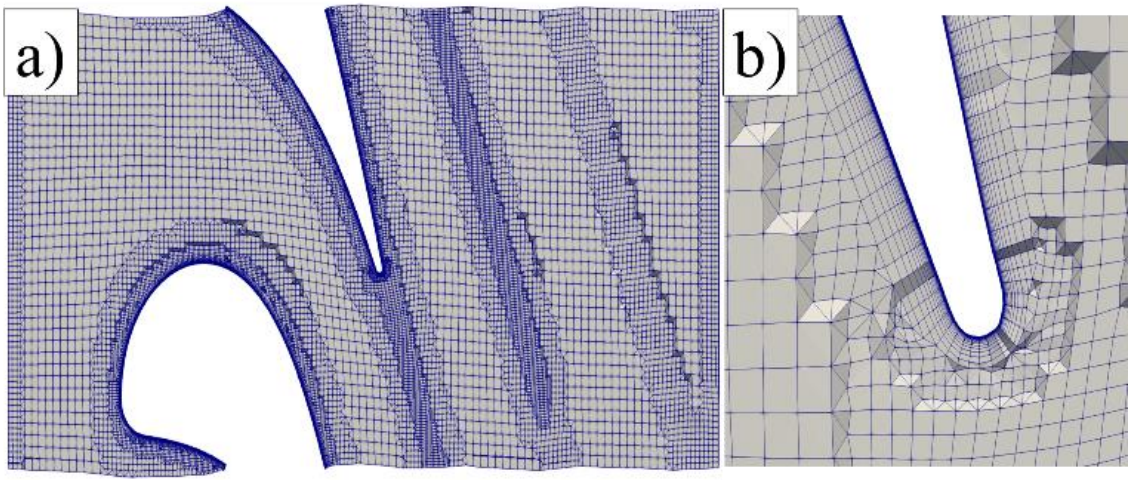

Figure 37: HPR mesh, constant-radius section view at mid-span (a) and closeup view of the trailing edge – Pictures distorted

Different refinement levels are imposed on critical surfaces such as the RIDN and RODN tubes in process. Fig. 36a shows a constant-radius section view of the HPS mesh. The surface mesh at the inner endwall with the RIDN cooling holes is visible in Fig. 36b. Fig. 37a shows a mid-span radial section of the HPR mesh, with a close-up on the trailing edge (Fig. 37b) displaying the prismatic layers. The section views of Fig.

36a and Figs. 37a and 37b clearly show the presence of local grid refinement. The HPS and HPR BOXER meshes have a cell count of respectively 25M and 35M and are generated in batch mode by using a “lua” script.

The intermediate-pressure stator is meshed with a default PADRAM meshing template file. PADRAM is a proprietary Rolls-Royce software tool for rapid high-quality meshing with a multi-block H-O-H structured approach. The O-mesh around the IPS blade has 14 layers and the same first cell height used in the high-pressure stage meshes is adopted. This is the same IPS mesh that was used in the previous analyses of sections 3 and 4 of this work.

the HPS domain, the rotor trailing edge and shroud, to ensure proper grid resolution. The mesh volume is refined in the rotor tip clearance and shroud platform gap regions. Both the rotor and stator wake dissipation regions are firstly located via precursor CFD runs and then selectively refined for the final meshing

5.2.3 Meshing for Fully Featured Simulation

The fully featured 1 ½ stage domain shares the same stator meshes (HPS, IPS) with the external one. The rotor geometry is now fully featured and a new meshing run for the HPR domain is carried out in BOXER. The fully featured rotor domain includes fluid and solid sub-domains, which are meshed simultaneously. As mentioned previously, the solid mesh is only to be used for the CHT simulations, but it is meshed together with the fluid one. This allows to create a conformal interface between the two, which facilitates the conjugate coupling.

BOXER’s meshing technique is octree-based. To define the closed volume where the mesh needs to be generated, the octree mesher relies on the specification of a “bounding box”. Once again, the bounding box is a cylindrical sector with a circumferential opening of ϑ_p (single-passage periodicity angle) and limited to an inner and outer radius. BOXER makes use of “seed points” to distinguish between confined regions within the box where the octree is set to propagate.

An individual octree mesh is created in the confined region that contains any seed point. In this case, two seeds are used as shown in the scheme of Fig. 38. The red region represents the space where the fluid mesh is to be created, while the black one pertains to the solid. The resulting solid mesh is conformal with the fluid one at the contact interface, which is represented by the red borders in Fig. 38. As indicated in this figure, the fluid mesh is seeded in the main gas path zone, and the octree is able to penetrate inside the cooling hole tubes and fill the inner cavity of the blade.

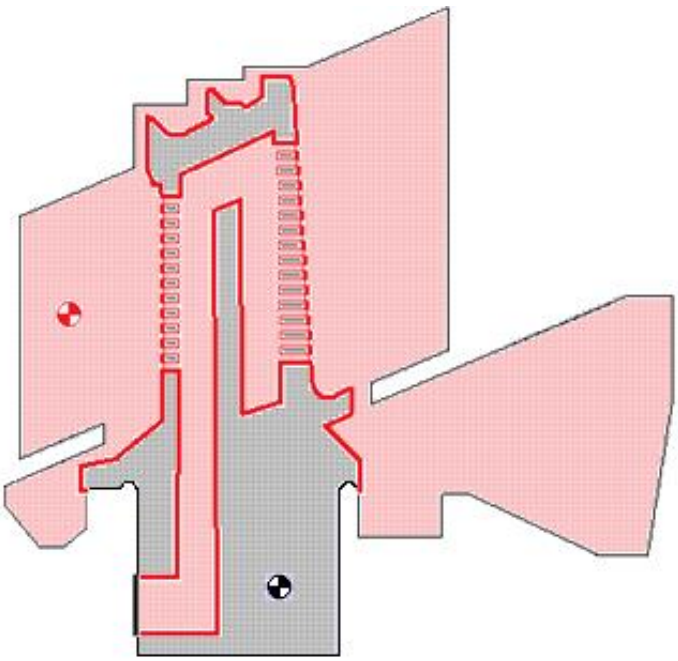

Figure 38: Section-view scheme showing the multi-region meshing technique used to generate the fluid and solid grids of the fully-featured rotor domain

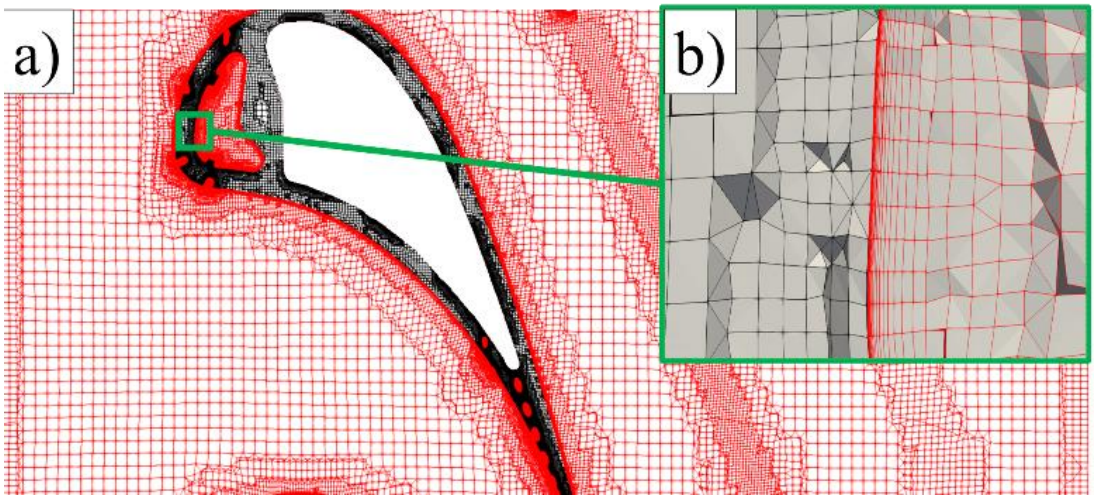

Figure 39: Radial section view showing the fully featured rotor mesh (a); the central part of the section including additional internal chambers is omitted from the representation for industrial confidentiality reasons – and a close up on the conformal interface (b) – Picture distorted

The fluid mesh octree propagation stops at the root of the blade where a patch is positioned to close off the cooling duct. This patch is also used as the inlet BC for the film cooling flow (FC in Fig. 35). Similarly to the external case, the mesh presents 22 prismatic layers on all the surfaces, and a first cell height of 5×10^{-7} m is adopted.

Various grid refinement specifications are used, repeating the same strategy described in the previous section, including the circumferential resolutions of the HPR bounding box (40 cells). Fig. 39a shows a radial section view of the HPR fluid (red) and solid (black) meshes, where some internal details have been omitted for confidentiality. A closeup on the conformal interface is shown in Fig. 39b.

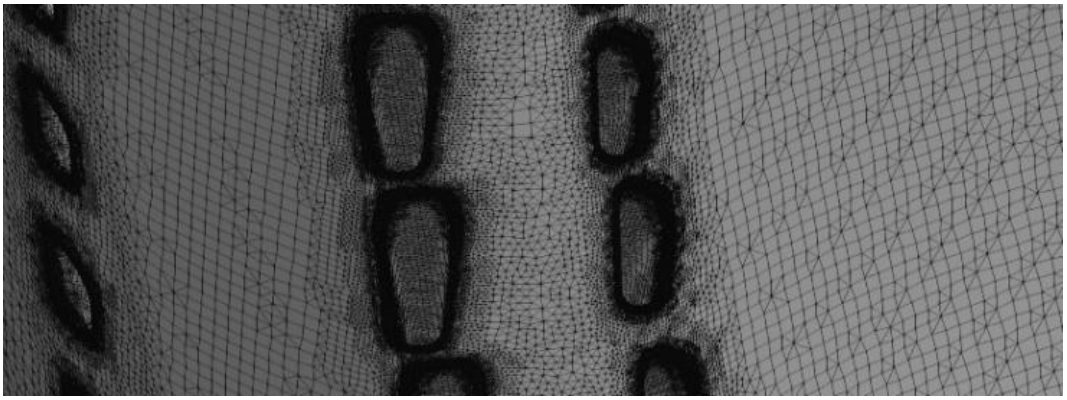

Figure 40: Fully featured rotor, solid surface mesh showing rows of cooling holes. High levels of local grid refinement are visible – Picture distorted

Additional refinement is imposed on the internals of the blade, as the surface of the inner cavity is fitted with several ribs to increase the heat exchange rates. The tubes and cooling hole borders present the highest level of refinement as it can be seen from the surface mesh representation of Fig. 40. The length of a mesh cell edge in those regions is respectively 1/32 and 1/64 times the reference one. This is done to obtain a good resolution of the mesh inside the tubes, and a good quality of the prismatic layers at the corners where the tubes meet the blade's external surface (the highly refined regions visible in Fig. 40). The same refinement is used for the opposite end of the cooling tubes, towards the blade's inner cavity. The final fluid and solid meshes have respectively 190M and 60M elements.

5.2.4 Simulation Technique

The software tool used to conduct the CFD simulations is the proprietary Rolls-Royce solver HYDRA. The 3D Reynolds-Averaged Navier-Stokes (RANS) equations are solved by using a single-grid implicit method. The k-ω turbulence model is adopted. The CFL number used is 20 for both the steady-state and phase-lag simulations. For the steady-state case, convergence is considered achieved when the root-mean-square (RMS) value of the momentum equations' residuals reaches the

value of 10^{-11}, which takes place after about 2,500 iterations. A drop of four orders of magnitude from the initial value is achieved.

The phase-lag simulation is run for a total of 10 periods, each one representing a complete revolution of the HPR row. Results are post-processed only for the last cycle. The number of harmonics and time-steps per cycle considered for the phase-lag simulations are based on the according periodicity of the HPS and HPR domains. A number of 6 harmonics is adopted for proper resolution in the frequency-domain, and calculations are performed for 363 time-steps per cycle. Ten sub-iterations of the implicit scheme are carried out for each time step. To assess the convergence of the phase-lag simulation, a force monitor is placed on the rotor. Through this monitor, the solver integrates the force on the blade and calculates the harmonic force components. During each cycle, the solver computes an error term expressed as the difference between each harmonic force component and the corresponding one at the same phase in the previous period. From one cycle to the next, this error becomes gradually smaller as shown in Fig. 41. The phase-lag calculation is considered converged once the rotor force error goes below the value of 2%.

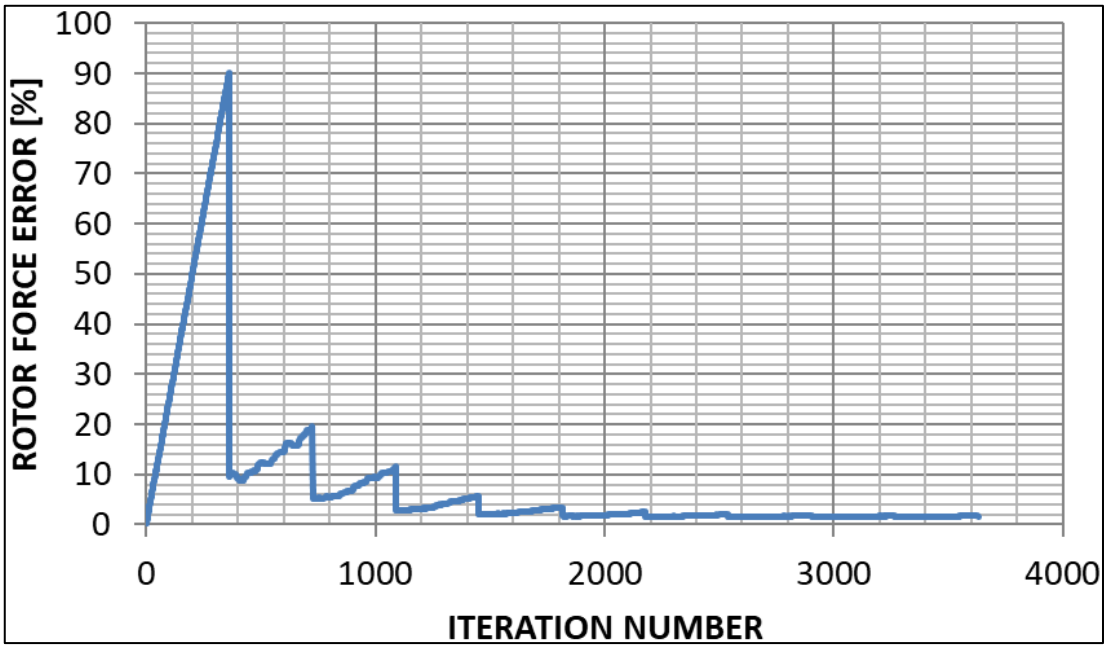

Figure 41: Convergence of the phase-lag simulation

The same settings described above are used both for the external and fully featured cases. During the CHT simulation, the heat conduction equation is solved inside the solid domain with a multi-grid explicit scheme. A HYDRA plugin tool is used to couple the fluid and solid meshes at the interface. Heat data exchange between the

coupled cells is carried out every 10 iterations on both sides. A converged fully featured adiabatic-walls solution is used to initialize the fluid side of the CHT simulation, while the temperature field in the solid domain is initialized with a uniform value. To evaluate the convergence of the temperatures in the solid, the surface temperature is extracted every 500 iterations and compared with the previous distribution. Convergence of the CHT simulation is achieved after about 8,000 iterations.

5.3 Results

5.3.1 External CFD Analysis

This section is dedicated to presenting and discussing the results from the external CFD simulations. The different surfaces of the blade are labelled in Figs. 42a and 42b to help with the identification of the various geometrical features. The arrangement of the film cooling source terms used in the external models is shown in Fig. 42c. Fig. 43 shows a comparison of the results respectively from the steady-state and phase-lag RANS simulations on the external geometry. For the phase-lag results, the cycle-average flow is considered. The static temperature distributions on the rotor are shown in Figs. 43a, 43c from the front and Figs. 43b, 43d from the rear.

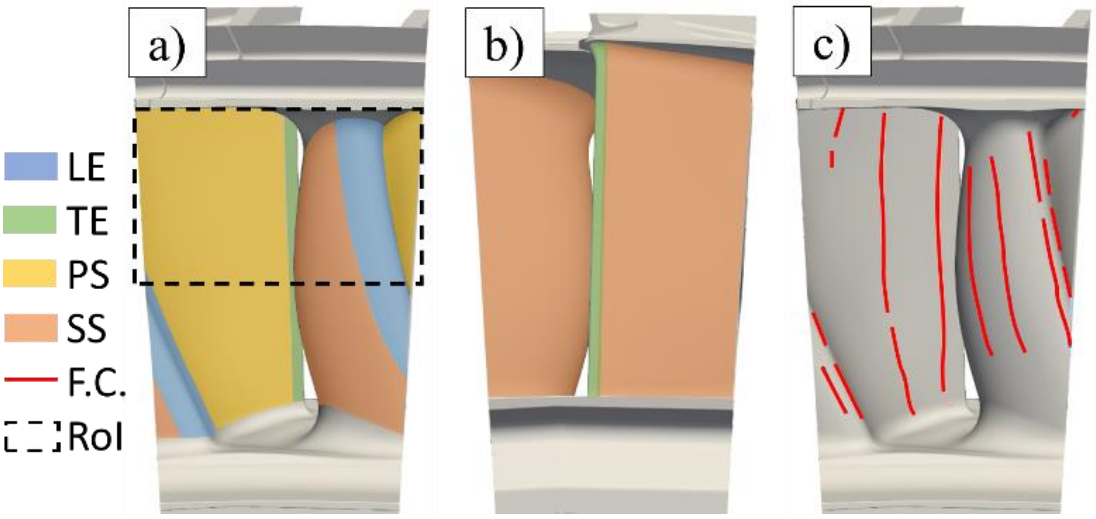

Figure 42: Identification of the surface features on the rotor blade viewed from the front (a) and rear (b), and a map of the film cooling source terms used in the model (c); The region of interest (RoI) in the LE-PS zone is enclosed in the dashed box in (a) – Pictures distorted

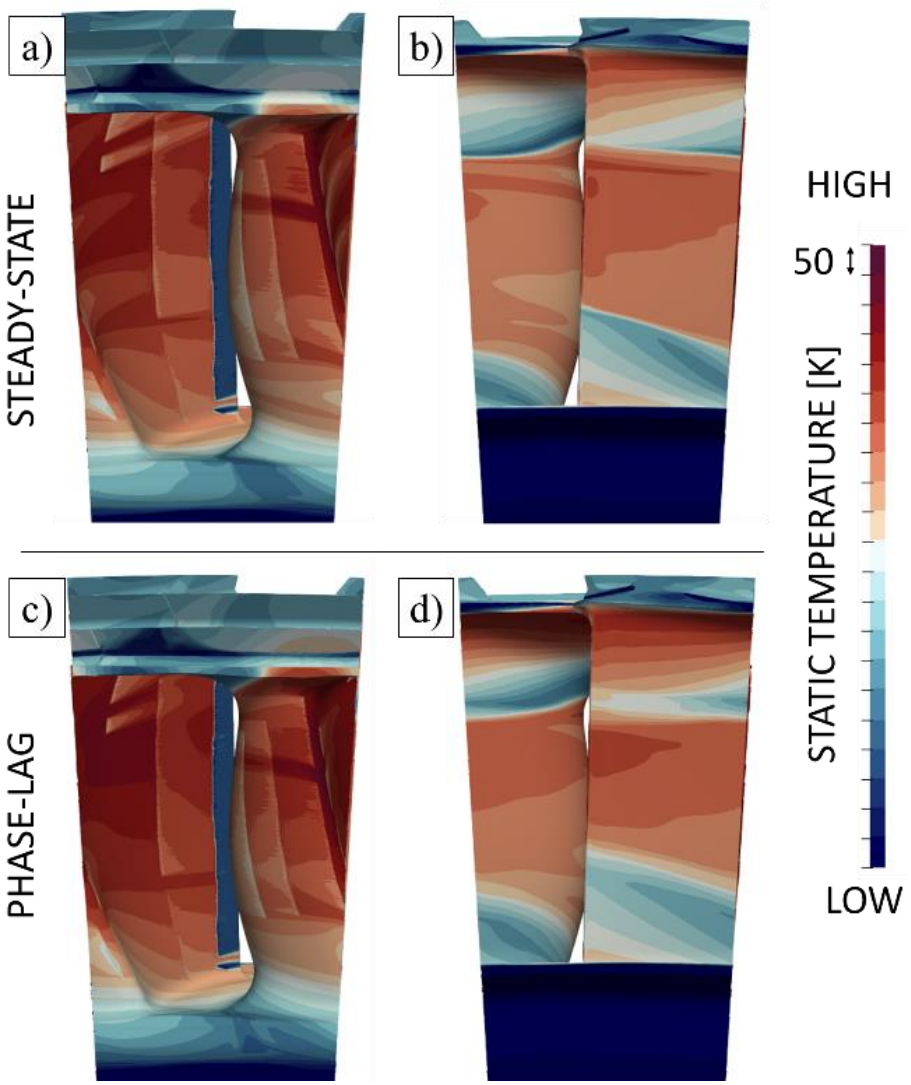

Figure 43: Static temperature contours predicted on the rotor by steady-state RANS viewed from the front (a) and rear (b); by phase-lag RANS viewed from the front (c) and rear (d) – Pictures distorted

Figs. 44a and 44b display contours of the static temperature delta respectively from the front and rear between the phase-lag and steady-state results. The presence of the film cooling source terms on the leading edge and pressure side is revealed in Figs. 10a and 10c as the vertical discontinuities in the contours on the blade surface. The trailing-edge cooling source strip is also clearly visible, delivering a large amount of coolant. In general, as indicated by both delta plots of Fig. 44, the phase-lag prediction points to higher overall temperatures with respect to the steady-state one, with the exception of the hub region, and a higher maximum temperature.

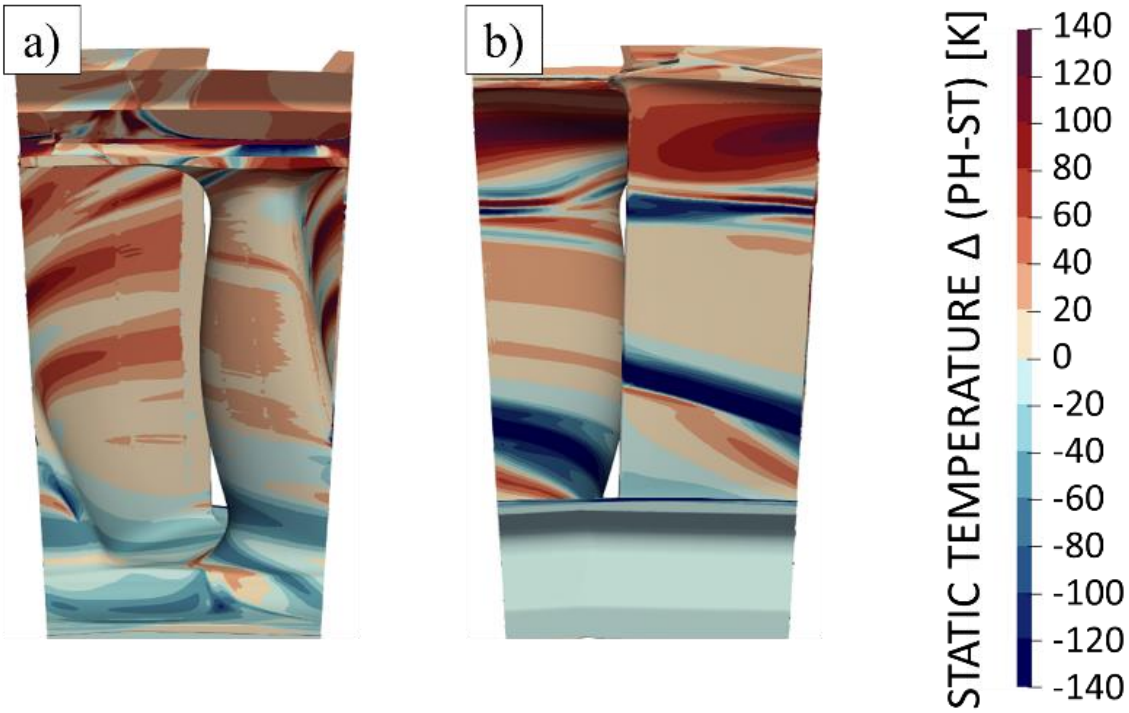

Figure 44: Static temperature difference between the phase-lag (PH) and steady-state (ST) simulations viewed from the front (a) and rear (b) – Pictures distorted

On average, the phase-lag prediction is around 20K hotter in the LE region, between 40K and 60K hotter in the shroud region, and up to 140K hotter near the PS. The region of interest for this comparison is indicated as "RoI" and is located inside the dashed black box in Fig. 42a. This is where the maximum temperatures are reached, and an accurate prediction of the film cooling behavior becomes critically important. By comparing this region in the two front views of Fig. 43a and 43c, it can be seen that each one of the PS-LE film cooling strips (the last three strips on the right of Fig. 42c) is generating a well-defined cold wake in the steady-state case (43a).

These features are missing in the phase-lag results, where a single region with higher temperatures is predicted. This same tendency can be also spotted on the suction side of the blade (Fig. 43b and Fig. 43d). The two cold surface currents predicted by the steady-state simulation, respectively above the hub and below the shroud, are much more pronounced and narrower than their phase-lag counterparts. The same behavior can be deduced by looking at the delta plot of Fig. 44b. This is due to the high levels of periodic unsteadiness that characterize the near-wall flow in the pressure side region right downstream of the leading edge. In the steady-state case, the cooling flows emitted by these strips constantly impinge over the same distinct surface regions. Conversely, the same cooling flows can be seen periodically oscillating up and down in the various phase-lag instantaneous flow solutions. This is shown in Fig. 45, where the

surface temperature contours inside the region of interest previously included in the dashed black box in Fig. 42a are shown. This behavior is reflected in the cycle-average solution with a more diffused, and ultimately less effective surface cooling.

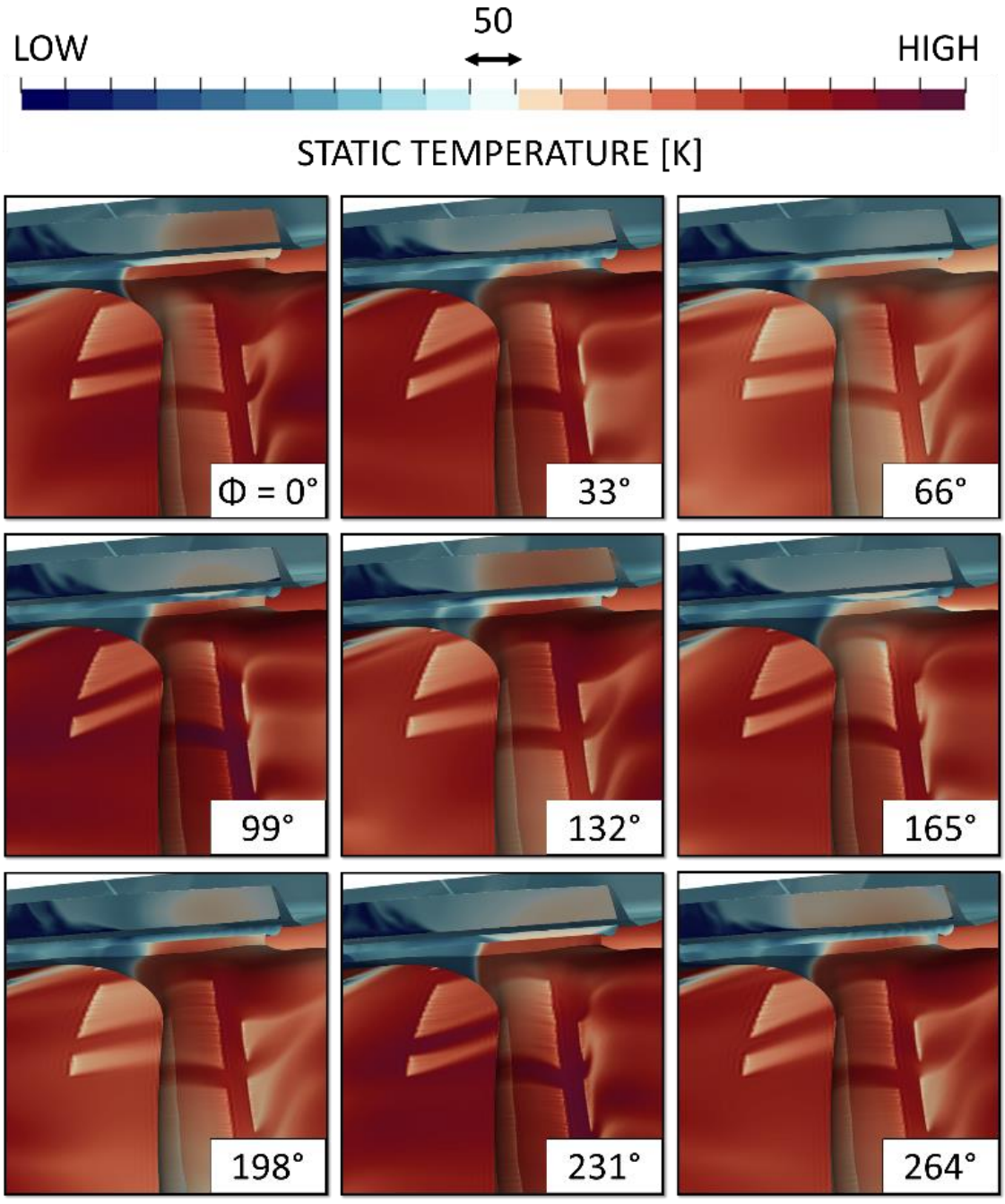

Figure 45: Phase-lag simulation – Instantaneous static temperature contours inside the region of interest circled in Fig. 42a at different period phases Φ – Pictures distorted

5.3.2 Fully Featured CFD Analysis

This section is dedicated to presenting the results of the fully featured cases, and to compare these with the ones obtained with the external models. First, a comparison is made focusing on the breakdown of the film cooling flow between different rows of cooling holes. To perform the comparison, the rows are divided in the following sets: leading edge (LE), front pressure side (FPS), rear pressure side (RPS) and trailing edge (TE) as indicated in Fig. 46a. As mentioned previously, in the case of an external model, each film cooling strip model emits a certain mass flow based on a linear scaling of pre-existing data obtained for a different operating condition. Conversely, in the fully featured case, the internal cooling flow is able to redistribute freely between rows, based on the local (external) pressure values and the losses inside the channels.

It is interesting to see in Fig. 46b that the scaled mass flows used in the external model (solid columns) appear to be roughly in line with the ones predicted by the fully featured model (hatched columns), although with some discrepancies, particularly notable in the case of the trailing edge row. It appears that the coolant mass flows from each individual row do not exactly scale linearly with the main global quantities. Further investigation on the linearity of the behavior of the single film cooling rows was conducted by parametrically modifying the FC inlet pressure.

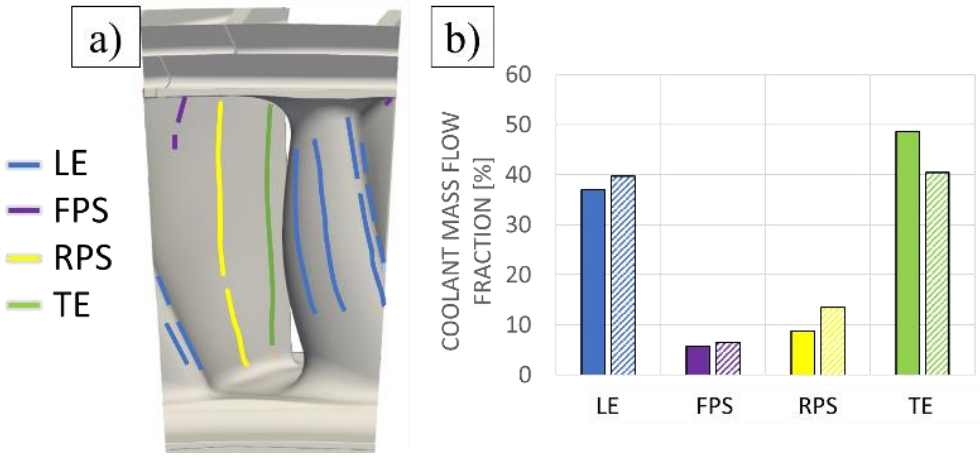

Figure 46: Identification of the different sets of film cooling hole rows (a) and corresponding coolant mass flow fraction predictions (b) by scaling from previous data (solid) and through fully featured CFD on present conditions (hatched)

The results of this study are reported in Fig. 47, showing a remarkably linear behavior up until a 10% inlet pressure reduction is reached. When that value is crossed, the highest amount of non-linearity is exhibited by the LE row. To the author's knowledge, this is the first time such information is made available and can inform

designers on the consequences of a partial failure or obstruction of the coolant feeding system. In particular, the regions of the rotor that would be affected the most in this case are those who rely on the LE rows for film cooling, thus LE-PS and the whole SS.

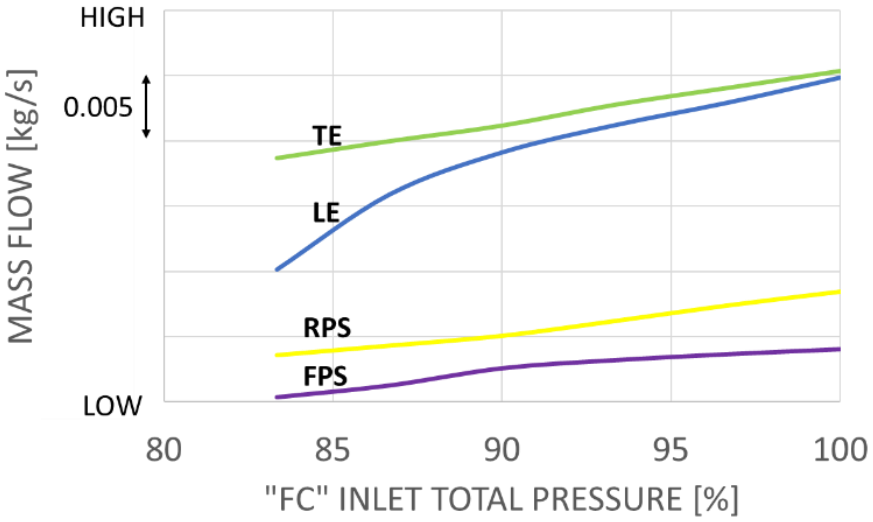

Figure 47: Fully featured modelling - effect of a reduction in FC inlet total pressure on the mass flows of the individual cooling hole rows with the same color scheme of Figure 46

To compare the results in terms of rotor near wall gas temperature distributions, data is extracted from each of the following models reported in Tab. 7.

Table 7: Multi-Fidelity Results Comparison, I

ID	MODEL TYPE	SIMULATION TECHNIQUE
A	External	Steady-state
B	External	Phase-lag
C	Fully featured	Steady-state
D	Fully featured	Phase-lag

The comparison is made by cutting the domain at the three radial sections, respectively at 25%, 50% and 75% span. To facilitate visualization of the results, each section is plotted using a curvilinear coordinate going from TE to LE along the pressure side, and then back to TE along the suction side. The plots of Fig. 48 represent the near wall gas temperature delta of each of the three models B, C, D with respect to model A, following the nomenclature used in Tab. 7.

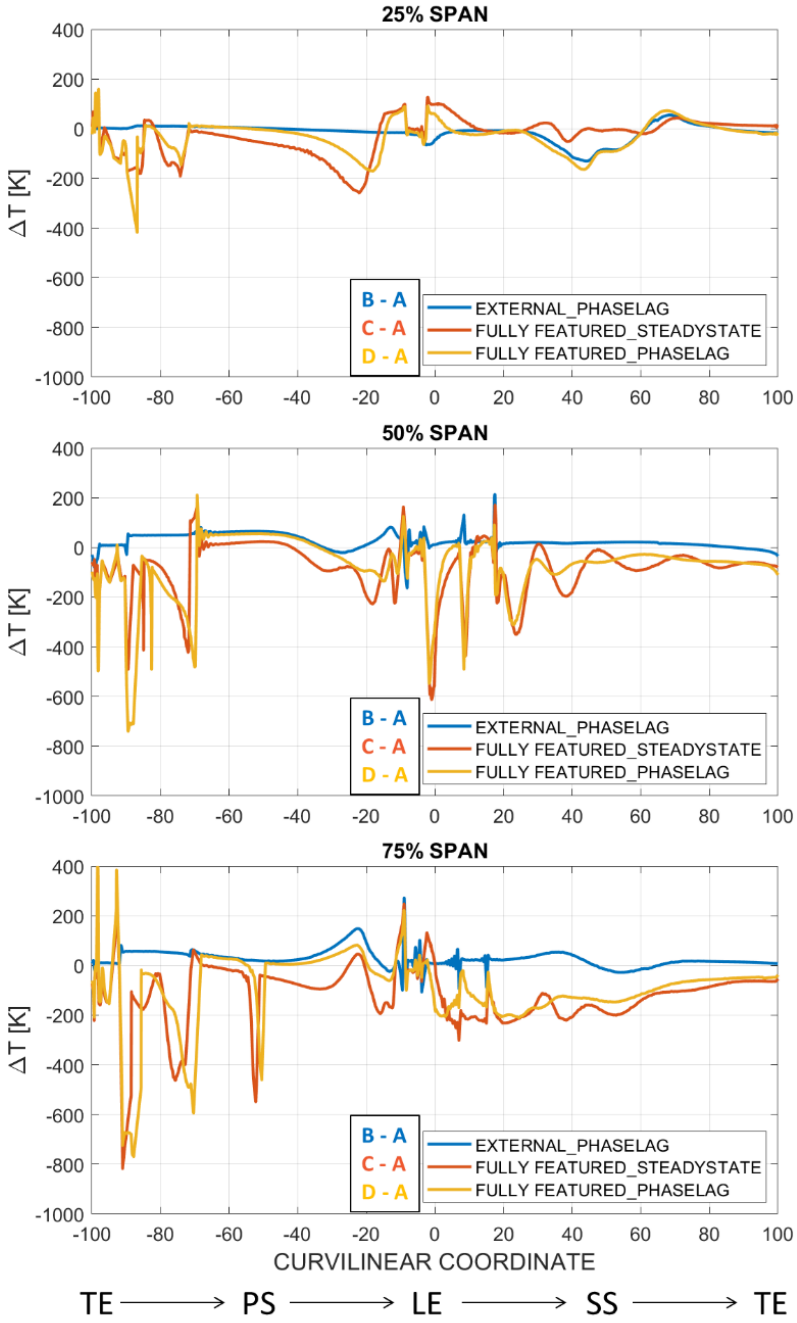

Figure 48: Comparison of the results from the different models listed in Tab. 7 in terms of HPR near wall gas static temperature delta at three sections along the span – The deltas are computed for each model with respect to model A (see Tab. 7)

The blue curve in the three plots of Fig. 48 contains information similar to what is displayed in Fig. 44. Fig. 48 confirms that with the exception of the low-span section,

the phase-lag prediction tends to be hotter than the steady-state one particularly in the PS. A marked difference can be spotted in the blue curve of Fig. 48, at 75% span for a curvilinear coordinate value of about -20, corresponding to the front PS zone, behind the LE. At the same time, it is interesting to note that the fully-featured models, represented by the orange and yellow curves in Fig. 48, mostly predict lower surface temperatures. This is particularly true for the suction side at the two top sections. This could be due to the fact that the LE rows in the fully featured cases are delivering more coolant as indicated by the graph of Fig. 46b. Interestingly, in the lowest span section at a non-dimensional coordinate of about 45 on the suction side, the fully featured phase-lag behaves remarkably similarly to the external phase-lag. The same can be said for the two steady-state models. The flow feature responsible for this negative delta is the cold surface stream visible in blue near the hub in Fig. 44b. Hence this appears to be a typical unsteady feature, captured by the phase-lag model.

Models B, C and D agree on predicting a higher temperature peak than the one predicted by model A in the LE-PS region at 75% span at a curvilinear coordinate of -25. This is within the region where the maximum near-wall gas temperatures are reached. The tendency of the phase-lag to compute hotter temperatures than its steady-state counterpart is also confirmed for the fully featured cases by comparing the orange and yellow curves in Fig. 48. Observing the results for the two sections of 50% and 75% span, it can be seen that the pressure side distributions of the fully featured models show a number of spikes. Those have to do with the presence of individual film cooling holes, as opposed to the continuous coolant emission caused by the presence of strip source terms in the external models. The fully-featured phase-lag predicts smoother temperature variations with respect to its steady-state counterpart. This finding is in line with what was observed by comparing the two external models in the previous section. It is important to understand that were a designer to trust the steady-state external simulation to determine the maximum (peak) near-wall gas temperature values on the rotor (located at a curvilinear coordinate of -25 at 75% span), this would come with a significant underestimation, that could translate into serious lifing issues for the blade.

5.3.3 Fully Featured Conjugate Analysis

In this section, steady-state CHT results are presented and discussed. The adiabatic-walls model C (see Tab. 7) is completed by adding the solid rotor domain, and a CHT run is carried out with the same BC set. Tab. 8 reports the simulations whose results are compared and discussed in this section of the thesis. The simulations listed in Tab. 8 are both steady-state. Model C is the same that was listed previously in Tab. 7.

Table 8: Multi-Fidelity Results Comparison, II

ID	MODEL TYPE	THERMAL MODELLING
C	Fully Featured	Adiabatic
F	Fully Featured	CHT

Fig. 49 shows a temperature delta plot between models F and C, at three span sections. For the adiabatic model C the values represent the near wall gas temperatures, while the surface metal temperature is considered for the conjugate model F.

Looking at the plots of Fig. 49, it can be seen that the introduction of fluid-solid heat exchange has a dramatic effect on the surface temperatures, especially on the blade's PS. The region that seems to benefit the least from this phenomenon appears to be the LE of the blade, where CHT temperatures are close to the adiabatic ones. It can be seen that the conjugate simulation predicts on average about 200K lower temperatures than the adiabatic one, with the exception of a number of positive peaks. These peaks appear where the section cuts through a cooling hole row. This can be seen in Fig. 49 where the presence of each row is indicated by a vertical dashed line, with the same color scheme used previously in Fig. 46. In the adiabatic simulation, the cooling holes produce very localized low-temperature flow streams near the wall, whereas in the conjugate solution the surface metal temperatures are smoothed out by means of heat conduction taking place within the solid. This causes the conjugate surface temperature distribution to be more homogenous, which is manifested by a positive spike in the temperature delta between the two models. This effect is particularly evident at the 50% span section.

Additional peaks of the same kind can be found downstream of each cooling hole row, for instance at a curvilinear coordinate of 40 in the 50% span section, and approximately halfway in between the TE and RPS rows in the same section (Fig. 49). This is due to the fact that some of the cooling hole rows are delivering streams of coolant that also travel radially upwards along the blade surface. Some of these streams are intersected by the section plots of Fig. 49 slightly downstream of the cooling hole rows that generated them, and this causes more temperature oscillations along the blade section.

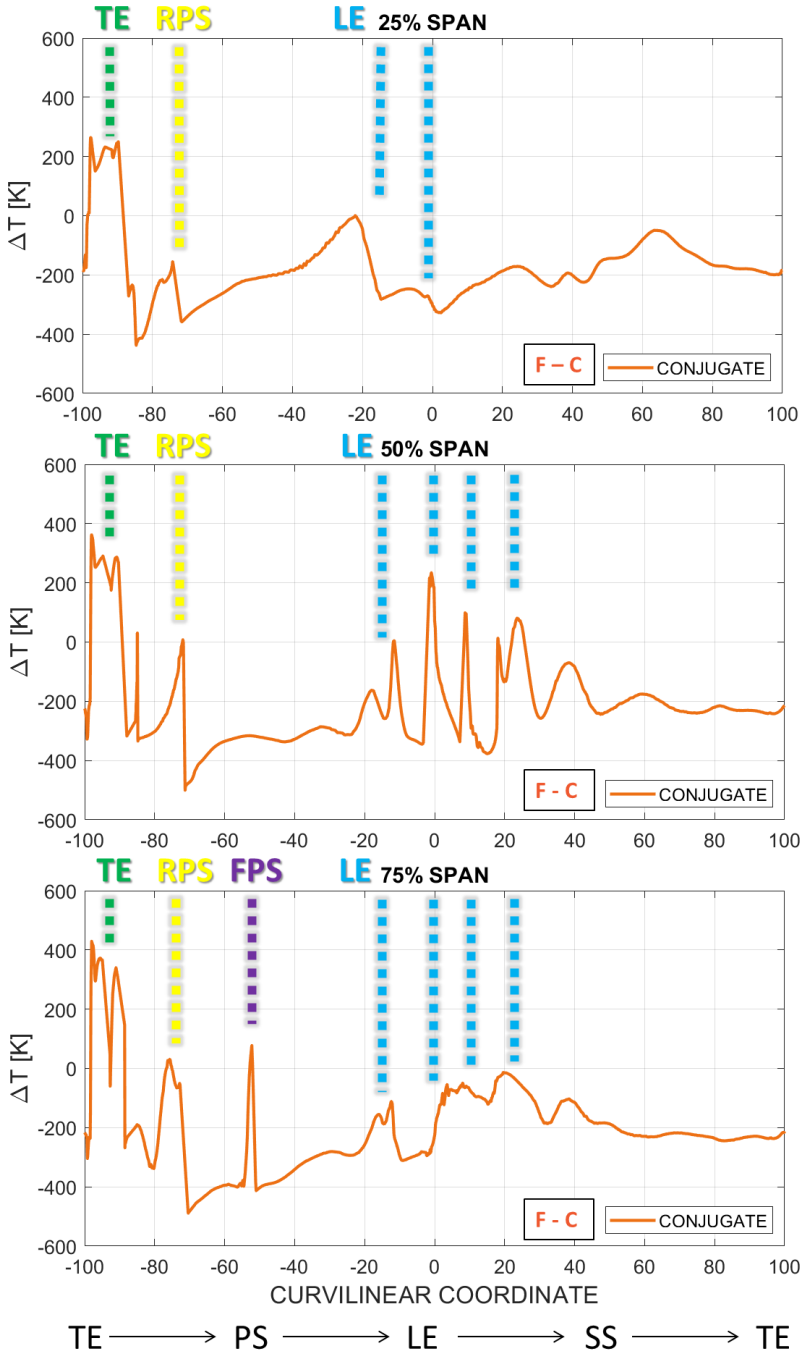

Figure 49: Comparison of the results from the two models listed in Tab. 8 in terms of HPR near wall gas static temperature delta at three sections along the span – The delta is computed between models F and C (see Tab. 8) – The dashed vertical lines signal the presence of a cooling hole row with the same color scheme used in Fig. 46

It is interesting to note that, in the TE region at all span sections, the thermal diffusion taking place within the solid due to conduction is effectively responsible for a significant (between 200K and 400K) increase in surface temperature with respect to the near-wall gas temperature prediction from the adiabatic simulation.

5.3.4 Sensitivity to Inlet Temperature Distribution

A modified HPS inlet temperature traverse (distribution) is developed from the datum one, with the objective of mitigating the rotor surface temperatures. With this new inlet BC, shown in Fig. 50b in comparison with the datum one (Fig. 50a), an additional adiabatic-walls simulation is performed, followed by the corresponding CHT simulation. The main modification introduced in the new HPS inlet BC consists in mitigating the tip bias that is clearly visible in the datum traverse. This was done by shifting of the hot spots created by the combustor towards a lower radius. The two temperature distributions are associated with the same overall total enthalpy inlet, although the modified distribution reaches a slightly lower (-60K) maximum temperature. Tab. 9 lists the (all fully featured steady-state) models that are compared in the present section.

Table 9: Multi-Fidelity Results Comparison, III

ID	THERMAL MODELLING	INLET BC
C	Adiabatic	Datum
E	Adiabatic	Modified
F	CHT	Datum
G	CHT	Modified

The results from the simulations listed in Tab. 9 are shown in Fig. 51. Similar to what was done in the previous section, each curve represents the static temperature distribution along a certain radial section of the outside surface of the rotor. The sections are once again taken at 25, 50 and 75 percent of the span. For the adiabatic-wall cases, the static temperatures are extracted at the walls inside the fluid domain, while in the CHT cases the surface metal temperatures from the solid domain are used. In the comparison of Fig. 51, all the curves represent the temperature delta, along a particular section, between each model and the model listed as C in both Tabs. 7 and 8.

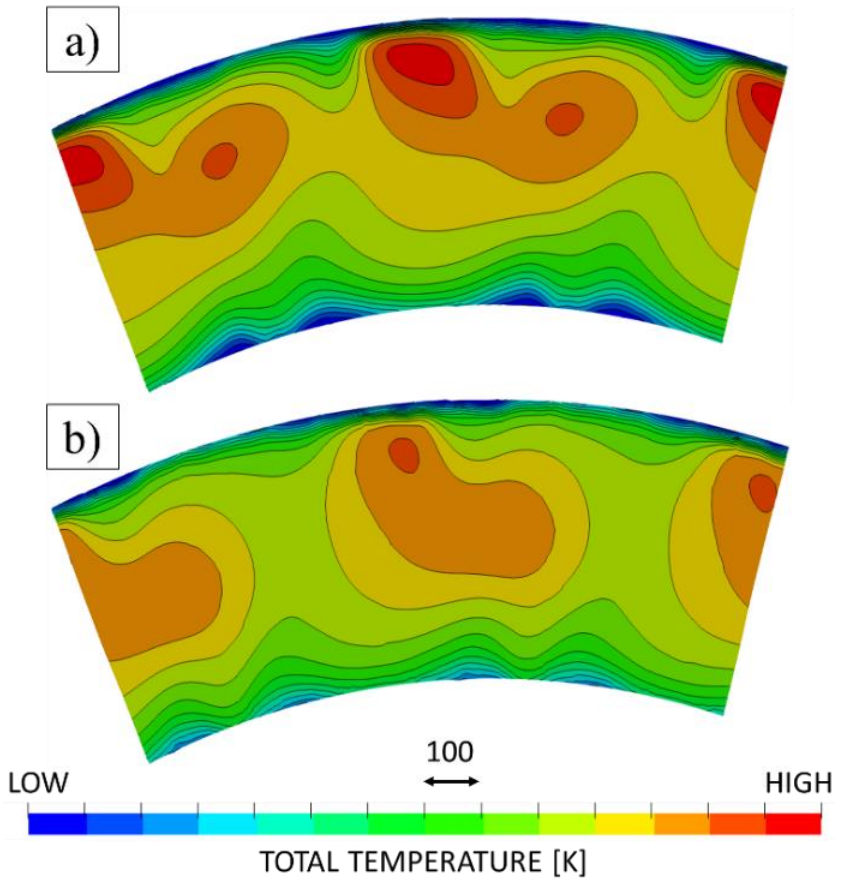

Figure 50: Comparison of the datum HPS inlet temperature distribution (a) with the modified one (b)

The modified inlet BC causes slightly higher static temperatures at 25% and 50% span, while it achieves the objective of mitigating the maximum temperatures at the highest-span section. This effect can be seen by comparing the two CHT curves (yellow and orange) of Fig. 51. The new traverse has a positive impact on the maximum temperature region, corresponding to a curvilinear coordinate between -30 and 0, where it achieves a maximum temperature reduction of 35K. The same trend can be seen when comparing the two adiabatic solutions (blue curve), with a similar, although much more intense, static temperature reductions in the critical region of 75K. This indicates that, were a designer to use a set of (albeit fully featured) adiabatic-walls simulations to estimate the benefits of switching to a different HPS traverse, this could lead to a significant overestimation.

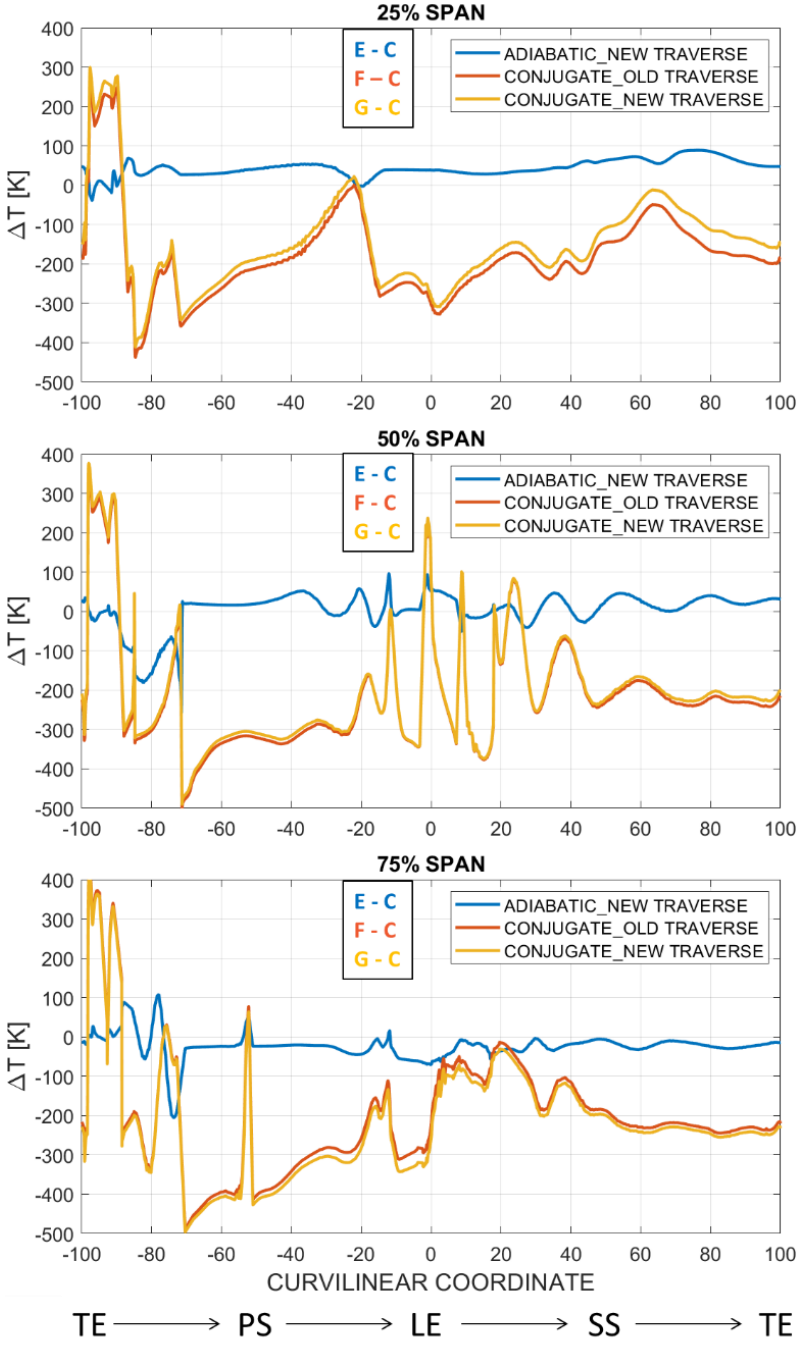

Figure 51: Comparison of the results from the different models listed in Tab. 3 in terms of HPR surface static temperature delta at three sections along the span - The deltas are computed for each model with respect to model C

5.3.5 Conjugate Heat Transfer Model Validation

In order to validate the CHT model, a simulation is conducted on the HPR row only by replicating the conditions of an experimental “thermal paint” test. This is a test where a number of rotor blades are coated with thermally-sensitive paint. The engine, which is placed in a test cell, is then operated at a working point similar to maximum take-off conditions. The paint on the HPR blades will achieve a specific final coloration based on the maximum temperature values that are locally reached during operation. After the test, the painted HPR blades are extracted from the engine and the colors on the surface of each blade are mapped to the corresponding temperatures according to the calibration coefficients. Finally, for the population of painted blades, weighted average and standard deviation of the surface temperature distributions are computed. A comparison is then made with the surface metal temperatures from the CHT simulations. For this validation run, a different set of boundary conditions was used, to match the flow conditions that were measured during the experiment. The inflow boundary condition was set at the HPR domain inlet, and the outflow at the HPR domain exit, because those are the planes where the aero-thermal quantities had been measured during the experiment.

Figs. 52-56 show the comparison by adopting the same curvilinear coordinate representation used in the previous sections. It can be seen that there is good qualitative agreement between the CHT model and the experimental results. There is a systematic CHT overestimation of the peak LE temperature, which is often due to imperfect modelling of the boundary layer transition [116, 117]. At the lowest span section (see Fig. 52) the CHT model overpredicts by a maximum of 100K the metal temperatures on the suction side (positive curvilinear coordinate values). After reviewing the data it was suggested that this could be due to uncertainty in the setting of the front hub cavity inflow boundary condition (USH in Fig. 35). It is however notable that the temperatures are mostly matched in the hottest regions of the blade, namely the LE-PS region above 50% of the span (Figs. 54-56).

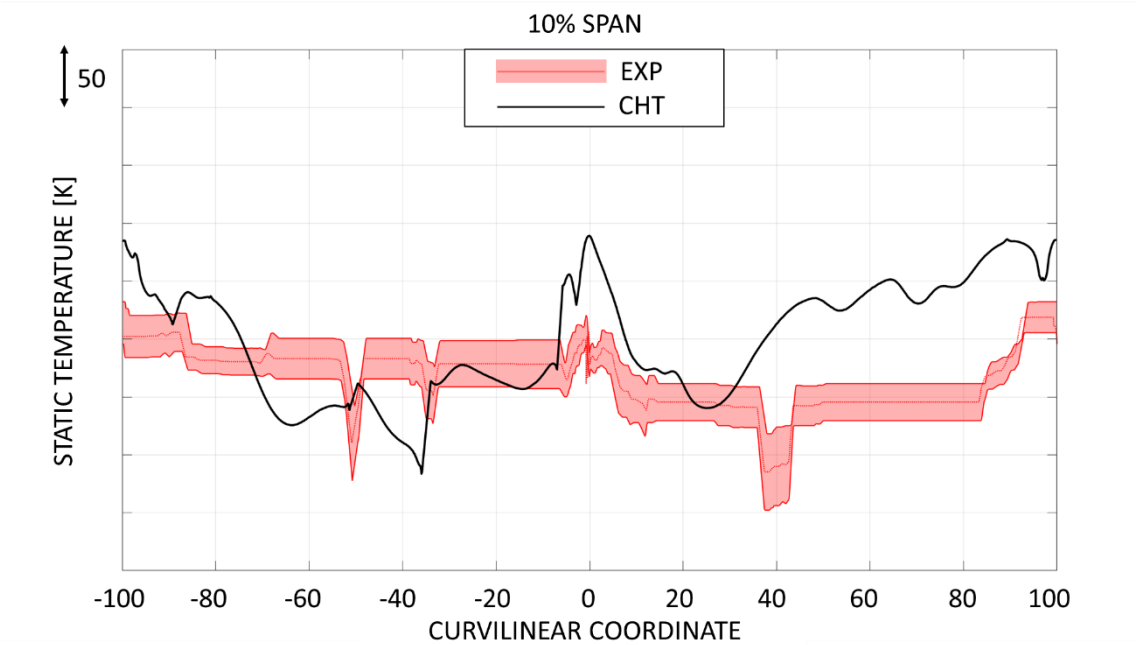

Figure 52: Comparison between CHT results (black curve) and experimental data including experimental variability (red band) at the 10% span section

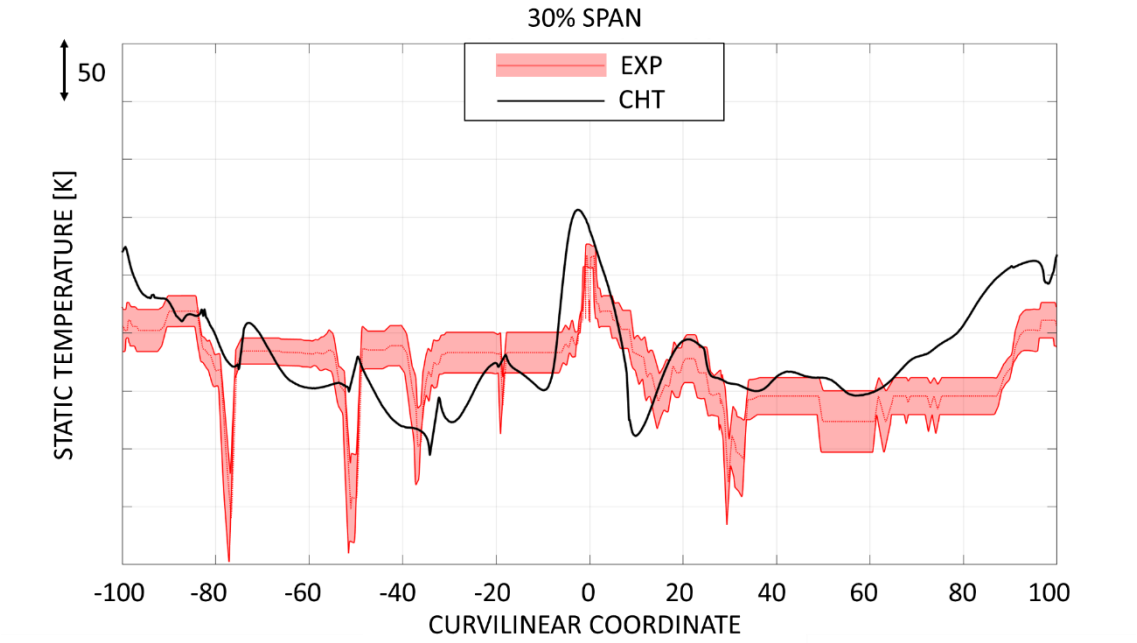

Figure 53: Comparison between CHT results (black curve) and experimental data including experimental variability (red band) at the 30% span section

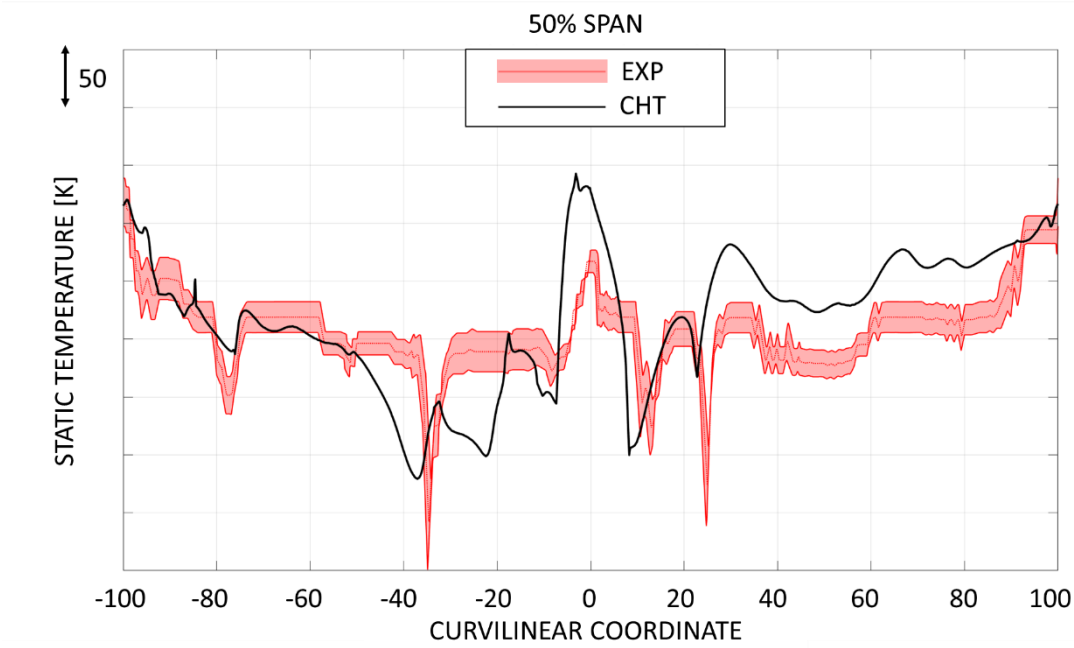

Figure 54: Comparison between CHT results (black curve) and experimental data including experimental variability (red band) at the 50% span section

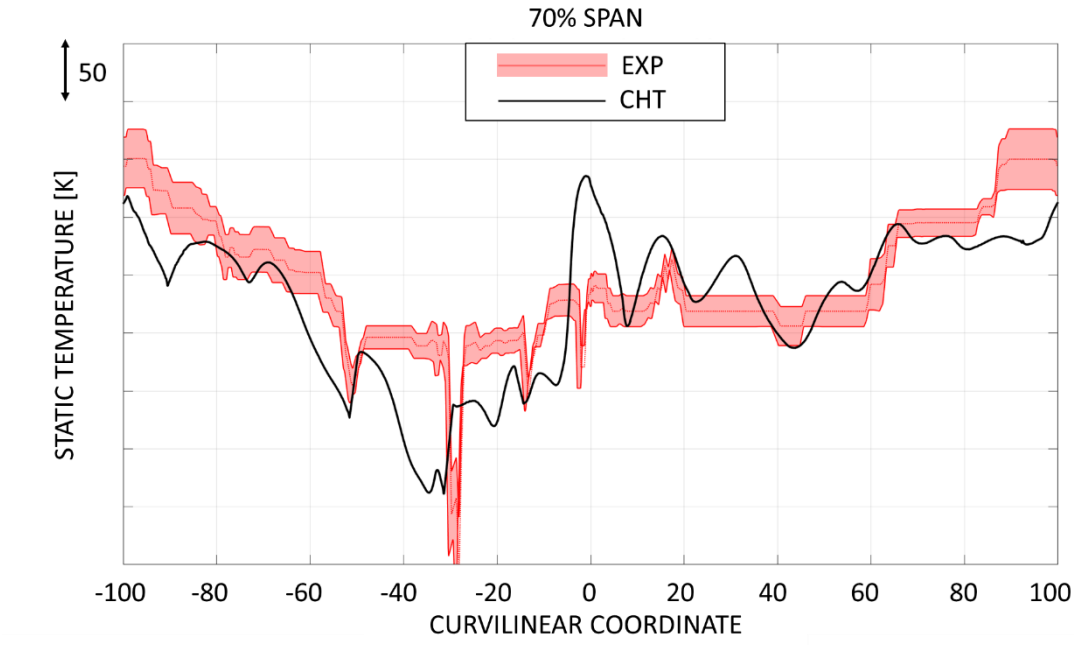

Figure 55: Comparison between CHT results (black curve) and experimental data including experimental variability (red band) at the 70% span section

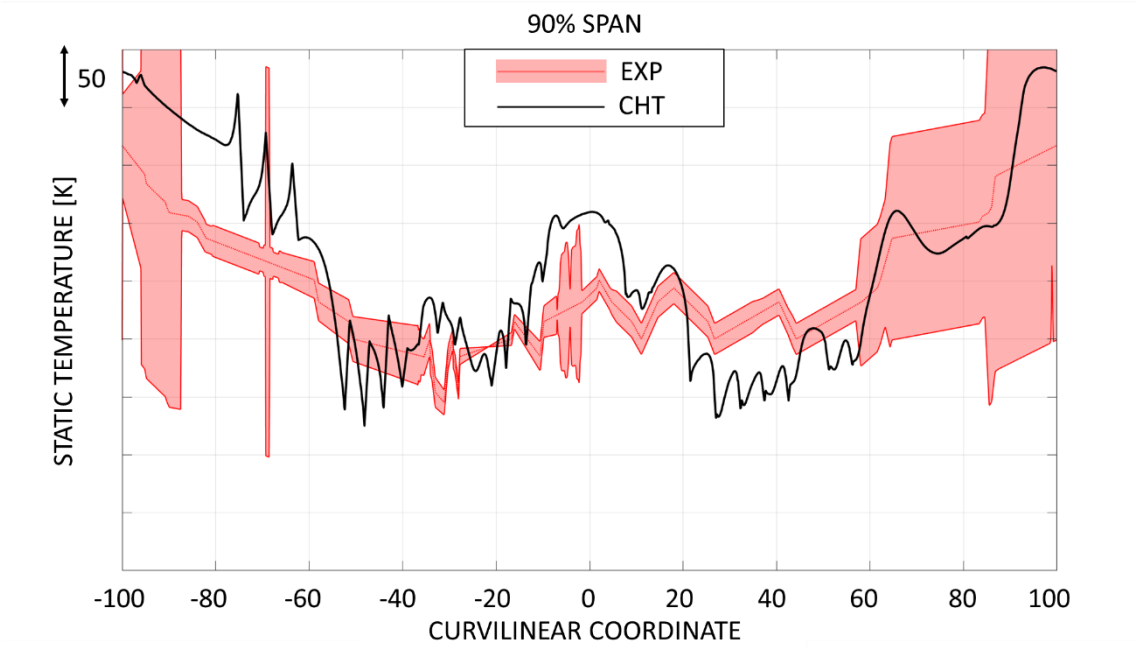

Figure 56: Comparison between CHT results (black curve) and experimental data including experimental variability (red band) at the 90% span section

5.4 Summary

CFD modelling is a tool that is today commonly used in the design and optimization processes for modern aero engine components. The fidelity of the model is an important aspect especially when dealing with complex geometries and remarkably unsteady flows. This is particularly true for the case treated in this thesis, which is the high-pressure turbine stage of a modern commercial jet engine. This work presents a comparison of the CFD results obtained with different geometric fidelity levels and different modelling techniques including steady-state and phase-lag approaches. Conjugate Heat Transfer (CHT) simulations have also been carried out to assess the importance of including the fluid-solid thermal interaction in the model.

It was found that, by switching to a phase-lag technique, the maximum near-wall gas temperature prediction is increased by around 150K with respect to the steady-state model. The film cooling effectiveness predicted by running fully featured simulations was observed to be higher than the one obtained using “strip” film cooling source models, leading on average to lower near-wall gas temperatures on the blade’s sides. Thus. when a more realistic prediction of the near-wall gas temperatures on a high-pressure turbine rotor is sought for, it is highly advisable to run phase-lag or unsteady simulations.

Fully featured modelling is indeed more computationally expensive than external flow simulation but can provide some important insight into the behavior of the cooling flow inside the internal channels. In the industry, 1D and 2D models are often used to compute the amount of coolant provided by each cooling hole row. These models rely on a simplified apportioning of the losses within the system, i.e. local pressure loss is introduced in the internal flow where the channel presents a bend and so on. This modelling technique fails to properly capture the mixing losses that take place downstream of the local pressure-loss elements and may thus provide unrealistic estimations of the amount of coolant delivered by each row. This is especially true when moving away from the nominal operating conditions, at which point further error is introduced by the scaling process, necessary to adjust the mass flow rates of the cooling strips.

A new combustor temperature distribution aimed at mitigating the maximum temperatures on the rotor was tested both with adiabatic and conjugate-heat-transfer simulations. It was observed that the amount of maximum near-wall temperature reduction predicted by the adiabatic simulations could be significantly larger (+114%) than the surface metal temperature reduction predicted by the conjugate results, due to the effect of heat conduction in the metal.

Chapter 6

Conclusions and Future Work

6.1 Conclusions

The work presented in this thesis is part of an undergoing effort, aimed at gaining an accurate understanding of the complex flow phenomena that take place inside the high-pressure turbine of a modern jet engine. The means used by the author to pursue this effort is constituted by high-fidelity CFD (numerical) simulation. The investigation is centered on:

- Quantifying the variation of the design's performance that is caused by geometric uncertainty mostly due to in-service deterioration.
- Quantifying the impact of different modelling fidelities on the accuracy of the numerical results.

The first part of the analysis focuses on the impact of in-service damage on the aerodynamic performance of the high-pressure turbine blades. This is done by conducting flow simulations on a set of 120 high-resolution optical scans of real turbine blades, that were selected from multiple engines at the end of their service life. The blades are observed to display various degrees of damage, including plastic deformation, abrasion, and erosion. This geometric deterioration is quantified and parametrized with the use of an automatic uncertainty quantification tool. Computational grids are generated with a high-fidelity approach directly on the deteriorated surfaces. Through steady-state full-3D RANS analysis of the HP stage, these geometries are found to suffer from significant performance deficits with respect to the design intent counterpart, having lost in some cases more than four percent of their nominal isentropic HP stage efficiency. With a series of additional CFD simulations, an efficiency loss breakdown study is conducted, by isolating particular damage modes in order to account for their individual impact on efficiency loss. It is found that eighty to ninety percent of the performance deficit is due to erosion damage in the blades' shrouds, and the remaining part is due to deformations taking place

below the shroud. A highly linear correlation is observed between a combination variable expressing shroud damage and stage efficiency loss, with a coefficient of determination (R^2) exceeding 0.9. Through this correlation study, it is discovered that the most important parameter affecting efficiency is the gap between neighboring shroud platforms at the mid-chord position. This parameter is seldom mentioned in current literature among the relevant drivers for performance loss for a shrouded turbine blade design.

The second part of the analysis is represented by an investigation on the implications of in-service damage on the heat transfer patterns of the high-pressure turbine blades. Once again, a number of optical scans of real blades are selected, and the same meshing and simulation procedures are put in place. To evaluate the heat transfer coefficient on the blades, a quadratic regression method is used, which requires two additional CFD simulations to be run for each case. Being that the aerodynamic analysis revealed the shroud region to be the most influential for performance loss, the thermal investigation focuses on the same region. It is found that the blades with the most amount of erosion in the shroud-gap region are the ones that display the highest heat transfer, thus most prone to suffering further damage. This suggests that these blades have been operating through a "vicious circle" of damage, where the latter is responsible for higher deterioration rates, which in turn cause further damage and so forth. A correlation study between the heat transfer coefficient and shroud erosion on the blades is conducted, revealing significant linearity between the two. The most relevant erosion parameter for heat transfer increase on the shroud is found to be the inter-platform shroud gap in the rear half of the platforms. An aerodynamic correlation analysis conducted on this new set of blades confirms the relevance of the inter-platform shroud gap in determining stage efficiency loss.

The last part of the work focuses on assessing the impact of modelling fidelity on the CFD results' accuracy for the same high-pressure turbine case. In this part of the work, a number of different simulation techniques are used, including steady-state RANS and phase-lag RANS to capture the periodic unsteadiness. On the geometric fidelity side, different levels of accuracy in the representation of the rotor geometries are adopted. The simplified geometry, which is of the kind that is most often used in industrial CFD analysis, is represented by a tight external-only rotor blade. In this case, all the internal channels that characterize this design's film cooling system are omitted from the geometric representation, and simplified strip-source models are used on the blade surface to surrogate the presence of rows of film-cooling holes. The second, more realistic geometry that is used, includes all these internal channels and cooling holes. Finally, a number of conjugate heat transfer simulations are run on the realistic geometries, to study the impact of including the fluid-solid heat exchange in the model. The phase-lag technique is found to predict a maximum near-wall gas temperature that is around 150K higher than the one predicted by the steady-state model. Thus. when a

more realistic prediction of the near-wall gas temperatures on a high-pressure turbine rotor is sought for, it is highly advisable to run phase-lag or unsteady simulations. Fully featured (realistic geometry) simulations are found to predict higher film cooling effectiveness levels than the ones obtained using “strip” film cooling source models. In addition, a new inlet temperature distribution coming from the combustor is prepared and tested, with the idea of moving the combustor hot-spots towards lower radii and introducing a slight clocking. The conjugate results show that a notable reduction in surface metal temperature is achieved by adopting the new distribution.

6.2 Future Work

Further work is currently in progress to leverage the knowledge gained during this research activity, in terms of design sensitivity to various input variabilities, with the aim of conducting a multi-disciplinary robust optimization. In consideration of the amount of mechanical stress that characterizes the normal operation of a high-pressure turbine blade, the structural aspect will also be taken into account, together with the aerodynamic and thermal ones, for the purposes of the optimization. Being that the present Ph. D. work has shown the relevance of component performance estimation in the presence of manufacturing variation and real in-service deterioration, the optimization will be aimed at de-sensitizing the geometry to this kind of geometric variability, de-risking the component with respect to its entry into service and operability. As a consequence of the findings of Chapter 5 of this work, related to the importance of using fully featured components, methods will be developed to enable the measurement, digitalization, and parametrization of geometric variation inside the internal channels of the rotor blade. A technique will then be developed to enable the automatic morphing of the nominal fully-featured CAD geometry according to the parametrized geometric variation, and the resulting blade (with a complete definition of its geometric uncertainty) will be the subject of the optimization process. Another aspect to be taken into account is the uncertainty in the so-called cold-to-hot transition (see Section 3.2.1). This has to do with the axial displacement and elastic deformations (due to thermal, centrifugal and gas loads) that the blades experience when the engine is gradually brought to its operating point. The experience gained in the present work concerning the relevance of estimating the effects of periodic unsteadiness on near-wall gas temperatures will be used in the future optimization study, which will include multi-passage, multi-row phase-lag simulations.

References

[1] M. Carta, T. Ghisu and S. Shahpar, "High-Fidelity CFD Analysis of In-Serviced Shrouded High-Pressure Turbine Rotor Blades - TURBO-22-1122," *ASME Journal of Turbomachinery*, vol. 144, no. 12, p. 121001 (12 pages), 2022.

[2] M. Carta, T. Ghisu and S. Shahpar, "Heat Transfer Analysis of Damaged Shrouded HIgh Pressure Turbine Rotor Blades," in *Accepted for the ETC15 - 15th european turbomachinery conference on "turbomachinery fluid dynamics and thermodynamics"*, Budapest, Hungary, 2023.

[3] M. Carta, T. Ghisu and S. Shahpar, "Multi-Fidelity Heat Transfer Analysis of Shrouded High Pressure Turbine Rotor Blades, GT2023-103789," in *Accepted for the ASME Turbo Expo 2023 conference*, Boston, Massachussets, USA, 2023.

[4] M. Carta, T. Ghisu and R. Putzu, "A Comparison of Plunging- and Pitching-induced Deep Dynamic Stall on a SD7003 Airfoil Using URANS and LES Simulations," *Aerospace Science and Technology*, vol. 121, no. February, 2022.

[5] T. Ghisu, F. Cambuli, P. Puddu, I. Virdis , M. Carta and F. Licheri, "A critical examination of the hysteresis in wells turbines using computational fluid dynamics and lumped parameter models," *Journal of Offshore Mechanics and Arctic Engineering*, vol. 142, no. 5, 2020.

[6] T. Ghisu, Cambuli F., P. Puddu, I. Virdis, M. Carta and F. Licheri, "A lumped parameter model to explain the cause of the hysteresis in OWC-Wells turbine systems for wave energy conversion," *Applied Ocean Research*, vol. 94, 2020.

[7] T. Ghisu, F. Cambuli, P. Puddu, I. Virdis and M. Carta, "Discussion: "unsteady RANS simulations of wells turbine under transient flow conditions" (Hu and Li, ASME J. Offshore Mechanics and Arctic Engineering, 140(1)," *Journal of Offshore Mechanics and Arctic Engineering*, vol. 141, no. 4, 2019.

[8] M. Carta, T. Ghisu and S. Shahpar, "High-Fidelity CFD Analysis of Shrouded High-Pressure Turbine Rotor Blades," in *ASME Turbo Expo 2022*, Rotterdam, 2022.

[9] D. S. Lee, D. W. Fahey, A. Skowron, M. R. Allen, U. Burkhardt, Q. Chen, S. J. Doherty, S. Freeman, P. M. Forster, J. Fuglestvedt, A. Gettelman, R. R. De Leon, L. L. Lim, M. T. Lund, R. J. Millar, B. Owen, J. E. Penner, G. Pitari, M. J. Prather, R. Sausen and L. J. Wilcox, "The Contribution of Global Aviation to Antrophogenic Climate Forcing for 2000 to 2018," *Atmospheric Environment*,

vol. 244:117834, 2021.

[10] S. Addepalli, G. Pagalday, K. Salonitis and R. Roy, "Socio-economic and demographic factors that contribute to the growth of the civil aviation industry," in *Proceedings of the 6th International Conference in Through-life Engineering Services*, University of Bremen, 7th and 8th November 2017.

[11] S. Freeman , D. S. Lee, L. L. Lim, A. Skowron and R. R. De Leon, "Trading off aircraft fuel burn and NOX emissions for optimal climate policy," *Environmental Science & Technology*, vol. 52, no. 5, pp. 2498-2505, 2018.

[12] S. Shparberg and B. Lange, "Airbus Global Market Forecast," 8 July 2022. [Online]. Available: https://www.airbus.com/en/products-services/commercial-aircraft/market.

[13] R.-R. plc, "Ultrafan: The ultimate turbofan," [Online]. Available: https://www.rolls-royce.com/innovation/ultrafan.aspx. [Accessed 14 09 2020].

[14] The Jet Engine, Fifth Edition, Derby, UK: Rolls-Royce, 1986.

[15] P. C. Ruffles, "Evolution of the Aero Gas Turbine," in *Trenchard Lecture*, 1991.

[16] R. S. Bunker, "Integration of New Aero-Thermal and Combustion Technologies with Long-Term Design Philosophies for Gas Turbine Engines," in *US – Ukrainian Workshop on Innovative Combustion and Aerothermal Technologies in Energy and Power Systems*, Kiev, Ukraine, 2001.

[17] M. J. Donachie and J. Stephen, Superalloys, a Technical Guide, ASM International, 2002 2nd Edition, ISBN 0-87170-749-7.

[18] L. S. Langston, The Adaptable Gas Turbine, American Scientist 101:264-267, 2013.

[19] C. R. Simcoe, Metallurgy Lane: Pioneers in Metal Research - Part VI., Advanced Materials and Processes, March 2016.

[20] F. J. Cunha, 4.4 Heat Transfer Analysis, NETL - The Gas Turbine Handbook, 2006.

[21] S. Ito, R. J. Goldstein and E. R. G. Eckert, "Film Cooling of a Gas Turbine Blade," *J. Eng. Power*, vol. 100, no. 3, pp. 476-481 (6 pages), Jul 1978.

[22] K. Takeishi, S. Aoki, T. Sato and K. Tsukagoshi, "Film Cooling on a Gas Turbine Rotor Blade," *J. Turbomach. Oct 1992, 114(4): 828-834 (7 pages)*, vol.

114, no. 4, pp. 828-834 (7 pages), Oct 1992.

[23] E. R. G. Eckert, "Analysis of Film Cooling and Full-Coverage Film Cooling of Gas Turbine Blades," *J. Eng. Gas Turbines Power,* vol. 106, no. 1, pp. 206-213 (8 pages), Jan 1984.

[24] L. Xu, S. Bo, Y. Hongde and W. Lei, "Evolution of Rolls-royce Air-cooled Turbine Blades and Feature Analysis," *Procedia Engineering,* vol. 99, pp. 1482-1491, 2015.

[25] J. D. Denton and W. N. Dawes, "Computational fluid dynamics for turbomachinery design.," *Proc Instn Mech Engrs,* vol. 213, no. Part C, pp. 107-124, 1999.

[26] J. Horlock and J. D. Denton, "A review of some early design practice using computational fluid dynamics and a current perspective," *Journal of Turbomachinery,* vol. 127, no. 1, 2005.

[27] R. W. Walters and L. Huyse, "Uncertainty Analysis for Fluid Mechanics with Applications, CR 0211449," NASA, 2002.

[28] A. Ben-Tal and A. Nemirovski, "Robust Optimization - Methodology and Applications," *Mathematical Programming,* 2002.

[29] D. Scott and J. Thompson, "Probability density estimation in higher dimensions," in *Computer Science and Statistics: Proceedings of the Fifteenth Symposium on the Interface,* 1983.

[30] "A problem of dimensionality: A simple example," in *IEEE Transactions on Pattern Analysis and Machine Intelligence. PAMI-1(3):306–307,* 1979..

[31] P. Indyk and R. Motwani, "Approximate nearest neighbors: Towards removing the curse of dimensionality.," in *Proceedings of the Thirtieth Annual ACM Symposium on Theory of Computing,* New York, NY, USA, 1998.

[32] S. Berchtold, C. Bohm and H. P. Kriegal, "The pyramid-technique: Towards breaking the curse of dimensionality," in *SIGMOD Record, 27(2):142–153,* jun 1998.

[33] S. Shahpar, "Building Digital Twins to Simulate Manufacturing Variation," in *ASME Turbo Expo 2020: Turbomachinery Technical Conference and Exposition,* September 2020, GT2020-15263.

[34] I. S. Diakunchak, "Performance Deterioration in Industrial Gas Turbines," *J. Eng. Gas Turbines Power,* vol. 114, no. 2, pp. 161-168 (8 pages), Apr 1992.

[35] A. Jarrett, V. V. Erukulla and A. K. Koul, "Untwist Creep Analysis of Gas Turbine First Stage Blade," in *ASME Turbo Expo: Turbomachinery Technical Conference and Exposition,* Phoenix, Arizona, USA, 2019, GT2019-90979.

[36] M. Naeem, "Implications of Turbine Erosion for an Aero-Engine's High-Pressure-Turbine Blade's Low-Cycle-Fatigue Life-Consumption," *J. Eng. Gas Turbines Power,* vol. 131, no. 5, p. 052501 (8 pages), Sep 2009.

[37] T. J. Carter, "Common failures in gas turbine blades," *Engineering Failure Analysis,* vol. 12, no. 2, p. 237–247, 2005.

[38] S. Garner and Z. Ibrahim, "Gas Turbine Common Issues, Failure Investigations, Root Cause Analyses, and Preventative Actions," in *ASME Power Conference*, 2016.

[39] "Gom Metrology," [Online]. Available: https://www.gom.com/.

[40] W. L. Oberkampf and T. G. Trucano, "Verification and Validation in Computational Fluid Dynamics," *Progress in Aerospace Sciences,* vol. 38, no. 3, pp. 209-272, 2002.

[41] A. Ben-Tal, L. El Ghaoui and A. Nemirovski, Robust Optimization, Princeton: Princeton University Press, 2009.

[42] D. Bertsimas, D. B. Brown and C. Caramanis, "Theory and Applications of Robust Optimization," *Society of Industrial and Applied Mathematics,* vol. 53, no. 3, p. 464–501, 2011.

[43] J. S. Arora, Introduction to Optimum Design, Iowa City, Iowa: Elsevier, 2004.

[44] G.-J. Park, T.-H. Lee, K. H. Lee and K.-H. Hwang, "Robust Design: An Overview," *AIAA Journal,* vol. 44, no. 1, pp. 181-191, 2006.

[45] H.-G. Beyer and B. Sendhoff, "Robust optimization – A Comprehensive Survey," *Computer Methods in Applied Mechanics and Engineering,* vol. 196, no. 33-34, pp. 3190-3218, 2007.

[46] C. Hirsch, D. Wunsch, J. Szumbarski, L. L. Wollk and J. Pons-Prats, Uncertainty Management for Robust Industrial Design in Aeronautics, Springer, 2019.

[47] S. Shahpar, "Towards Robust CFD Based Design Optimisation of Virtual Engine," NATO Unclassified Paper, 2007.

[48] A. Kumar, A. J. Keane, P. B. Nair and S. Shahpar, "Robust Design of Compressor Blades Against Manufacturing Variations," in *Proceedings of IDETC/CIE*, Philadelphia, Pennsylvania, 2006.

[49] A. Kumar, A. J. Keane, P. B. Nair and S. Shahpar, "Robust design using Bayesian Monte Carlo," *International Journal for Numerical Methods in Engineering*, vol. 73, p. 1497–1517, 2008.

[50] A. Kumar, A. J. Keane, S. Shahpar and P. B. Nair, "Efficient Robust Design for Manufacturing Process Capability," in *Proceedings of the 6th ASMO UK conference on Engineering Design Optimization*, 2015.

[51] A. Kumar, P. B. Nair, A. J. Keane and S. Shahpar, "Robust Design of Compressor Fan Blades Against Erosion," *Journal of Mechanical Design*, vol. 128, no. 4, pp. 864-873, 2006.

[52] P. Seshadri, S. Shahpar and G. T. Parks, "Robust Compressor Blades for Desensitizing Operational Tip Clearance Variations," in *Proceedings of ASME Turbo Expo 2014: Turbine Technical Conference and Exposition*, Düsseldorf, Germany, 2014.

[53] J. Kamenik, I. Voutchkov, D. J. J. Toal, A. J. Keane, L. Hogner, M. Meyer and R. Bates, "Robust Turbine Blade Optimization in the Face of Real Geometric Variations," *Journal of Propulsion and Power*, vol. 34, no. 6, pp. 1479-1493, 2018.

[54] R. T. Marler and J. S. Arora, "The Weighted Sum Method for Multi-Objective Optimization: New insights," *Structural and Multidisciplinary Optimization*, vol. 41, no. 6, p. 853–862, 2010.

[55] X. Wang, "CFD Simulation of Complex Flows in Turbomachinery and Robust Optimization of Blade Design," Vrije Universiteit Brussel, Bruxelles, 2010.

[56] C. Zhiying and Z. Ping, "Robust Optimization Design for Turbine Blade-Tip Radial Running Clearance using Hierarchically Response Surface Method," in *IOP Conference Series: Materials Science and Engineering*, 2017.

[57] P. N. Koch, R.-J. Yang and L. Gu, "Design for Six Sigma through Robust Optimization," *Structural and Multidisciplinary Optimization*, vol. 26, pp. 235-

248, 2004.

[58] S. B. Jeong, J. Lim and G. J. Park, "Robust Optimization Using the Probabilistic Robustness Index and the Enhanced Single-Loop Approach," *AIAA Journal,* vol. 52, no. 7, pp. 1568-1573, 2014.

[59] D. Roos, J. Einzinger and V. Bayer, "Robust Design Optimization Applied to Structural, Thermal and Fluid Analysis Including Manufacturing Tolerances," in *Proceedings of the sixth Weimar Optimization and Stochastic Days*, Weimar, Germany, 2009.

[60] H. Kato, H. Mashiko, Y. Tokuyama, K. Funazaki and J. Takida, "Robust Aerodynamic Shape Optimization of Supersonic Turbine Using Non-Intrusive Polynomial Chaos Expansion," in *9th World Congress on Structural and Multidisciplinary Optimization*, Shizuoka, Japan, June 13 - 17, 2011.

[61] Y. M. Korolev, V. V. Toropov and S. Shahpar, "Design Optimization Under Uncertainty Using the Multipoint Approximation Method," in *58th AIAA/ASCE/AHS/ASC Structures, Structural Dynamics, and Materials Conference*, Grapevine, Texas, 9 - 13 January 2017.

[62] G. Antinori, I. Arsenyev and A. Fischersworring-Bunk, "Robust Design Optimization of a Low Pressure Turbine Rotor Discs Secondary Air System," in *Proceedings of ASME Turbo Expo 2017: Turbomachinery Technical Conference and Exposition*, Charlotte, NC, June 26-30, 2017.

[63] I. Martin, L. Hartwig and D. Bestle, "A Multi-Objective Optimization Framework for Robust Axial Compressor Airfoil Design," *Structural and Multidisciplinary Optimization,* vol. 59, p. 1935–1947, 2019.

[64] P. Seshadri, G. T. Parks and S. Shahpar, "Density-Matching for Turbomachinery Optimization Under Uncertainty," *arXiv,* 2015.

[65] T. Ghisu, G. T. Parks, J. P. Jarrett and P. J. Clarkson, "Robust Design Optimization of Gas Turbine Compression Systems," *Journal of Propulsion and Power,* vol. 27, no. 2, pp. 282-295, 2011.

[66] E. A. Dow and Q. Wang, "The Implications of Tolerance Optimization on Compressor Blade Design," *Journal of Turbomachinery*, vol. 137, no. 10, 2015.

[67] X. Wang, S. Kang, C. Hirsch and C. Lacor, "Uncertainty-Based Robust Aerodynamic Optimization of Rotor Blades," *International Journal for*

Numerical Methods in Engineering, vol. 94, no. 2, pp. 111-127, 2013.

[68] D. Roos, T. Most and J. Will, "Advanced Surrogate Models Within the Robustness Evaluation," in *Weimar Optimization and Stochastic Days 4.0*, Weimar, Germany, 2007.

[69] I. N. Egorov, G. V. Kretinin and I. A. Leshchenko, "Robust Design Optimization Strategy of IOSO Technology," *Fifth World Congress on Computational Mechanics*, 2002.

[70] J. Will, "Combination of Optimization and Robustness Evaluation from Practical Point of View," DYNARDO GMBH, Weimar, Germany, 2015.

[71] K. Deb, A. Pratap , S. Agarwal and T. Meyarivan, "A Fast and Elitist Multiobjective Genetic Algorithm: NSGA-II," *IEEE Transaction of Evolutionary Computation*, vol. 6, no. 2, p. 182–197, 2002.

[72] D. M. Jaeggi, G. T. Parks, T. Kipouros and P. J. Clarkson, "The Development of a Multi-Objective Tabu Search Algorithm for Continous Optimisation Problems," *European Journal of Operational Research*, vol. 185, no. 3, p. 1192–1212, 2008.

[73] S. Shahpar, "SOFT: A New Design And Optimisation Tool for Turbomachinery," in *Evolutionary Methods for Design, Optimisation and Control, CIMNE*, Barcelona, 2002.

[74] S. Heinrich and E. Sindambiwe, "Monte Carlo Complexity of Parametric Integration," *Journal of Complexity*, vol. 15, no. 3, pp. 317-341, 1999.

[75] M. B. Giles, "Multilevel Monte Carlo Path Simulation," *Operations Research*, vol. 56, no. 3, pp. 607-617, 2008.

[76] N. Collier, A. Haji-Ali, F. Nobile, E. von Schwerin and R. Tempone, "A Continuation Multilevel Monte Carlo algorithm," *BIT Numer. Math.*, vol. 55, no. 2, pp. 399-432, 2015.

[77] P. Seshadri, G. T. Parks, J. Jarrett and S. Shahpar, "Towards robust design of axial compressors with uncertainty quantification," in *AIAA/ASME/ASCE/AHS/ASC Structures, Structural Dynamics and Materials Conference*, 2013.

[78] B. Glezer, "Thermal-mechanical design factors affecting turbine blade tip clearance," in *VKI LS 2004-02, Turbine blade tip design and tip clearance treatment, ISBN 2-930389-51-6*, Rhode-St-Genese, Belgium, von Karman

Institute for Fluid Dynamics, 2004, pp. 1-23.

[79] N. W. Harvey, "Aerothermal Implications of shroudless and shrouded blades," in *VKI LS 2004-02, Turbine blade tip design and tip clearance treatment, ISBN 2-930389-51-6*, Rhode-St-Genese, Belgium, von Karman Institute for Fluid Dynamics, 2004.

[80] S. Colón, M. Ricklick, D. Nagy and A. Lafleur, "Geometric Effects of Thermal Barrier Coating Damage on Turbine Blade Temperatures," in *ASME Turbo Expo: Turbomachinery Technical Conference and Exposition*, Phoenix, Arizona, USA, 2019, GT2019-90886.

[81] E. A. Ogiriki, Y. G. Li, T. Nikolaidis, E. I. ThankGod and G. Sule, "Effect of Fouling, Thermal Barrier Coating Degradation and Film Cooling Holes Blockage on Gas Turbine Engine Creep Life," *Procedia CIRP*, no. 38, pp. 228-233, 2015.

[82] J. Jean-Roch and N. A. M. Nor, "A Methodology and Case Study of Outboard Traverse Flame Detection on Aeroderivative Gas Turbines," in *ASME Turbo Expo: Turbomachinery Technical Conference and Exposition*, Phoenix, Arizona, USA, 2019, GT2019-90158.

[83] J. Kamenik, S. Shahpar, A. J. Keane, L. Hogner, M. Meyer and D. J. J. Toal, "Modelling and Impact of High-pressure Turbine Blade Trailing Edge Film Cooling Hole Variations," in *AIAA Scitech 2020 Forum*, Orlando, Florida, 6-10 January 2020.

[84] C. V. Sidwell, "On the impact of variability and assembly on turbine blade cooling flow and oxidation life," PhD Thesis, Massachusetts Institute of Technology, 2004.

[85] D. G. Ainley and G. C. R. Mathieson, "A Method of Performance Estimation for Axial-Flow Turbines," British Aeronautical Research Council R&M 2974, 1951.

[86] O. E. Baljé and R. L. Binsley, "Axial Turbine Performance Evaluation. Part A - Loss-Geometry Relationships," *Journal of Engineering and Power,* vol. 90, no. 4, pp. 341-348, 1968.

[87] M. K. Mukhtarov and V. I. Krichakin, "A Procedure for Estimating Losses in the Flow Path of Axial Turbines in Calculating their Characteristics," *Teploenergetika,* vol. 7, pp. 26-31, 1969.

[88] A. V. Zaita, G. Buley and G. Karlsons, "Performance Deterioration Modeling in Aircraft Gas Turbine Engines," in *Intenational Gas Turbine & Aeroengine*

Congress & Exhibition, Orlando, Florida, June 2 - June 5 1997.

[89] J. D. Denton, "Loss Mechanisms in Turbomachines," *Journal of Turbomachinery*, vol. 115, no. 4, pp. 621-656, 1993.

[90] T. W., Thermische Turbomaschinen, Berlin: Springer-Verlag, 1966.

[91] J. Gier, B. Stubert, B. Brouillet and L. de Vito, "Interaction of Shrouded Leakage Flow and Main Flow in a Three-Stage LP Turbine," *Journal of Turbomachinery*, vol. 125, no. 4, pp. 649-658, 2005.

[92] M. Pau, F. Cambuli and N. Mandas, "Shroud Leakage Modeling of the Flow in a Two-Stage Axial Test Turbine," in *ASME Turbo Expo: Power for Land, Sea and Air*, Berlin, Germany, June 9-13, 2008, GT2008-51093, pp. 1333-1343.

[93] S. H. Moustapha, S. C. Kacker and B. Tremblay, "An Improved Incidence Losses Prediction Method for Turbine Airfoils," *Journal of Turbomachinery*, vol. 112, no. 2, pp. 267-276, 1990.

[94] M. W. Benner, S. A. Sjolander and S. H. Moustapha, "Influence of Leading-Edge Geometry on Profile Losses in Turbines at Off-Design Incidence: Experimental Results and an Improved Correlation," *Journal of Turbomachinery*, vol. 119, no. 2, pp. 193-200, 1997.

[95] S. Yoon, T. Vandeputte, H. Mistry, J. Ong and A. Stein, "Loss Audit of a Turbine Stage," *Journal of Turbomachinery*, vol. 138, no. 5, 2006.

[96] J. D. Denton and L. Xu, "The Trailing Edge Loss of Transonic Turbine Blades," *Journal of Turbomachinery*, vol. 112, no. 2, pp. 277-285, 1990.

[97] S. Shahpar and L. Lapworth, "PADRAM: Parametric Design and Rapid Meshing System for Turbomachinery Optimisation, GT2003-38698, pp. 579-590," in *ASME Turbo Expo and International Joint Power Generation Conference*, Atlanta, Georgia, USA, 2003.

[98] A. A. J. Demargne, R. O. Evans, P. J. Tiller and W. N. Dawes, "Practical and Reliable Mesh Generation for Complex, Real World Geometries," in *AIAA 52nd Aerospace Sciences Meeting*, National Harbor, Maryland, USA, 2014, AIAA 2014-0119.

[99] L. Lapworth, "Hydra CFD: a Framework for Collaborative CFD Development," in *International Conference on Scientific and Engineering Computation (IC-SEC)*, Singapore, 2004.

[100] G. Occhioni, S. Shahpar and H. Li, "Multi-Fidelity Modelling of a Fully-Featured HP Turbine Stage," in *ASME Turbo Expo: Turbomachinery Technical Conference and Exposition*, Charlotte, North Carolina, USA, 2017, GT2017-64478.

[101] P. Seshadri and G. T. Parks, "Effective-Quadratures (EQ): Polynomials for Computational Engineering Studies," *The Journal of Open Source Software*, vol. 2, no. 11, 2017.

[102] T. Ghisu and S. Shahpar, "Affordable Uncertainty Quantification for Industrial Problems: Application to Aero-Engine Fans," *Journal of Turbomachinery*, vol. 140, no. 6, p. 061005, 2018.

[103] R. E. Dundas, "Investigation of Failure in Gas Turbines: Part 2 — Engineering and Metallographic Aspects of Failure Investigation," in *ASME 1993 International Gas Turbine and Aeroengine Congress and Exposition*, Cincinnati, Ohio, USA, May 24–27, 1993, 93-GT-84.

[104] A. M. Kolagar, N. Tabrizi, M. Cheraghzadeh and M. S. Shahriari, "Failure Analysis of Gas Turbine First Stage Blade Made of Nickel-Based Superalloy," *Case Studies in Engineering Failure Analysis*, vol. 8, pp. 71-78, 2017.

[105] X. Guo, W. Zheng, C. Xiao, L. Li, S. Antonov, Y. Zheng and Q. C. Feng, "Evaluation of microstructural degradation in a failed gas turbine blade due to overheating," *Engineering Failure Analysis*, vol. 103, pp. 308-318, 2019.

[106] J. Han and L. M. Wright, 4.2.2.2 Enhanced Internal Cooling of Turbine Blades and Vanes, NETL - The Gas Turbine Handbook, 2006.

[107] R. Maffulli and L. He, "Wall Temperature Effects on Heat Transfer Coefficient - GT2013-94291," in *Asme Turbo Expo*, Fairfield, USA, 2013.

[108] R. Maffulli and L. He, "Dependence of External Heat Transfer Coefficient And Aerodynamics on Wall Temperature For 3D Turbine Blade Passage - GT2014-26763," in *Asme Turbo Expo*, Dusseldorf, Germany, 2014.

[109] A. Fitt, C. Forth, B. Robertson and T. Jones, "Temperature Ratio Effects in Compressible Turbulent Boundary Layers," *International Journal of Heat and Mass Transfer*, vol. 29, no. 1, pp. 159-164, 1986.

[110] W. Kays and M. Crawford, Convective Heat and Mass Transfer, Second Edition ed., Tata Mc Graw Hill Publishing Co. Ltd, 1983.

[111] B. Lakshminarayana, Fluid Dynamics and Heat Transfer of Turbomachinery, Wiley-Interscience Publication, Wiley & Sons, 1995.

[112] B. Petukhov, "Heat Transfer and Friction in Turbulent Pipe Flow with Variable Physical Properties," *Advances in Heat Transfer*, vol. 6, pp. 503-564, 1970.

[113] E. T. McGarry, "Digital Measuring Borescope System 98-GT-534, V005T15A038; 4 pages," in *ASME 1998 International Gas Turbine and Aeroengine Congress and Exhibition*, Stockholm, Sweden, June 2–5, 1998.

[114] D. L. Rigby and J. Lepicovsky, "Conjugate Heat Transfer Analysis of Internally Cooled Configurations," in *ASME Turbo Expo 2001*, New Orleans, Louisiana, USA, June 4–7, 2001 .

[115] W. D. York and J. H. Leylek, "Three-Dimentional Conjugate Heat Transfer Simulation of an Internally-Cooled Gas Turbine Vane," in *ASME Turbo Expo*, Atlanta, Georgia, USA, June 16-19, 2003.

[116] B. Facchini, A. Magi and A. S. Greco, "Conjugate Heat Transfer of a Radially Cooled Gas Turbine Vane," in *ASME Turbo Expo*, Vienna, Austria, June 14–17, 2004.

[117] K. Ho, C. Urwiller, S. M. Konan, J. Liu and B. Aguilar, "Conjugate Heat Transfer Analysis for Gas Turbine Cooled Stator," in *ASME Turbo Expo*, Copenhagen, Denmark, June 11–15, 2012.

[118] K. Tsukamoto, H. Yasuhiro, S. Kazuyuki and H. Shinichi, "Conjugate Heat Transfer Analysis in an Actual Gas Turbine Rotor Blade in Comparison with Pyrometer Data," in *ASME Turbo Expo*, Düsseldorf, Germany, June 16–20, 2014.

[119] K. Ho, C. Urwiller, S. M. Konan, J. Liu and B. Aguilar, "Conjugate Heat Transfer Analysis for Gas Turbine Cooled Blade," in *ASME Turbo Expo*, Düsseldorf, Germany, June 16–20, 2014.

[120] T. Takahashi, W. Kazunori and S. Takayuki, "Conjugate Heat Transfer Analysis of a Rotor Blade With Rib-Roughened Internal Cooling Passages, GT2005-68227," in *ASME Turbo Expo*, Reno, Nevada, USA, June 6–9, 2005.

[121] J. L. Erdos and E. Alzner, "Computation of unsteady transonic flows through rotating and stationary cascades," NASA CR-2900, 1977.

[122] L. He, "An Euler solution for unsteady flows around oscillating blades," *Journal of Turbomachinery*, vol. 112, no. 4, pp. 714-722, 1990.

[123] L. He, "Fourier methods for Turbomachinery Applications," *Progress in Aerospace Sciences,* vol. 46, no. 8, pp. 329-341, 2010.

[124] S. Salvadori, P. Adami and F. Martelli, "On the Implementation of a Phase Lag Approach for Multi-Row Simulations," in *Proceedings of the 10th International Symposium on Experimental, Computational Aerothermodynamics of Internal Flows*, Brussels, Belgium, 4-7 July 2011.

[125] R. Schnell, "Investigation of the Tonal Acoustic Field of a Transonic Fan Stage by Time-Domain CFD Calculations with Arbitrary Blade Counts, ASME paper GT2004-54216," in *Turbo Expo: Power for Land, Sea, and Air*, Vienna, Austria, June 14-17, 2004.

[126] G. A. Gerolymos, G. Michon and J. Neubauer, "Analysis and Application of Chronochronic Periodicity in Turbomachinery Rotor/Stator Interaction Computations," *Journal of Propulsion and Power,* vol. 18, no. 6, pp. 1139-1152, 2002.